JOURNAL OF PETROLOGY

Journal of Petrology, 2015, Vol. 56, No. 4, 645–679
doi: 10.1093/petrology/egv010
Original Article

OXFORD

Pre-Eruptive Conditions of the Hideaway Park Topaz Rhyolite: Insights into Metal Source and Evolution of Magma Parental to the Henderson Porphyry Molybdenum Deposit, Colorado

Celestine N. Mercer[1]*, Albert H. Hofstra[1], Todor I. Todorov[2], Julie Roberge[3], Alain Burgisser[4], David T. Adams[5] and Michael Cosca[1]

[1]Denver Inclusion Analysis Laboratory, US Geological Survey, Denver, CO 80225, USA, [2]Center for Food & Drug and Safety & Applied Nutrition, US Food & Drug Administration, College Park, MD 20740, USA, [3]ESIA-Ticoman, Instituto Politecnico Nacional, D.F. 07340, Mexico, [4]ISTerre, Université de Savoie, 73376 Le Bourget du Lac-cedex, France and [5]Department of Earth & Planetary Sciences, Macquarie University, Sydney, NSW 2109, Australia

*Corresponding author. E-mail: cmercer@usgs.gov

Received April 28, 2014; Accepted February 25, 2015

ABSTRACT

The Hideaway Park tuff is the only preserved extrusive volcanic unit related to the Red Mountain intrusive complex, which produced the world-class Henderson porphyry Mo deposit. Located within the Colorado Mineral Belt, USA, Henderson is the second largest Climax-type Mo deposit in the world, and is therefore an excellent location to investigate magmatic processes leading to Climax-type Mo mineralization. We combine an extensive dataset of major element, volatile, and trace element abundances in quartz-hosted melt inclusions and pumice matrix glass with major element geochemistry from phenocrysts to reconstruct the pre-eruptive conditions and the source and evolution of metals within the magma. Melt inclusions are slightly peraluminous topaz rhyolitic in composition and are volatile-charged ($\leq$6 wt % H_2O, $\leq$600 ppm CO_2, ~0·3–1·0 wt % F, ~2300–3500 ppm Cl) and metal-rich (~7–24 ppm Mo, ~4–14 ppm W, ~21–52 ppm Pb, ~28–2700 ppm Zn, <0·1–29 ppm Cu, ~0·3–1·8 ppm Bi, ~40–760 ppb Ag, ~690–1400 ppm Mn). Melt inclusion and pumice matrix glass chemistry reveal that the Hideaway Park magma evolved by large degrees of fractional crystallization ($\leq$60–70%) during quartz crystallization and melt inclusion entrapment at pressures of $\leq$300 MPa ($\leq$8 km depth), with little to no crystallization upon shallow ascent and eruption. Filter pressing, crystal settling, magma recharge and mixing of less evolved rhyolite melt, and volatile exsolution were important processes during magma evolution; the low estimated viscosities (~10^5–10^{10} Pa s) of these H_2O- and F-rich melts probably enhanced these processes. A noteworthy discrepancy between the metal contents in the pumice matrix glass and in the melt inclusions suggests that after quartz crystallization ceased upon shallow magma ascent and eruption, the Hideaway Park magma exsolved an aqueous fluid into which Mo, Bi, Ag, Zn, Mn, Cs, and Y strongly partitioned. Given that the Henderson deposit contains anomalous abundances of not only Mo, but also W, Pb, Zn, Cu, Bi, Ag, and Mn, we suggest that these metals were sourced from similar fluids exsolved from unerupted portions of the same magmatic system. Trace element ratios imply that Mo was sourced deep, from either the lower crust or metasomatized mantle. The origin of sulfur remains unresolved; however, given the extremely low S solubility of rhyolite melts in the shallow crust we favor the possibility that another source of S might supplement or account for that present in the ore deposit, probably the comagmatic, mantle-derived lamprophyres that occur in minor quantities with the voluminous topaz rhyolites in the area. To account for the 437 Mt of MoS_2 (~$1·0 \times 10^6$ t Mo) present in the Henderson ore deposit, a volume of ~45 km^3 of Hideaway Park rhyolite magma would have been necessary to supply the Mo (a cylindrical pluton measuring

3·1 km × 6·0 km) along with sparging of ~6·8 × 10^5 t of S from ~0·05 km^3 of lamprophyre magma. Based on a weighted mean $^{40}Ar/^{39}Ar$ age of 27·58 ± 0·24 Ma, similar melt geochemistry, and characteristically F-rich biotite phenocrysts, we conclude that the Hideaway Park tuff was cogenetic with the intrusions at Red Mountain that formed the Henderson deposit.

Key words: rhyolite; crystallization; P–T conditions; melt inclusions; metals; degassing; Henderson porphyry molybdenum deposit; LA-ICP-MS

INTRODUCTION

The world's molybdenum supply is mined primarily from porphyry-type ore deposits. Porphyry Mo deposits are important sources and reserves of Mo, second only to porphyry Cu (±Mo, Au) deposits, where Mo is recovered as a byproduct. Among Mo-bearing porphyry ore deposits, Climax-type deposits contain large amounts of Mo comparable with those of giant porphyry Cu–Mo deposits such as Bingham, Chiquicamata, Butte, and El Teniente. The Climax and Henderson deposits are among the few porphyry systems that have >1 Mt of contained Mo, and are the only deposits of this size with grades averaging >0·2% Mo (e.g. Carten *et al.*, 1993; Ludington & Plumlee, 2009). Climax-type deposits are distinguished from other Mo-bearing porphyry deposits by containing distinctively high abundances of Mo and F, and bearing virtually no Cu. The deposits consist of overlapping ore shells composed of quartz-molybdenite stockwork veins that lie above and surround the apices of highly evolved calc-alkaline granite and subvolcanic rhyolite porphyry intrusions (e.g. Carten *et al.*, 1993; Wallace, 1995; Ludington & Plumlee, 2009). These intrusions are characteristically enriched in F (commonly >1 wt %), Rb (>500 ppm), and Nb (>50 ppm) and are restricted to regions of the North American Cordillera that underwent crustal extension and bimodal magmatism during the middle to late Cenozoic (e.g. Ludington & Plumlee, 2009, and references therein).

The source and evolutionary path of metals and sulfur in Climax-type deposits has been a topic of much debate. The restricted distribution of Climax-type Mo deposits in continental rift settings with episodic mafic alkaline and silicic magmatism has led many to suggest a mantle origin for the molybdenum and sulfur (e.g. Westra & Keith, 1981; Carten *et al.*, 1993; Keith & Christiansen, 1993; Audétat, 2010; Audétat *et al.*, 2011). On the other hand, some researchers advocate an upper crustal source, given the extremely thick crust and localized, long-lived nature of some Mo-bearing provinces such as the Colorado Mineral Belt (Bookstrom, 1981; e.g. Sinclair, 2007; Zhu *et al.*, 2009), whereas others call on a combination of sources involving contributions from the lower crust and ancient metasomatized subcontinental lithospheric mantle (e.g. Klemm *et al.*, 2008; Pettke *et al.*, 2010). Although evidence for mingling of mafic and felsic magmas is sparse in Climax-type intrusive complexes (e.g. Bookstrom *et al.*, 1988; Carten *et al.*, 1993), most districts contain mafic and felsic igneous rocks that are approximately coeval (e.g. Pine Grove, Utah, Keith *et al.*, 1986; Questa, New Mexico, Johnson & Lipman, 1988; Johnson *et al.*, 1989). Recent work by Audétat (2010) demonstrates that molybdenum and sulfur at the Cave Peak Mo deposit in Texas were probably concentrated through fractional crystallization of mafic, alkaline magmas generated in a continental rift setting. In addition, sulfur isotope work by Stein & Hannah (1985) on three porphyry Mo deposits from the western USA led them to conclude that sulfur was derived from a source deeper than the upper continental crust.

Understanding the origin of Climax-type mineralizing fluids is ultimately linked to unraveling the petrological evolution of the parental magma that fed the ore-forming stock and the partitioning of key elements in exsolved fluids within it. In this study we present analyses of quartz-hosted silicate melt inclusions, pumice matrix glass, and phenocrysts from the Hideaway Park tuff, a high-silica topaz rhyolite, which is thought to be the only preserved cogenetic extrusive expression of the intrusive complex that formed the world-class Henderson porphyry Mo deposit (Adams *et al.*, 2009). These compositional data are used to determine pre-eruptive magmatic conditions (pressure, temperature, oxygen fugacity), volatile contents (H_2O, CO_2, F, Cl, S), and metal concentrations to elucidate magmatic processes and metal evolution within an ore-forming, Climax-type intrusive complex.

GEOLOGICAL FRAMEWORK

The Urad and Henderson ore bodies comprise a stacked pair of porphyry Mo deposits associated with Oligocene high-silica rhyolite intrusions of the Red Mountain Complex near Empire, Colorado (Fig. 1; Wallace *et al.*, 1978; Shannon *et al.*, 1982, 2004; Carten *et al.*, 1988*a*; Wallace, 1995; Seedorff & Einaudi, 2004*a*). These deposits represent a premier example of Climax-type mineralization related to bimodal magmatism in a rift-related setting (Bookstrom, 1981; Geraghty *et al.*, 1988; Carten *et al.*, 1993). The relatively shallow, smaller, and older Urad orebody (Fig. 1) is hosted by the 1·4 Ga Silver Plume granite (Peterman *et al.*, 1968) and stocks of Oligocene, pre-Red Mountain rhyolite porphyry (Wallace, 1974; Wallace *et al.*, 1978). Mineralization of the Urad orebody is attributed to intrusion of the 28·5 ± 2·2 Ma Square Quartz porphyry (Wallace *et al.*, 1978; zircon fission-track age from Geissman *et al.*, 1992). The Urad

deposit is cut by the Red Mountain porphyry intrusion, a large cylindrical intrusion, which probably vented to the surface (Taylor *et al.*, 1968; Wallace *et al.*, 1978; Stein & Crock, 1990). The Red Mountain porphyry widens with depth into the larger, Urad porphyry, which hosts the bulk of the Henderson deposit (Fig. 1). The much larger Henderson orebody is located ~1000 m below the summit of Red Mountain. It consists of three closely spaced overlapping ore zones with variable amounts of Mo mineralization, each of which is associated with a rhyolitic intrusive center, from oldest to youngest (based on cross-cutting relationships): the Henderson [>28·71 ± 0·08 Ma ($^{40}Ar/^{39}Ar$); ~27·5 ± 2 Ma (zircon fission-track)], Seriate [<29·8 ± 0·1 Ma, >28·71 ± 0·08 Ma ($^{40}Ar/^{39}Ar$)], and Vasquez [~28·71 ± 0·08 Ma ($^{40}Ar/^{39}Ar$); ~25 ± 2 Ma (zircon fission-track)] centers (Fig. 1; Bookstrom *et al.*, 1988; Geissman *et al.*, 1992). Together, these centers are composed of a dozen or more stocks that intruded the Urad porphyry, and evidently did not vent to the surface (Carten *et al.*, 1988*a*, 1988*c*). Re–Os dating of molybdenite powder from the Henderson mill suggests a molybdenum mineralization age of 27·656 ± 0·022 Ma (Markey *et al.*, 2007). Paleodepth estimates for the apices of these mineralized intrusions based on geological reconstructions are ~1·6 km for the Urad deposit and 2·8–3·1 km for the Henderson deposit (Carten *et al.*, 1988*a*; Geraghty *et al.*, 1988).

Extrusive volcanic products sourced from the Red Mountain intrusive complex have not been clearly identified. However, several features suggest that volcanic eruptions took place after mineralization of the Urad orebody but before mineralization of the Henderson orebody, from a vent (or vents) higher in the system than is now preserved. The amount of extrusive material that could have vented is unknown. There are several generations of radially and concentrically distributed rhyolite and pebble dikes emanating from the magmatic center as well as a series of rubble dikes and breccia pipes along the central Red Mountain porphyry conduit. The shattering of wall-rocks and the presence of pumice fragments and glass shards in the Peak breccia exposed at the summit of Red Mountain indicates that rapid gas release and venting probably took place (Taylor *et al.*, 1968; Wallace *et al.*, 1978).

The intrusions of the Red Mountain complex can be linked by similar bulk composition, age, and common Precambrian structural controls to several occurrences of rhyolitic tuffs that crop out throughout the Fraser Basin to the NE (Fig. 1; Taylor & King, 1967; Taylor *et al.*, 1968). The Hideaway Park tuff is the largest of these bodies of rhyolitic tuff. It is a light gray, rhyolitic ash-flow tuff that crops out along the Fraser River 16 km NE of the Red Mountain intrusive complex near the town of Winter Park, Colorado (Fig. 1; Taylor *et al.*, 1968). The estimated thickness of the tuff is ~15 m to >150 m (Shroba *et al.*, 2010). The rock has been locally quarried for ornamental and foundation stone and is used extensively in the mountain cabins of the Winter Park resort (Taylor *et al.*, 1968). The first K–Ar analyses of sanidine phenocrysts from the upper tuff yielded an age of ~29 ± 3 Ma (Taylor *et al.*, 1968). More recent analyses of sanidine from the same unit yielded an $^{40}Ar/^{39}Ar$ plateau age of 27·49 ± 0·24 Ma (2σ) (Knox, 2005; revised to the Fish Canyon sanidine standard age used in this study). Comparison of ages and bulk-rock compositions with other Oligocene igneous centers (e.g. Never Summer igneous complex 40 km north of Winter Park; Knox, 2005; Shroba *et al.*, 2010) in the region suggests that the most likely source for the tuff is either the Red Mountain complex or a concealed vent near Winter Park (Shroba *et al.*, 2010).

METHODS

Sample preparation

Pumice and poorly to moderately welded tuff were sampled from the upper and lower parts of a section of the Hideaway Park ash-flow tuff (Fig. 1). Thin and thick polished sections were prepared and examined with a standard petrographic microscope in preparation for scanning electron microscope (SEM) and microprobe analysis of phenocrysts. Special attention was paid to the occurrence of melt and mineral inclusions.

A portion of the poorly welded upper tuff (including pumice clasts) was crushed using a small jaw crusher for bulk-rock analysis. Pumice clasts from another portion of the upper tuff were carefully scraped out and quartz phenocrysts were removed using tweezers to prepare the glassy portion for bulk analysis. The pumice matrix glass was lightly crushed using a porcelain mortar and pestle. The moderately welded lower tuff does not contain extractible pumice clasts and bulk-rock analysis reveals that it is slightly silicified, so we do not report bulk-rock or pumice matrix glass analysis from this sample. Bulk-rock and pumice matrix glass samples were ground to a fine powder with an agate mortar and pestle for analysis by wavelength-dispersive X-ray fluorescence (WD-XRF) and inductively coupled plasma mass spectrometry (ICP-MS) in the Analytical Chemistry Laboratory at the USGS in Denver. Quartz grains were picked from the smaller size fractions (~0·5–2 mm) and then cleaned with a 12% solution of HF for 10 min. Quartz grains hosting suitable melt inclusions (fully enclosed, uncracked melt inclusions) were selected for analyses. Half of these crystals were prepared for analysis by laser ablation (LA)-ICP-MS, whereas the other half were used in homogenization experiments to prepare them for analysis by Fourier transform infrared (FTIR) spectroscopy, electron probe microanalysis (EPMA), and LA-ICP-MS.

Preparation of crystalline inclusions

Single quartz phenocrysts with suitable crystalline melt inclusions were mounted in acetone-soluble crystal bond on microscope slides and were doubly ground and polished to make wafers with inclusions that

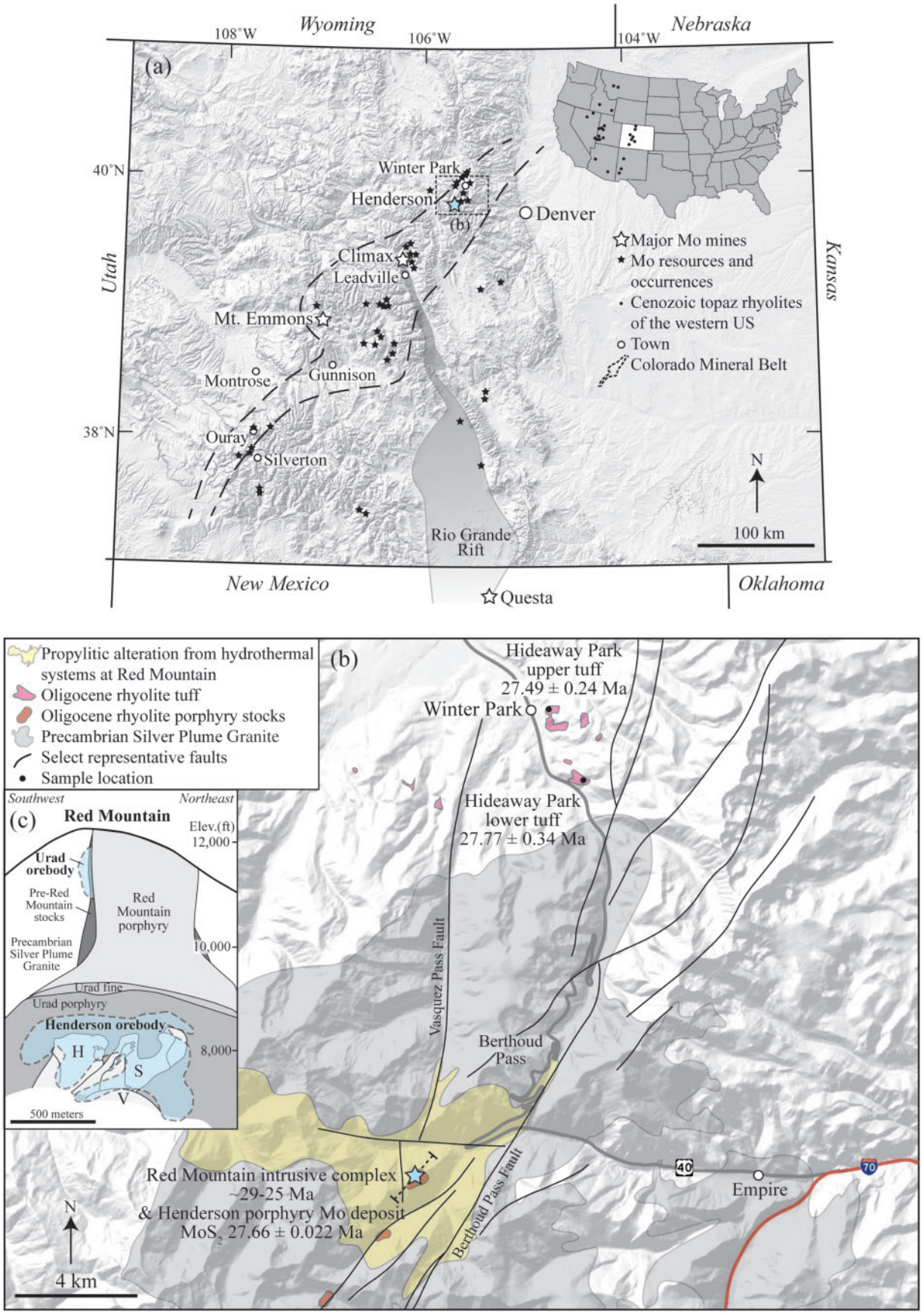

Fig. 1. (a) Schematic map of Colorado showing the location of the Henderson porphyry Mo deposit, Red Mountain intrusive complex, and Winter Park, the sampling area for this study. For reference, we also show: the Colorado Mineral Belt (modified from

were within ~10–80 μm of the top polished surface. The wafers were then washed multiple times with acetone and mounted on glass slides using epoxy so that the melt inclusions could be analyzed for trace elements by LA-ICP-MS.

Preparation of homogenized inclusions

Batch homogenization experiments were conducted by Dr T. Sisson using a ZHM (zirconium–hafnium–molybdenum) cold-seal pressure vessel housed at the US Geological Survey in Menlo Park, CA. Melt inclusion-bearing quartz crystals were loaded into Pt capsules (4 mm × 13 mm), which were twisted and crimped closed. Capsules were open to the pressure medium to prevent quartz grains from crushing against one another. A pressure medium of pure Ar was used. Experimental oxygen fugacity (fO_2) was not controlled; however, the Mo-bearing pressure vessel tends to buffer the fO_2 at reducing conditions of <Mo–MoO_2 (T. Sisson, personal communication), or ~FMQ – 4·5 (where FMQ is fayalite–magnetite–quartz).

Experiments were run at 120–150 MPa to prevent inclusion decrepitation and were maintained to within ±3 MPa using a Heise gauge. The capsule was pressurized to the target pressure at room temperature after which power was applied to heat the capsule to the target temperature over ~30 min. Experiments were initially performed at a wide variety of temperatures (810–1010°C) and durations (10 min to 5·75 h) to determine adequate homogenization conditions. The details we present here are representative of experiments for which problems of 'over-' and 'under-homogenization' were minimized (i.e. there was not excessive dissolution of the quartz host into the melt inclusion and post-entrapment quartz along inclusion rims was adequately incorporated into the melt inclusion). Experiments were held at target conditions for 15 min to 5·5 h. Temperatures ranged from 860 to 1010°C and were maintained to within ±7°C using a Pt–Pt_{90}–Rh_{10} thermocouple positioned in a well in the pressure vessel. Thermocouples were calibrated by comparison with a reference thermocouple following the methods of Sisson & Grove (1993).

The pressure vessel was positioned vertically in a Deltech DT31VT resistance furnace, held at pressure and temperature for the duration of the experiment, and then quenched rapidly (≥200°C s^{-1}) by inverting the vessel so that the sample capsule fell against the water-cooled pressure seal (Sisson & Grove, 1993).

After quenching, the capsules were carefully opened and quartz grains hosting glassy, fully enclosed inclusions were selected. Single quartz phenocrysts were prepared similarly to phenocrysts with crystalline inclusions, except that the glassy inclusions were doubly intersected and polished to make wafers with the glass inclusions exposed on both sides (typically ~20–250 μm thick). Wafers were washed multiple times with acetone in preparation for FTIR analysis. After analysis by FTIR, the wafers were mounted on glass slides using epoxy for analysis by EPMA and LA-ICP-MS.

Diffusion of hydrogen (H_2, H_2O, and/or H^+) from melt inclusions commonly occurs during laboratory reheating (e.g. Severs *et al.*, 2007; Zajacz *et al.*, 2009), but in many cases it is difficult to quantify because it overprints diffusion from natural post-entrapment processes (e.g. cooling of the tuff) and natural variability within samples. Nevertheless, it is important to consider when evaluating volatile contents in melt inclusions. In this study, samples were homogenized over a range of pressure–temperature–time conditions and the duration of experiments shows the strongest control on diffusion. For example, melt inclusions from the lower tuff that were heated for 5·5 h at 860°C average ~75% less dissolved H_2O than those run for 15 min at 1010°C. We observed no correlation between degree of diffusion and melt inclusion size or distance from the edge of the host quartz; however, the latter is difficult to quantify because many of the host phenocrysts fractured during sample preparation.

Analytical procedures

$^{40}Ar/^{39}Ar$ geochronology

The $^{40}Ar/^{39}Ar$ analyses were performed at the USGS in Denver, CO, where sanidine grains were separated from rock samples using standard heavy liquid, magnetic, and hand-picking techniques. The separated sanidine grains and standards were arranged in aluminum disks that were stacked and sealed in an evacuated quartz tube and irradiated for 2 MW h in the central thimble position of the USGS TRIGA reactor.

The irradiated sanidine samples and standards were loaded into numbered positions of a stainless steel planchette, placed into a laser sample chamber with an externally pumped ZnSe window, and evacuated to ultra-high vacuum conditions in a fully automated stainless steel extraction line designed and built at the USGS in Denver. Using a 25 W CO_2 laser equipped with a beam homogenizing lens, one aliquot of several small

Tweto & Sims, 1963); major and minor Mo mines, resources, and occurrences (Lehmann, 1987; Klemm *et al.*, 2008); Cenozoic topaz rhyolites of the western USA (Christiansen *et al.*, 1983); and the Rio Grande rift (modified from White *et al.*, 1981). Dashed rectangle indicates the area shown in (b). (b) Outlines are shown for the Hideaway Park rhyolite (Shroba *et al.*, 2010), Precambrian Silver Plume granite (Wallace *et al.*, 1978), propylitic alteration about Red Mountain (Seedorff & Einaudi, 2004*a*), and other Oligocene rhyolite porphyry stocks in the region (Wallace *et al.*, 1978). Faults near the Henderson deposit (Wallace *et al.*, 1978) and selected regional faults (Kellogg *et al.*, 2008) are shown with black lines. Ages for the Hideaway Park tuff are from this study and Knox (2005), those for the Red Mountain intrusive complex are from Bookstrom *et al.* (1988) and Geissman *et al.* (1992), and that for molybdenite mineralization at Henderson is from Markey *et al.* (2007). (c) Cross-section showing the Red Mountain intrusions and the Henderson porphyry Mo deposit, modified from Seedorff & Einaudi (2004*b*). Cross-section location is shown schematically in (b) with a dashed line. Base hill shade map from USGS *The National Map* (http://viewer.nationalmap.gov).

sanidine grains was incrementally heated and two larger, single grains were fused in a single heating step and the liberated gas was expanded and purified by exposure to a cryogenic trap maintained at −135°C and two hot SAES™ GP50 getters. Following purification the gas was expanded online into a Mass Analyser Products™ 215-50 mass spectrometer and the Ar isotopes were measured in a static vacuum by peak jumping using an electron multiplier in analog mode.

Data were acquired during 10 measurement cycles and time zero intercepts were determined by best-fit linear and/or polynomial regressions to the data. Data were corrected for mass discrimination, blanks, radioactive decay, and interfering nucleogenic reactions. The neutron flux was monitored by laser fusion of >10 single Fish Canyon Tuff sanidine crystals (28·20 Ma ± 0·09 Ma, Kuiper *et al.*, 2008) at each closely spaced position within the irradiation package and resulted in neutron flux ratios reproducible to ±0·25% (2σ). Isotopic production ratios were determined from irradiated CaF_2 and KCl and for this study the following values were measured: $(^{36}Ar/^{37}Ar)_{Ca} = (2{\cdot}61 \pm 0{\cdot}05) \times 10^{-4}$; $(^{39}Ar/^{37}Ar)_{Ca} = (6{\cdot}81 \pm 0{\cdot}11) \times 10^{-4}$; $(^{38}Ar/^{39}Ar)_{K} = (1{\cdot}22 \pm 0{\cdot}03) \times 10^{-2}$). Cadmium shielding during irradiation prevented any measurable $(^{40}Ar/^{39}Ar)_{K}$.

Fourier transform infrared spectroscopy

Concentrations of H_2O and CO_2 dissolved in 57 homogenized melt inclusions were determined using a Thermo Nicolet Nexus 670 (University of Oregon) and a Bruker Hyperion (Centro de Geociencias campus Juriquilla) FTIR spectrometer, both interfaced with a Continuum IR microscope. Quantitative measurements of dissolved OH^-, molecular H_2O, and molecular CO_2 were obtained using Beer's Law,

$$c = MA/\rho d\varepsilon$$

where c is the concentration (weight fraction) of the absorbing species, M is the molecular weight of H_2O (18·02) or CO_2 (44·00), A is the absorbance intensity of the band of interest, ρ is the room temperature density of the rhyolitic glass, d is the thickness of the inclusion, and ε is the molar absorption coefficient for the species of interest.

To measure the absorbance intensity (A) for each spectrum, a linear background was modeled and subtracted from the peak height using OMNIC software. The total dissolved H_2O was measured using the band centered at ~3550 cm^{-1}. The molar absorption coefficient for water species in rhyolitic glasses varies with total water content, and we used the Beer's Law algorithm of Mandeville *et al.* (2002) to calculate total H_2O contents. Dissolved CO_2 was measured using the intensity of the 2350 cm^{-1} band (molecular CO_2) and the molar absorption coefficient from Behrens *et al.* (2004). The FTIR instrument and microscope stage were continuously purged with dry, CO_2-free air, so there was no interference by atmospheric CO_2.

The density of the glass was calculated from a simple summation of partial molar volumes following Luhr (2001). The thickness of the wafers containing the inclusions was first determined using the interference fringe method of Wyszocanski & Tani (2006). However, for most of the samples, the reflectance spectra collected were unsuitable to calculate the inclusion thickness owing to unequal spacing of interference patterns. Sample thicknesses were then measured using the high-precision Z-focus of an FEI field emission SEM, by first focusing on the surface of the inclusion then focusing on the glass slide next to the inclusion wafer and calculating the change in Z-focus positions (assuming a negligible amount of thin epoxy beneath the wafer). This technique successfully reproduced the thickness determined with a digital micrometer to within 3 μm and was expedient. Based on replicate FTIR analyses, 1σ precision is ±0·1 wt % for H_2O and ±20 ppm for CO_2.

SEM analysis and EPMA

These data were obtained at the USGS Denver Microbeam Laboratory. SEM-cathodoluminescence (CL) images were taken using a JEOL 5800LV electron microscope equipped with a Centaurus CL detector. Samples were analyzed at 20 kV with a beam current of 0·5 nA. CL images of melt inclusion-bearing quartz crystals show complex growth and resorption bands that can be used to assess the chronological evolution of melt inclusions in single crystals (e.g. Fig. 2).

The laboratory's JEOL 8900 Superprobe was operated using two setups optimized for analyses of major and minor element compositions (including Cl, S, F) of (1) hydrous glass inclusions and (2) mineral phases, and a third setup optimized for analysis of trace elements (Ti, Al, K) in quartz. Analysis of 58 homogenized glass inclusions was performed using a 15 kV accelerating potential, a 10 nA beam current, and a 10–20 μm spot size where possible to minimize volatilization. To avoid loss of Na and K, these elements were counted first to collect X-ray counts with minimal beam exposure. A correction was also applied for Na and K loss (Nielsen & Sigurdsson, 1981) using Probe for EPMA software. H_2O was measured using the water-by-difference method in the Probe for EPMA software (Donovan & Tingle, 1996). Analyses of Cl and F in the glass inclusions were well above the detection limit (100 ppm and 900 ppm, respectively), whereas most analyses of S were below the detection limit (80 ppm). Mineral phases were analyzed using a 15 kV accelerating potential, a 20 nA beam current, and a 1–5 μm spot size. Concentrations of Cl and F were well above the detection limit in biotite. Concentrations of Ti, Al, and K in quartz were measured using a 20 kV accelerating potential, a 100 nA beam current, and a 20 μm spot size. Ti was measured simultaneously on two spectrometers with LiF crystals following the general methods of Donovan *et al.* (2011) and Mercer & Reed (2013). Detection limits (99% confidence) achieved on spot analyses are 11 ppm Ti, 7 ppm Al, and 9 ppm K. Natural and

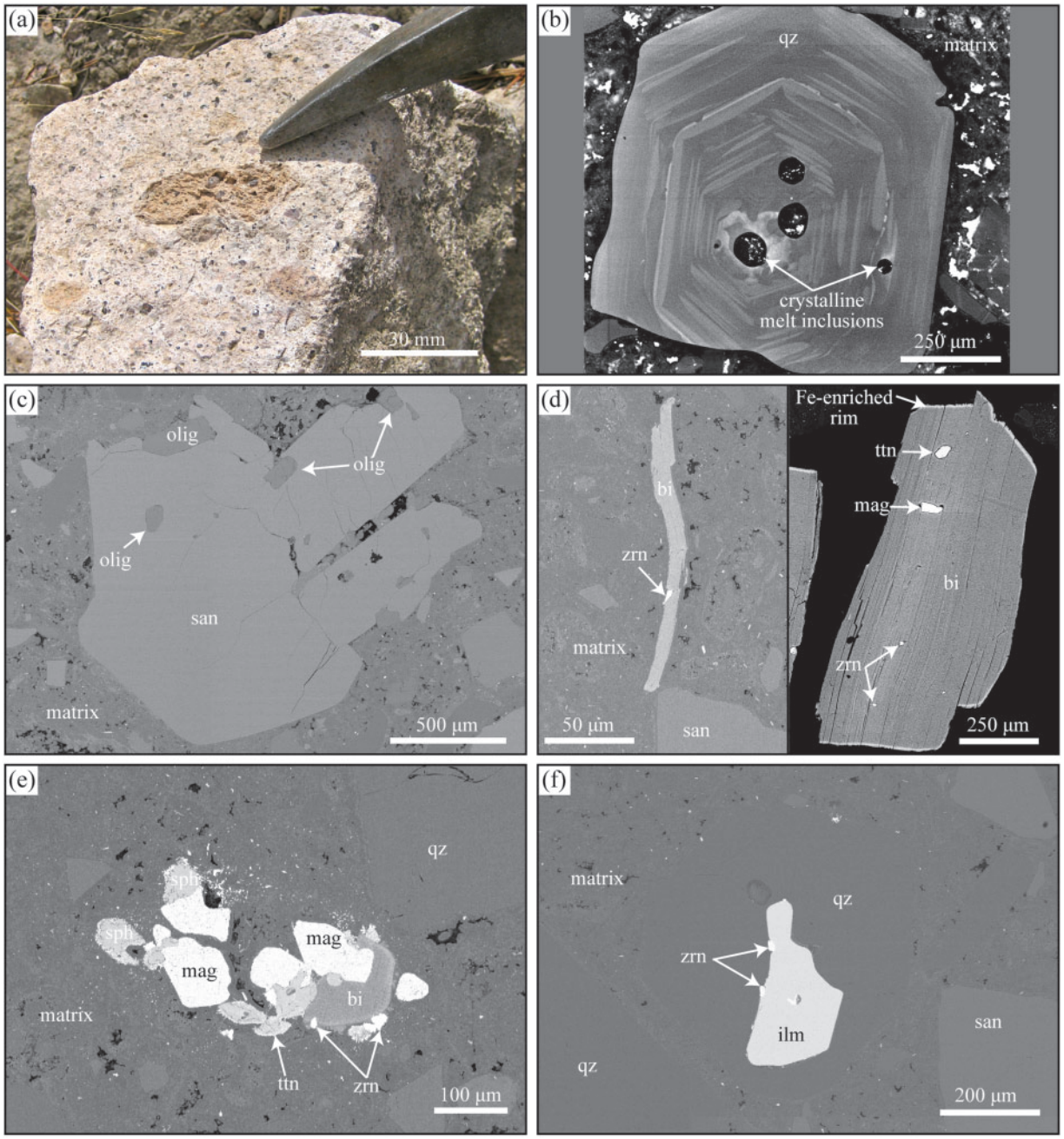

Fig. 2. Representative samples of the Hideaway Park tuff. (a) Hand sample of the upper tuff showing a large pumice clast and bipyramidal quartz phenocrysts suspended within the poorly welded tuff matrix; (b) SEM-CL image of a typical resorbed quartz phenocryst displaying a complex zoning history (euhedral growth bands and resorption surfaces) and several crystalline silicate melt inclusions. SEM-BSE images: (c) subhedral sanidine phenocryst with inclusions of oligoclase; (d) thin biotite phenocryst with an inclusion of zircon and larger biotite phenocryst with slightly Fe-enriched core and distinctly Fe-enriched rims; (e) typical cluster of magnetite intergrown with titanite, biotite, and zircon. (f) Quartz phenocryst with an inclusion of ilmenite and zircons. qz, quartz; san, sanidine; olig, oligoclase; bi, biotite; zrn, zircon; ilm, ilmenite; mag, magnetite; ttn, titanite.

synthetic minerals and glasses were used as standards for EPMA.

LA-ICP-MS analyses

Trace elements were determined for all inclusions by LA-ICP-MS at the USGS Denver Inclusion Analysis Laboratory. The system consists of a 193 nm ArF excimer laser with an energy homogenized beam profile coupled with a Thermo XSERIES II quadrupole mass spectrometer. A summary of the analytical conditions and data acquisition parameters used for this study is reported in Supplementary Data Electronic Supplement 1 (supplementary data are available for downloading at http://www.petrology.oxfordjournals.org).

A suite of 38 trace elements was analyzed, including those of particular geochemical interest at the Henderson porphyry Mo deposit (Mo, W, Pb, Zn, Cu, Bi,

Ag, and Mn). Spot sizes ranged from 24 to 160 μm (depending on the melt inclusion size and, for crystalline inclusions, the depth beneath the polished surface). One laser ablation setup was optimized for spot analyses of homogeneous glass inclusions and another for drilling through quartz and analyzing whole crystalline inclusions. The average detection limits and details of each of these analytical setups can be found in Electronic Supplement 1. The NIST610 glass was used as the primary reference material for all analyses and NIST612 was used as the secondary reference material in all runs. The preferred standard values for these glasses were obtained from Jochum *et al.* (2011). The average analytical precision for each element is reported in Tables 1 and 2. Major elements Ca and Al were also analyzed, and Al concentrations from EPMA were used as the internal standard for homogenized inclusions. For crystalline inclusions, the average Al content from all homogenized inclusions and pumice glass (13·3 ± 0·8 wt % Al_2O_3) was used as the internal standard, which imparts an additional error of ≤10%. This study reports the trace element compositions of 133 melt inclusions: 94 from the lower tuff (45 homogenized, 49 crystalline) and 39 from the upper tuff (26 homogenized, 13 crystalline).

RESULTS

Mineralogy, chemistry, and age of the Hideaway Park tuff

Hand specimens of the Hideaway Park tuff are light gray to light tan in color when fresh (Fig. 2a), and contain large (up to several millimeters) phenocrysts of shattered sanidine (~7–10 vol. %), plagioclase (~7–10 vol. %), and smoky bipyramidal quartz (~7 vol. %), with accessory (<1 vol. % each) biotite, magnetite, ilmenite, titanite, zircon, and apatite. The tuff is poorly to moderately welded and the ashy matrix is variably devitrified and/or silicified. The stratigraphy of the Hideaway Park tuff is not well documented because there are few outcrops, many of which are poorly exposed or concealed by glacial deposits. The analyzed phenocrysts and melt inclusions for this study come from two outcrops: the 'canal' outcrop and the 'quarry cliff' outcrop. The canal outcrop is in contact with the Proterozoic Routt plutonic suite and is from the lower portion of the tuff (Fig. 1). It is light gray in color, moderately welded, devitrified and slightly silicified, and contains ~2–3 vol. % angular lithic fragments ≤10 mm in diameter, relatively few (~5–7 vol. %) clasts of tan pumice ≤20 mm in diameter, and ~7–10 vol. % shattered, smoky quartz ≤5 mm in diameter. The quarry cliff outcrop is in contact with Holocene to middle Pleistocene colluvium and alluvium and is from the upper portion of the tuff (Fig. 1). It is light tan in color, poorly welded, and only slightly devitrified and unsilicified. It contains few (≪1 vol. %) large, rounded lithic clasts ≤30 mm in diameter (including pink granite and hornblende gneiss that are probably Precambrian in age), a much higher proportion (~15–20 vol. %) of tan pumice, including tube pumice, ranging in size up to ~60 mm, and ~5–7 vol. % smoky quartz shards and bipyramids ≤5 mm in diameter. The pumice clasts contain 15–25 vol. % smoky, euhedral bipyramidal quartz phenocrysts up to ~6 mm in diameter. The rocks at the quarry cliff outcrop are lower in density than those at the canal outcrop, and contain gas cavities commonly as large as ~3 cm in diameter (e.g. Taylor *et al.*, 1968).

Major and trace element bulk-rock analyses of the Hideaway Park tuff are presented in Table 1. It is a high-silica, slightly peraluminous rhyolite with similar total alkali contents to average rhyolite, other topaz rhyolites of the western USA, and rhyolitic stocks of the Henderson porphyry Mo deposit (Fig. 3a; Stein & Hannah, 1985; Bookstrom *et al.*, 1988; Christiansen *et al.*, 2007). Its rare earth element (REE) pattern is similar in shape to that of the Henderson rhyolite stocks (Stein & Hannah, 1985) except that it is shifted to slightly higher values (Fig. 3b). The Hideaway Park tuff has a somewhat flat REE pattern (La/Yb_N ~7) and a strong Eu anomaly (Eu/Eu* ~0·2) that mimic the nearly flat patterns and pronounced negative Eu anomalies characteristic of topaz rhyolites (Christiansen *et al.*, 1983, 1986).

Sanidine from the lower tuff (this study) yielded single grain fusion ages of 27·82 ± 0·28 Ma and 27·76 ± 0·34 Ma, respectively, and a third aliquot yielded a $^{40}Ar/^{39}Ar$ plateau age of 27·72 ± 0·28 Ma (mean age 27·77 ± 0·34 Ma; all errors 2σ; Supplementary Data Electronic Supplement 2). Applying the same standard age (28·20 Ma) for Fish Canyon sanidine (Kuiper *et al.*, 2008) as used in this study to the sanidine from the upper tuff (Knox, 2005) yields a revised $^{40}Ar/^{39}Ar$ isochron age of 27·49 ± 0·24 Ma (2σ). Although the lower tuff may be slightly older than the upper tuff within 1σ error, the ages are indistinguishable within 2σ error (Fig. 4). Thus the two units could represent products of two separate eruptions spaced closely in time, or a single eruption. Each $^{40}Ar/^{39}Ar$ date is within the age range of Red Mountain intrusive rocks (Bookstrom *et al.*, 1988; Geissman *et al.*, 1992) and the ages of the upper and lower tuffs are identical within 2σ to the high-precision Re–Os date [27·656 ± 0·022 Ma (2σ); Markey *et al.*, 2007] from Henderson molybdenite.

Mineral petrography and compositions

In this study, we used mineral compositions to constrain the Hideaway Park pre-eruptive magma temperature, fO_2, and activity of TiO_2 (a_{TiO2}), and to identify any chemical resemblance to corresponding minerals in the Red Mountain intrusive complex. The minerals analyzed represent the main phenocryst populations and accessory minerals, as opposed to microphenocrysts. Average mineral analyses, thermobarometry and oxygen barometry results are given in Table 2 and single mineral analyses are reported in Supplementary Data Electronic Supplement 3.

Table 1: Average major and trace element compositions, Ar–Ar age, estimates of a_{TiO2}, and inclusion entrapment temperature for the Hideaway Park tuff

	Hideaway Park upper tuff bulk-rock[1]	H.P. upper tuff pumice matrix glass[1]	Average H.P. lower tuff melt inclusions[2]	Average H.P. upper tuff melt inclusions[2]	Average bulk western US topaz rhyolite[5]	Average rhyolite[6]
Age (Ma):	N.A.	N.A.	27·7 ± 0·1[3]	27·5 ± 0·1[4]		
n:	2	1	83	36		
Major elements (wt %)						
SiO_2	78·36	75·72	77·27(86)	77·4(1·8)	76·02	77·88
TiO_2	0·12	0·10	0·09(2)	0·09(4)	0·08	0·08
Al_2O_3	11·13	12·80	13·22(51)	13·4(1·0)	13·15	12·54
FeO*[7]	0·89	0·59	0·61(8)	0·55(13)	0·93	0·68
MgO	0·02	0·02	0·02(1)	0·02(1)	0·12	0·04
MnO	0·08	0·05	0·12(1)	0·13(1)	0·08	0·02
CaO	0·38	0·34	0·55(9)	0·57(9)	0·57	0·42
Na_2O	3·16	3·83	3·30(38)	2·90(71)	3·95	3·50
K_2O	4·39	5·11	4·65(32)	4·70(40)	4·69	4·84
P_2O_5	0·06	0·03	0·01(0)	b.d.l.	0·03	0·01
Total	98·59	98·59	100·00	100·00	99·62	100·01
F (ppm)	N.A.	1300[8]	7600(1000)	6700(1600)	4029	480
S (ppm)	N.A.	N.A.	98(11)	110(40)	N.A.	284
Cl (ppm)	N.A.	360(30)[8]	2900(200)	2800(300)	775	754
H_2O (wt %; water-by-difference)	N.A.	0·75(47)[8]	n.a.	n.a.	0·38	5·14
molar $Al_2O_3/(Na_2O + K_2O + CaO)$	1·05	1·03	1·16(6)	1·24(11)	1·05	1·07
a_{TiO2}[9]	N.A.	N.A.	0·35	0·34		
Volatile elements by FTIR						
H_2O (wt %)	N.A.	N.A.	1·9(1·5)	1·3(4)		
CO_2 (ppm)	N.A.	N.A.	290(170)	130(100)		
Maximum H_2O(wt %)	N.A.	N.A.	5·80	2·46		
Maximum CO_2 (ppm)	N.A.	N.A.	597	338		180
Entrapment pressure (MPa)[10]	n.a.	n.a.	290	60		
Trace elements (ppm)						
Li	50·5	67·5	1600(600)	3700(1600)	146	*71*
Be	7·7	9·4	16(3)	16(3)	15	4·1
B	N.A.	N.A.	36(8)	39(5)	15	*41*
Sc	3·6	3·9	6(1)	7(1)	3	*4*
Ti	438	541	490(110)	460(80)		*554*
Mn	512	598	990(120)	1000(110)	620	155
Fe	5200	4720	4300(900)	3500(800)		*5000*
Cu	6	112	8(6)	9(7)	1	6
Zn	22·3	23·9	200(300)	300(700)	25	38
Ga	23·4	23·6	25(3)	25(2)	49	
As	1·8	6·3	6(1)	7(3)		3·5
Rb	494	673	760(150)	760(70)	562	102
Sr	25·4	8·5	2(1)	1·0(6)	31	*34*
Y	43·1	15·8	40(7)	40(6)	96	*21*
Zr	N.A.	N.A.	89(15)	87(18)	117	136
Nb	66	87	140(30)	140(20)	70	28
Mo	2·3	4·2	15(3)	15(3)	8	1·0
Ag	<0·01	<0·01	0·1(0)	0·1(1)		0·04
Sn	N.A.	N.A.	9(1)	10(2)	20	3·6
Sb	0·1	0·4	0·7(7)	0·6(1)		0·35
Cs	2·9	4·1	16(4)	17(2)	25	*6*
Ba	50·3	79·4	2(2)	2(2)	88	*371*
La	53·2	30·4	58(28)	50(14)		*21*
Ce	82·2	57·1	82(10)	79(13)		*46*
Nd	27·8	N.A.	20(3)	19(3)		*17*
Sm	4·5	N.A.	3·3(5)	3·1(5)		*3·4*
Eu	0·3	N.A.	0·1(1)	0·1(0)		*0·2*
Gd	3·8	N.A.	2·7(5)	2·8(5)		*2·4*
Dy	4·6	N.A.	3·9(6)	3·7(6)		*3·5*
Er	3·5	N.A.	3·7(7)	3·7(7)		*2·4*
Yb	4·8	N.A.	6(1)	6(1)		*3·0*
Ta	N.A.	N.A.	11(2)	12(2)	11	2·3
W	N.A.	N.A.	9(2)	9(2)		2·4

(continued)

Table 1: (continued)

	Hideaway Park upper tuff bulk-rock[1]	H.P. upper tuff pumice matrix glass[1]	Average H.P. lower tuff melt inclusions[2]	Average H.P. upper tuff melt inclusions[2]	Average bulk western US topaz rhyolite[5]	Average rhyolite[6]
Tl	2·01	2·39	4(1)	4(1)		
Pb	30·5	37·5	38(5)	36(4)	43	21
Bi	<0·06	0·08	0·8(2)	0·8(1)		0·12
Th	75·2	49·8	49(11)	46(12)	61	26
U	14·8	20·2	26(5)	27(4)	23	5
Zr-saturation entrapment temp. (°C)[11]	n.a.	n.a.	745(14)	746(25)		

Numbers in parentheses next to each analysis represent 1σ standard deviation on average of multiple analyses. Errors given in terms of least unit cited [e.g. 77·27(86) represents 77·27 ± 0·86]. *n*, number of analyses; N.A., not analyzed; n.a., not applicable; b.d.l., below the 99% detection limit. Average analytical precision (1σ) for electron microprobe analyses (based on 2–6 replicate analyses): SiO_2 ± 0·66, TiO_2 ± 0·02, Al_2O_3 ± 0·26, FeO* ± 0·06, MgO ± 0·01, MnO ± 0·02, CaO ± 0·03, Na_2O ± 0·69, K_2O ± 0·20, F ± 0·13, S ± 0·003, Cl ± 0·01. Average analytical precision (1σ) for LA-ICP-MS analyses (crystalline inclusion setup): Li (3%), Be (5%), B (5%), Sc (8%), Ti (5%), Mn (3%), Fe (4%), Cu (4%), Zn (1%), Ga (4%), As (6%), Rb (3%), Sr (5%), Y (4%), Zr (4%), Nb (4%), Mo (4%), Ag (5%), Sn (4%), Sb (5%), Cs (4%), Ba (5%), La (4%), Ce (4%), Nd (4%), Sm (5%), Eu (6%), Gd (5%), Dy (5%), Er (4%), Yb (5%), Ta (4%), W (4%), Tl (4%), Pb (4%), Bi (6%), Th (4%), U (4%).

[1]Data collected by WD-XRF and ICP-MS.

[2]Melt inclusion major element analyses are normalized anhydrous; major element data, F, S, and Cl collected by electron microprobe; H_2O and CO_2 by FTIR; and trace element data by LA-ICP-MS.

[3]Sanidine ^{40}Ar–^{39}Ar age (this study).

[4]Sanidine ^{40}Ar–^{39}Ar age (Knox, 2005; calculated from this study).

[5]Average of ~150 rock analyses from review by Christiansen *et al.* (1986).

[6]Average bulk rhyolite compiled by Robb (2005). Additional melt inclusion analyses are given in italics from the Taupo Volcanic Center (Hervig *et al.*, 1989; Barclay *et al.*, 1996; Liu *et al.*, 2006, 2007; Shane *et al.*, 2007, 2008; Smith *et al.*, 2010; Johnson *et al.*, 2011) and the Bishop Tuff (Anderson *et al.*, 1989; Skirius *et al.*, 1990; Lu *et al.*, 1992; Christensen & Halliday, 1996; Wallace *et al.*, 1999, 2003; Anderson *et al.*, 2000; Schmitt & Simon, 2004; Roberge *et al.*, 2013).

[7]All Fe reported as FeO.

[8]Data from electron microprobe analysis of fused matrix glass bead.

[9]a_{TiO2} calculated using the model of Hayden & Watson, 2007.

[10]Entrapment pressure calculated using solubility model of Liu *et al.* (2005) and melt inclusion with the highest H_2O and CO_2 contents.

[11]Zr-saturation thermometer of Watson & Harrison (1983).

Quartz

Phenocrysts of quartz are euhedral with resorbed rims. SEM-CL images of quartz show evidence of complex zoning (Fig. 2b) with periodic euhedral growth and resorption bands. Quartz contains relatively abundant inclusions of silicate melt and sparse subhedral grains of ilmenite and zircon. One quartz phenocryst analyzed from the lower tuff (out of a total of >100 phenocrysts examined) contains a small (~20 μm) grain of molybdenite (confirmed by EPMA wavelength-dispersive spectrometer wavescans), and one other quartz phenocryst contains a small (<10 μm) grain of pyrite (confirmed by SEM energy-dispersive spectrometry); these represent the only two sulfide mineral inclusions identified in all of the quartz phenocrysts analyzed. Electron microprobe trace element analyses of quartz (Table 2) show small variations in Ti, K and Al. Titanium concentrations range from 62 to 72 ppm; higher Ti concentrations correspond to CL-bright bands in quartz. Quartz crystallization temperatures calculated using the titanium-in-quartz calibration of Huang & Audétat (2012) average 840 ± 18°C (Table 2). For this calculation, we assumed a pressure of 290 MPa, which is a minimum estimate constrained by the highest entrapment pressure we calculated for the melt inclusion with the highest H_2O and CO_2 contents (see below). Using a pressure estimate ~50 MPa higher would result in an ~15°C increase in calculated temperatures. We assume an a_{TiO2} of 0·35 following our Fe–Ti-oxide oxygen-barometer results (see below). An increase in a_{TiO2} of 0·5 would result in a decrease in calculated temperatures by ~100°C (Huang & Audétat, 2012).

Feldspars

Sanidine ($Or_{59}Ab_{39}An_2$) and oligoclase ($Or_7Ab_{71}An_{22}$) phenocrysts are typically subhedral and homogeneous in composition (Table 2). They contain few silicate melt inclusions; some sanidine phenocrysts host inclusions of oligoclase (Fig. 2c) and, less commonly, ilmenite. Two-feldspar temperatures calculated following Putirka (2008) are ~100°C cooler than the Ti-in-quartz temperatures and average 733 ± 9°C (Table 2).

Biotite

Biotite phenocrysts are sparse (≤1 vol. %) and typically observed as thin books ~50–200 μm in length (Fig. 2d). In the lower tuff, biotite books are generally euhedral to subhedral and cohesive, whereas most of those in the upper tuff are expanded, display ragged cleavage planes, and appear out of equilibrium. Biotite compositions vary from $X_{phlogopite}$ ~0·57 to 0·15 (Fig. 5), but

Table 2: Representative chemical analyses of phenocrysts from the Hideaway Park tuff and results from thermobarometry and oxygen-barometry

	Quartz	Sanidine	Oligoclase	Magnetite	Ilmenite		Biotite
n	53	46	43	4	5		81
Element (wt % unless noted)							
SiO_2	N.A.	66·53(28)	66·40(48)	0·21(3)	b.d.l.		40·0(1·7)
TiO_2	N.A.	0·03(1)	0·02(1)	6·7(3·1)	43·76(31)		2·66(68)
Al_2O_3	N.A.	18·83(12)	21·46(32)	0·81(11)	0·05(1)		13·4(1·9)
FeO*[1]	N.A.	0·12(1)	0·16(1)	78·5(3·9)	42·24(38)		18·7(3·1)
FeO	N.A.	n.a.	n.a.	32·0(1·7)	35·94(36)		n.a.
Fe_2O_3	N.A.	n.a.	n.a.	51·7(6·3)	6·99(20)		n.a.
MgO	N.A.	b.d.l.	b.d.l.	0·02(0)	0·04(2)		13·4(2·8)
MnO	N.A.	0·02(1)	0·02(1)	3·65(95)	10·72(28)		1·48(78)
CaO	N.A.	0·19(1)	2·60(16)	0·02(1)	b.d.l.		b.d.l.
Na_2O	N.A.	4·39(11)	9·23(9)	N.A.	N.A.		0·43(9)
K_2O	N.A.	10·22(14)	1·38(7)	N.A.	N.A.		9·62(28)
V_2O_3	N.A.	N.A.	N.A.	0·04(1)	0·03(0)		N.A.
Cr_2O_3	N.A.	N.A.	N.A.	b.d.l.	b.d.l.		N.A.
ZnO	N.A.	N.A.	N.A.	0·17(3)	0·07(4)		0·09(4)
Rb_2O	N.A.	N.A.	N.A.	N.A.	N.A.		0·14(8)
BaO	N.A.	0·09(2)	0·08(1)	N.A.	N.A.		b.d.l.
NiO	N.A.	N.A.	N.A.	0·56(9)	0·46(14)		N.A.
Nb_2O_5	N.A.	N.A.	N.A.	0·08(0)	1·48(7)		N.A.
F	N.A.	b.d.l.	b.d.l.	N.A.	N.A.		4·24(60)
Cl	N.A.	0·03(0)	0·03(0)	N.A.	N.A.		0·19(6)
Ti (ppm)	66(9)	N.A.	N.A.	N.A.	N.A.		N.A.
Al (ppm)	108(11)	N.A.	N.A.	N.A.	N.A.		N.A.
K (ppm)	18(8)	N.A.	N.A.	N.A.	N.A.		N.A.
Total	n.a.	100·34(27)	100·21(55)	95·81(65)	99·40(27)		100·00
Or	n.a.	0·59(1)	0·07(0)	n.a.	n.a.	$X_{phlogopite}$[2]	0·38(10)
Ab	n.a.	0·39(1)	0·71(1)	n.a.	n.a.	X_{Mg}[3]	0·56(9)
An	n.a.	0·02(0)	0·22(1)	n.a.	n.a.		
No. of cations:		Cations per 8 O	Cations per 8 O	Cations per 4 O	Cations per 3 O	Cations per 22 O + 4(OH, F, Cl)	
Si	n.a.	3·00(1)	2·88(1)	0·01(1)	b.d.l.	Si	5·82
Ti	n.a.	0(0)	0(0)	0·20(9)	0·86(0)	^{iv}Al	2·17
Al	n.a.	1·00(1)	1·11(2)	0·04(1)	0·001(0)	Sum iv	8
Fe	n.a.	0·01(1)	0·01(0)	n.a.	n.a.	Ti	0·29
Fe^{2+}	n.a.	n.a.	n.a.	1·06(6)	0·78(1)	^{vi}Al	0·13
Fe^{3+}	n.a.	n.a.	n.a.	1·54(18)	0·14(0)	Fe^{2+}	2·28
Mg	n.a.	b.d.l.	b.d.l.	0·001(1)	0·001(1)	Mg	2·9
Mn	n.a.	0(0)	0(0)	0·12(3)	0·24(1)	Mn	0·18
Ca	n.a.	0·01(0)	0·12(1)	0·001(1)	b.d.l.	Sum vi	5·79
Na	n.a.	0·39(2)	0·79(1)	N.A.	N.A.	Ca	b.d.l.
K	n.a.	0·59(2)	0·80(0)	N.A.	N.A.	Na	0·12
Ni	n.a.	N.A.	N.A.	0·02(0)	0·01(1)	K	1·78
Zn	n.a.	N.A.	N.A.	0·005(1)	0·001(1)	Sum xii	1·92
Nb	n.a.	N.A.	N.A.	0·001(1)	0·02(0)		
Total cations	n.a.	4·99(0)	4·99(1)	3·01(0)	2·05(0)	Total cations	15·7
Thermo- or oxygen-barometry							
	Assumed P (MPa)	Assumed P (MPa)		Mag–ilm T (°C) (Fe–Ti exchange)[4]			X_{Mg}-Ti-in-biotite T (°C)[5]
	290	290		730(50)			671(38)
	Assumed a_{TiO2}	Two-feldspar T (°C)[6]		log fO_2[4]			
	0·35	733(9)		NNO – 0·3(0·5)			
	Ti-in-quartz T (°C)[7]			a_{TiO2}[4]			
	840(18)			0·35			

Numbers in parentheses next to each analysis represent 1σ standard deviation on average of multiple analyses. Errors given in terms of least unit cited [e.g. 66·53(28) represents 66·53 ± 0·28]. *n*, number of analyses; N.A., not analyzed; n.a., not applicable; b.d.l., below the 99% detection limit. Average analytical precision (1σ) for electron microprobe analyses (based on 2–3 replicate analyses): SiO_2 ± 0·75, TiO_2 ± 0·31, Al_2O_3 ± 0·32, FeO* ± 0·25, MgO ± 0·22, MnO ± 0·07, CaO ± 0·21, Na_2O ± 0·09, K_2O ± 0·17, V_2O_3 ± 0·02, Cr_2O_3 ± 0·01, ZnO ± 0·05, Rb_2O ± 0·03, BaO ± 0·03, NiO ± 0·21, Nb_2O_5 ± 0·01, F ± 0·14, Cl ± 0·01.

[1]All Fe reported as FeO.

[2]$X_{phlogopite}$ = mole fraction Mg/∑vi cations.

[3]X_{Mg} = molar [Mg/(Mg + Fe^{2+})].

[4]Calculated using the geothermobarometer of Ghiorso & Evans (2008).

[5]Temperature calculated using the thermometer of Henry *et al.* (2005).

[6]Calculated using the revised thermobarometer of Putirka (2008).

[7]Calculated using the thermobarometer of Huang & Audétat (2012).

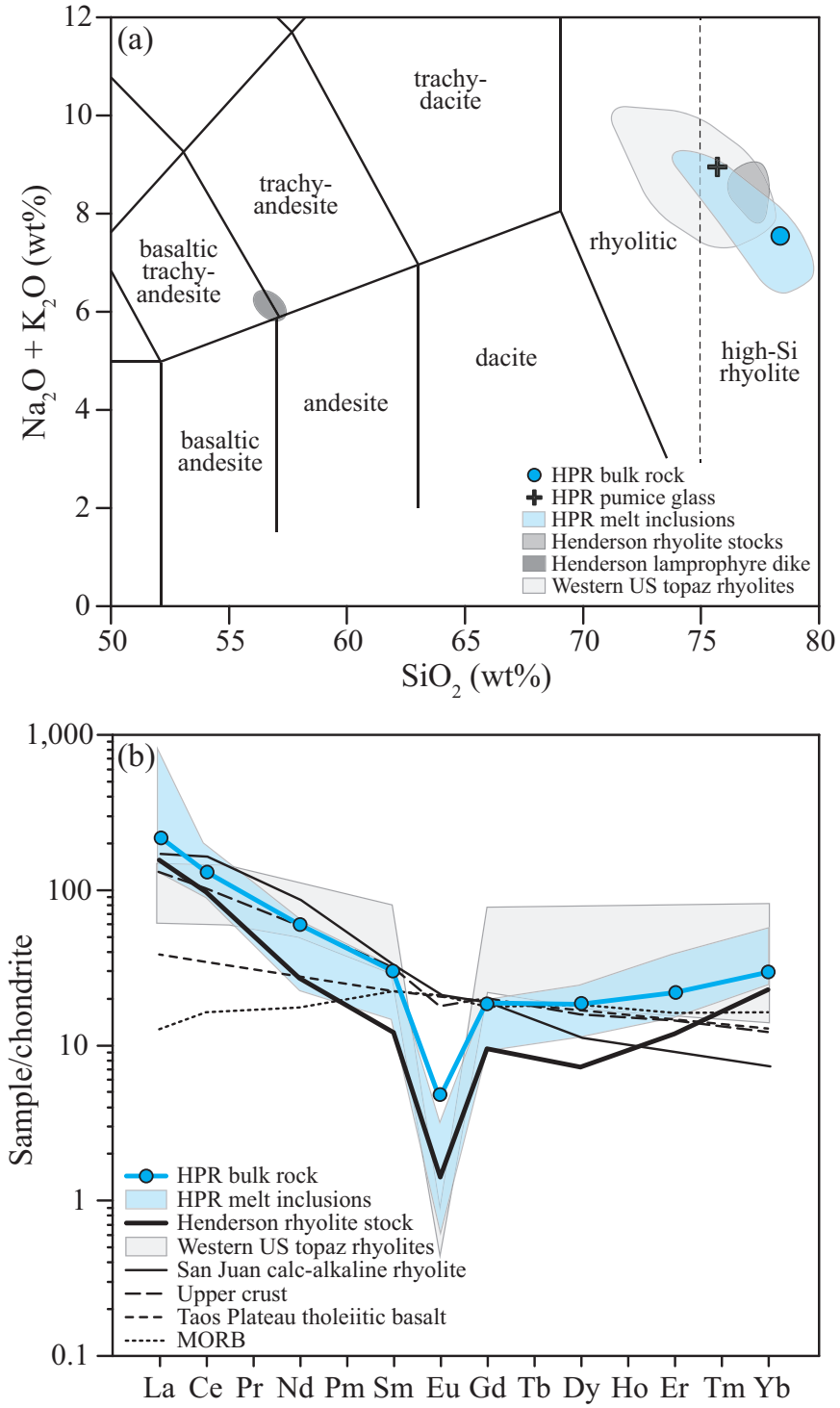

Fig. 3. Major and trace element bulk-rock and melt inclusion trends for the Hideaway Park tuff. (a) Total alkali–silica diagram; plotted for comparison are rhyolite stocks from the Henderson porphyry Mo deposit (Stein & Hannah, 1985; Bookstrom *et al.*, 1988), lamprophyre (kersantite) dikes from the Henderson deposit (Bookstrom *et al.*, 1988), and topaz rhyolites of the western USA (Christiansen *et al.*, 2007). HPR, Hideaway Park rhyolite. (b) Chondrite-normalized (McDonough & Sun, 1995) REE diagram showing bulk-rock and melt inclusion patterns for the HPR, which is similar in pattern to the Seriate stock intrusions from the Henderson porphyry Mo deposit (Stein & Hannah, 1985). Plotted for comparison are topaz rhyolites from the western USA (Christiansen *et al.*, 1983, 1986), calc-alkaline rhyolite from Summer Coon volcano in the San Juan Mountains, CO (Zielinski & Lipman, 1976), upper crust (Rudnick & Gao, 2003), Taos Plateau tholeiitic basalts (Farmer, 2003), and mid-ocean ridge basalt (MORB) (Sun & McDonough, 1989). The 1σ errors for LA-ICP-MS analyses are reported in Table 1.

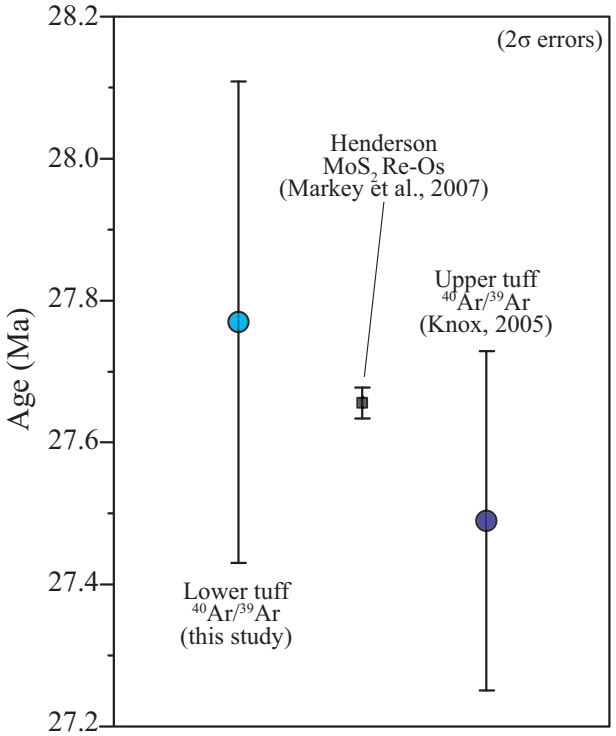

Fig. 4. Ages of the Hideaway Park tuff relative to MoS_2 mineralization at Henderson (this study; Knox, 2005; Markey *et al.*, 2007). (All uncertainties 2σ.)

single grains are typically unzoned and none appear xenocrystic. Some of the larger grains show faintly Fe-enriched cores with distinct Fe-rich rims (Fig. 2d). Biotite phenocrysts are most notably enriched in F (2·5–5·0 wt %) and Cl (0·15–0·39 wt %), and F generally decreases with decreasing $X_{phlogopite}$, consistent with Fe–F avoidance in biotite (Fig. 5; e.g. Mason, 1992). These F concentrations are higher than those in biotite from the Pine Grove topaz rhyolite (J. Lowenstern, personal communication), similar to those in biotite from the Honeycomb Hills rhyolite (Congdon & Nash, 1991), and overlap with biotite from igneous rhyolitic intrusions and ore-related hydrothermal veins from the Henderson porphyry Mo deposit (Gunow *et al.*, 1980; Carten *et al.*, 1988*a*; Seedorff & Einaudi, 2004*a*). Hideaway Park tuff biotite phenocrysts also contain significantly more F than biotite from the lamprophyre (kersantite) dike at Henderson (Carten *et al.*, 1988*a*). Chlorine contents of biotite from the Hideaway Park tuff exhibit a similar range to that in the Pine Grove topaz rhyolite and the lamprophyre dike at Henderson, but are higher than those of biotite in the Henderson rhyolitic intrusions and hydrothermal veins (Fig. 5). Biotite occasionally occurs intergrown with zircon, magnetite, titanite (Fig. 2d and e), feldspar, and less commonly apatite and REE-phosphate. No pyrrhotite or immiscible sulfide melts were observed in biotite. Biotite temperatures calculated using the thermometer of Henry *et al.* (2005) provide the lowest crystallization temperature estimates, averaging 671 ± 38°C (Table 2).

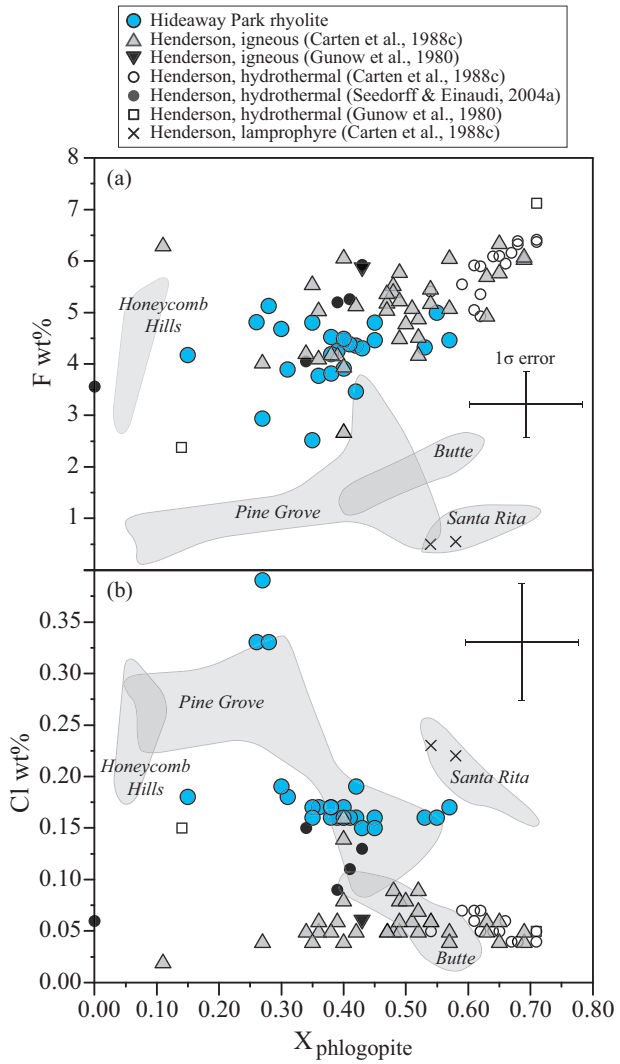

Fig. 5. Composition of (a) F and (b) Cl of biotite from the Hideaway Park rhyolite and from igneous intrusions and hydrothermal veins from the Henderson porphyry Mo deposit (Gunow *et al.*, 1980; Carten *et al.*, 1988*b*; Seedorff & Einaudi, 2004*a*). For reference, igneous biotite data are shown from the Pine Grove topaz rhyolite, UT (comagmatic with the Pine Grove porphyry Mo deposit; J. Lowenstern, personal communication) and the Honeycomb Hills rhyolite, UT (eruptive pegmatite; Congdon & Nash, 1991), and hydrothermal vein biotite from the Butte porphyry Cu–Mo deposit, MT (Zhang, 2000) and Santa Rita porphyry Cu deposit, NM (Jacobs & Parry, 1979). $X_{phlogopite}$ = mole fraction Mg/$\sum$vi cations (Table 2).

Magnetite and ilmenite

Magnetite grains are subhedral, typically $\leq$100 μm in diameter, and are found in trace amounts (<1 vol. %). They vary somewhat in composition, particularly in Fe, Ti, and Mn contents (Table 2). Magnetite is spongy in texture and commonly intergrown with titanite (which contains ~1·3 wt % F and usually shows a reaction rim where exposed to the matrix), zircon, quartz, and less commonly biotite (Fig. 2e). In contrast, ilmenite grains are smooth and relatively homogeneous (Table 2), are only observed intergrown with zircon and quartz or as occasional inclusions in quartz phenocrysts (Fig. 2f), and are significantly less abundant than magnetite.

No pyrrhotite or immiscible sulfide melts were observed in magnetite or ilmenite. The intergrown assemblage titanite + magnetite + quartz signifies an $fO_2 \geq$ NNO – 1 (where NNO is nickel–nickel oxide) (Wones, 1989). Magnetite and ilmenite are not observed intergrown so we do not have clear evidence that they grew in equilibrium; however, they are intergrown with a shared mineralogy. Their compositions are within ~0·2 log units of the Bacon & Hirshmann (1988) equilibrium test line, slightly outside the 2σ envelope. Application of the revised Fe–Ti two-oxide geothermometer and oxygen-barometer of Ghiorso & Evans (2008) results in a magnetite–ilmenite temperature of ~730°C (± 50°C), an fO_2 of ~NNO – 0·3 (±0·5), and an a_{TiO2} of 0·35 (Table 2). Although these magnetite–ilmenite data are not robust, given the apparent departure from equilibrium, they provide a first-order estimate. The fO_2 estimates are comparable with previous estimates for porphyry Mo deposition (e.g. Ohmoto & Goldhaber, 1997; Audétat *et al.*, 2011).

Christiansen *et al.* (1983, 1986) estimated temperatures ranging from 605 to 830°C and oxygen fugacities of ~NNO – 0·5 for topaz rhyolites from the western USA. Overall, the thermobarometry and oxygen-barometry results for the Hideaway Park rhyolite agree well with these estimates. Although the calculated temperatures range to remarkably high values given the volatile-rich character of the rhyolite, particularly for quartz, they are well within the range of sub-liquidus temperatures according to the hydrous topaz rhyolite phase relations of Webster *et al.* (1987).

Melt inclusion and pumice glass compositions

Quartz-hosted melt inclusions in the Hideaway Park tuff are composed of rhyolitic and feldspathic glass (variably devitrified), crystals of alkali feldspar, quartz, magnetite, fluorite, zircon, ilmenite, and monazite; a few contain bubbles. We identified three optically distinct morphologies of melt inclusion (Fig. 6). The most abundant inclusions are tan, partly crystalline inclusions (Fig. 6a) that vary in size (10–200 μm) and are generally equant with rounded, negative bipyramidal forms. Brown, mostly crystalline to opaque inclusions (Fig. 6b) are less abundant, and are typically spherical to oblate in shape and large (50–200 μm, long dimension). Clear, partly crystalline inclusions (Fig. 6c) are the least abundant, and are usually small (~20 μm), equant with rounded bipyramidal forms, and contain one or more bubbles. Despite their difference in morphology, there is no geochemical distinction between these types, and we conclude that their appearance must be a function of the degree of crystallization. After homogenization, the melt inclusions are typically clear and do not contain any bubbles (Fig. 6d). Average major and trace element analyses of melt inclusions from the upper and lower tuff are presented in Table 1, along with the calculated a_{TiO2} (Hayden & Watson, 2007) and Zr-saturation thermometry results (Watson & Harrison, 1983). Single inclusion analyses for both unhomogenized and

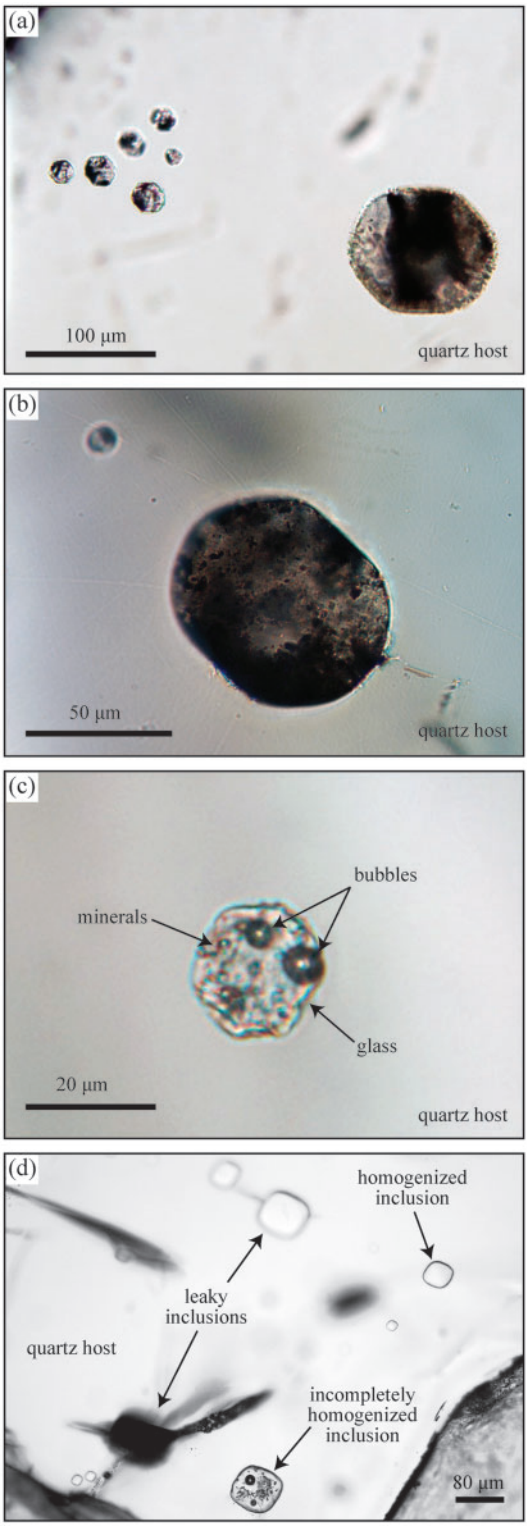

Fig. 6. Photomicrographs exhibiting the variety of morphologies of quartz-hosted crystalline silicate melt inclusions analyzed from the Hideaway Park tuff. (a) Tan, partly crystalline inclusions are the most abundant inclusion type; (b) brown, mostly crystalline to opaque inclusions are less abundant; (c) clear, partly crystalline inclusions are least abundant; (d) experimental run product showing examples of fully enclosed, homogenized inclusions used in this study, incompletely homogenized inclusions (not analyzed), and leaky inclusions (not analyzed). This quartz phenocryst was homogenized at 140 MPa and 1010°C for 15 min.

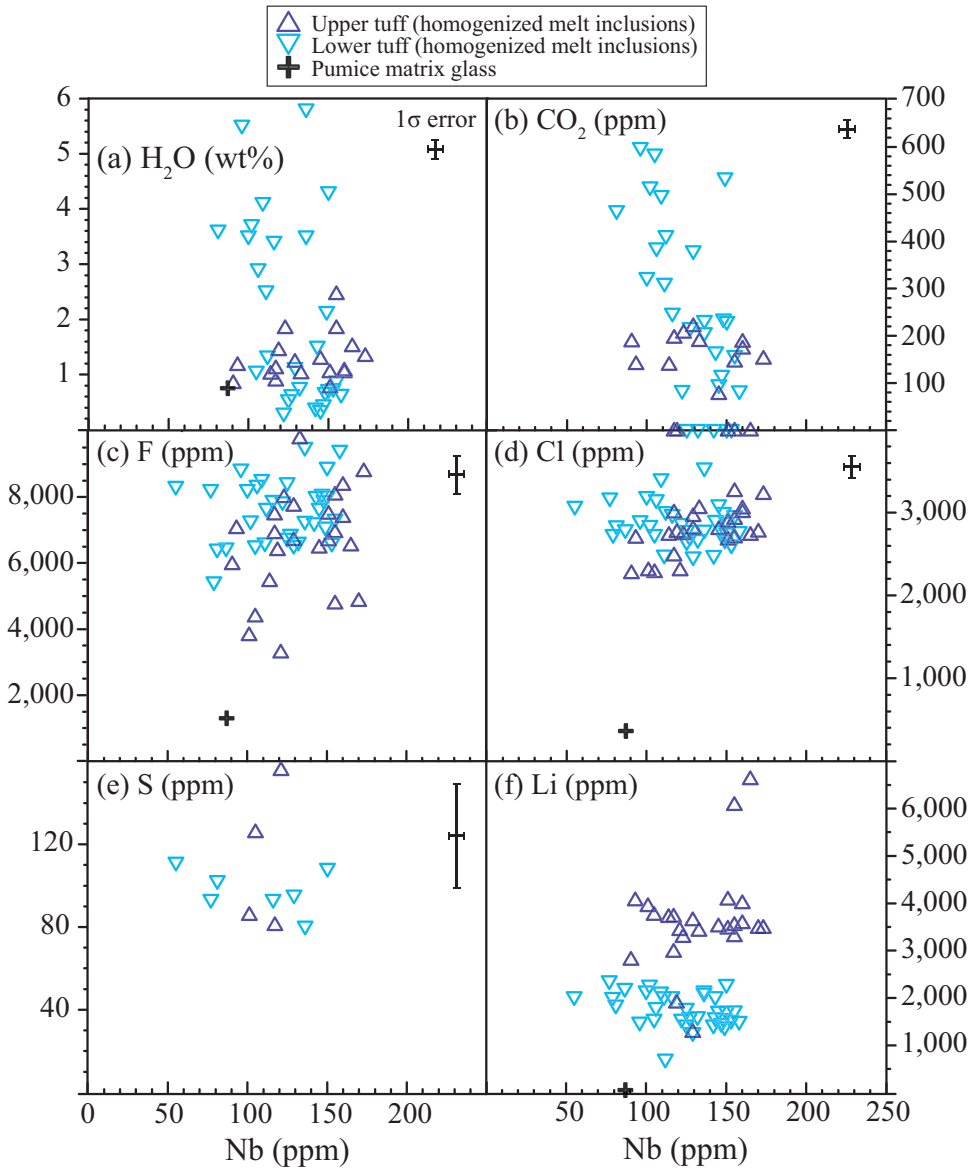

Fig. 7. Concentrations of (a) H_2O, (b) CO_2, (c) F, (d) Cl, (e) S, and (f) Li in melt inclusions and pumice matrix glass plotted versus Nb, which is used as an index for the evolution of the melt. The 1σ errors for Li are smaller than the symbols.

homogenized inclusions are provided in Electronic Supplement 1.

Major elements and volatiles

Melt inclusion compositions are dominantly high-silica rhyolites ranging from ~74 to 80 wt % SiO_2 and from ~6 to 9 wt % total alkalis (Fig. 3a; Table 1). Melt inclusions are more peraluminous than the whole-rock composition [molar $Al_2O_3/(Na_2O + K_2O + CaO)$ ~1·2 and 1·05, respectively; Table 1]. The more evolved melt inclusions overlap with the bulk-rock composition, which is common for rhyolites and indicates accumulation of silicic material (e.g. incorporating quartz phenocrysts and xenoliths upon eruption). In contrast, the pumice matrix glass overlaps with the less evolved melt inclusions, which is unusual (e.g. Roberge *et al.*, 2013). Concentrations of Al_2O_3, CaO, Na_2O, and K_2O in melt inclusions behave compatibly, decreasing with increasing SiO_2. Using the average melt inclusion major element compositions and the rutile saturation model of Hayden & Watson (2007), we calculate an a_{TiO2} of ~0·35, which is in agreement with the estimate we calculate using Fe–Ti-oxide oxygen-barometry (Ghiorso & Evans, 2008).

The pre-eruptive Hideaway Park rhyolite melt was volatile-rich (Fig. 7, Table 1). Although the melt inclusions have undoubtedly experienced an unquantifiable amount of post-entrapment diffusive H_2 loss (Severs *et al.*, 2007; Zajacz *et al.*, 2009), some inclusions still preserve high H_2O contents. The highest dissolved H_2O contents are found in inclusions from the lower tuff, with a maximum of 5·8 wt % H_2O and an average of 1·9 wt %. The maximum dissolved H_2O content in

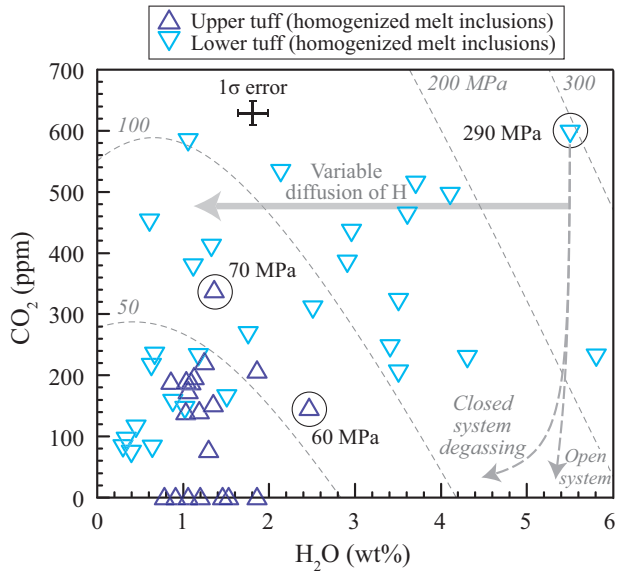

Fig. 8. Dissolved H_2O and CO_2 contents in melt inclusions. Vapor saturation isobars in the C–O–H system calculated at 750°C are from Liu *et al.* (2005), and should be used as a general reference only because the vapor saturation pressure of C–O–H–S–F–Cl-bearing melts is not yet well established. Minimum inclusion entrapment pressure estimates are given for the inclusions with the highest H_2O and CO_2 contents for both the lower and upper tuffs. Also for reference are example open- and closed-system degassing paths (Newman & Lowenstern, 2002).

inclusions from the upper tuff is 2·5 wt %, less than half that of the lower tuff, with an average of 1·3 wt %. Dissolved CO_2 concentrations are also higher in melt inclusions from the lower tuff, and range from 0 to 600 ppm. CO_2 concentrations in melt inclusions from the upper tuff range from 0 to 340 ppm. Overall, CO_2 concentrations tend to decrease with increasing melt evolution (i.e. increasing Nb; Fig. 7). Melt inclusions are also rich in F (~3300–9800 ppm) and Cl (2300–3500 ppm; Fig. 7). They contain significantly more F and Cl than melt inclusions from the Pine Grove topaz rhyolite, which average ~3600 ppm F and 620 ppm Cl (Lowenstern, 1994), and about one-half of the whole-rock F concentration of rhyolitic intrusions from the Henderson deposit (Carten *et al.*, 1988*a*). Concentrations of F and Cl in melt inclusions do not show any strong correlation with melt evolution (Fig. 7). Dissolved Li is known to diffuse rapidly in quartz-hosted melt inclusions, similar to H (e.g. Zajacz *et al.*, 2009). Melt inclusions from the Hideaway Park tuff probably underwent some diffusive loss of Li; however, many melt inclusions preserve remarkably high Li contents (Hofstra *et al.*, 2013), ranging from 1230 to 6630 ppm. Although inclusions from the upper tuff are generally more volatile-poor (e.g. H_2O and CO_2) than the lower tuff, they contain overall higher Li contents than the lower tuff (Fig. 7). Dissolved volatile and light element concentrations in the pumice matrix glass are significantly lower than in the melt inclusions (~0·8 wt % H_2O, 1300 ppm F, 360 ppm Cl, and ~68 ppm Li; Fig. 7), reflecting degassing of the melt upon ascent, eruption, and cooling of the tuff.

The high H_2O and CO_2 contents preserved in a few inclusions (apparently less affected by diffusive H_2 loss) indicate that at least some quartz crystallized at relatively high pressures (Fig. 8). We calculated a minimum entrapment pressure for the inclusion with the highest H_2O and CO_2 contents for both the lower and upper tuffs using the solubility model of Liu *et al.* (2005), which is established for C–O–H-bearing melts. This calculation assumes that the melt was volatile saturated at the time of entrapment, which is supported by the inverse correlation between CO_2 and incompatible elements (e.g. Nb, Fig. 7; Wallace *et al.*, 1999). The entrapment pressure is ~290 MPa for the lower tuff (corresponding to a depth of ~8 km, assuming a crustal density of 2·7 g cm^{-3}) and ~70 MPa for the upper tuff (~2 km depth; Table 1). The majority of the inclusions have lost significant H_2 by diffusion, as indicated by low H_2O contents with relatively high CO_2 contents (Fig. 7); we did not calculate entrapment pressures for these samples and we do not recommend interpreting a pressure for these from the isopleths in Fig. 8. A small amount of dissolved S^{2-} (<200 ppm) is known to reduce the volatile saturation pressure for C–O–H–S-bearing melts relative to that of C–O–H melts at these oxygen fugacities (Webster *et al.*, 2011). Melt inclusions from the Hideaway Park tuff have low dissolved S concentrations owing to the relatively low solubility of S in rhyolitic melt (e.g. Wallace & Edmonds, 2011). Concentrations of S are generally below the detection limit (<80 ppm), except for a few melt inclusions in the lower and upper tuffs, which contain 80–156 ppm S (Fig. 7). This small amount of S could increase the calculated entrapment pressures by ~50 MPa; however, current experimental data on this phenomenon do not allow for a rigorous pressure adjustment. The effect of F and Cl on increasing the saturation pressure of C–O–H–S-bearing melts is not well established (e.g. Webster, 1990) and should be considered when the appropriate experimental constraints are available.

Trace elements and metals

The concentrations of metals in the Hideaway Park melt inclusions are generally high compared with those of average rhyolite (e.g. Robb, 2005; Johnson *et al.*, 2013), reflecting their highly evolved nature, but are broadly similar to those of average topaz rhyolite (Table 1; see references therein). Trace element concentrations vary widely, even within single samples. Overall, inclusions are highly depleted in compatible elements (e.g. ~2 ppm Sr, ~2 ppm Ba, ~0·1 ppm Eu) and enriched in lithophile elements (e.g. ~1600–3700 ppm Li, ~16 ppm Be, ~760 ppm Rb, ~40 ppm Y, ~140 ppm Nb, ~16 ppm Cs, ~12 ppm Ta), typical of topaz rhyolites (Table 1). Niobium varies in melt concentration from 55 to 210 ppm and is inferred to behave the most incompatibly, thus we use it as an indicator of melt evolution. Concentrations of other typically incompatible elements

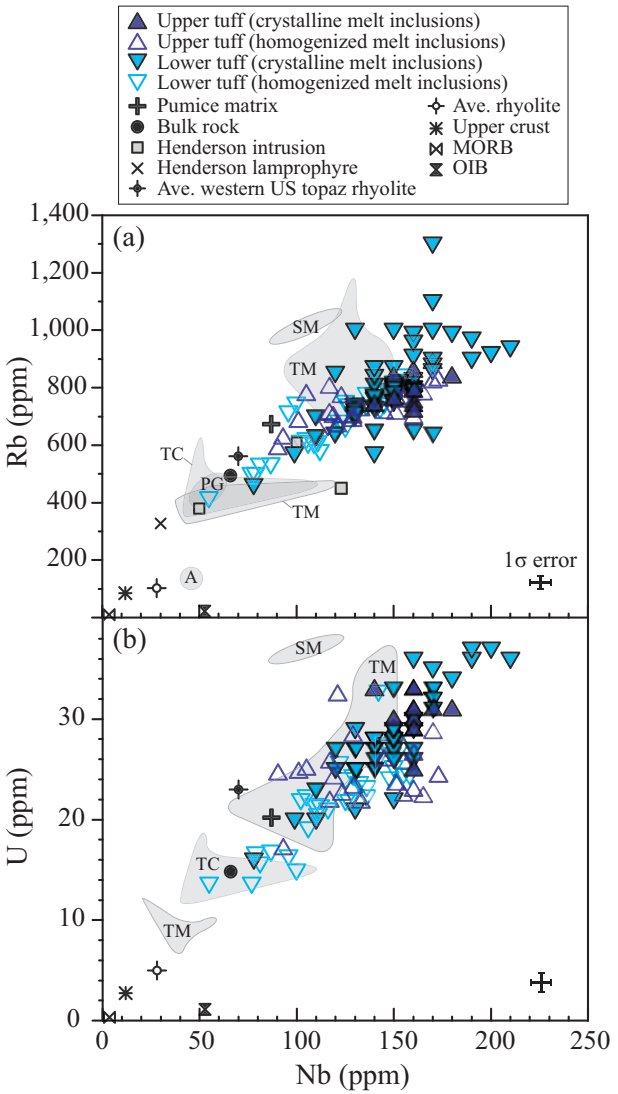

Fig. 9. Variation of (a) Rb and (b) U vs Nb in the Hideaway Park melt inclusions. Shaded fields represent analyses of silicate melt inclusions from: TC, Taylor Creek, New Mexico, topaz rhyolite (Webster & Duffield, 1991, 1994); SM, Spor Mountain, Utah, topaz rhyolite (Christiansen & Venchiarutti, 1990); and molybdenite-saturated felsic samples: PG, Pine Grove, Utah, topaz rhyolite (continuous-line outline is from Audétat *et al.*, 2011; dashed outline is from Lowenstern, 1994; we estimated the Nb value for these data assuming an incompatible Rb/Nb relationship similar to that of the Hideaway Park tuff); TM, Treasure Mountain, Colorado, topaz rhyolite (Audétat *et al.*, 2011; Lerchbaumer & Audétat, 2013); A, Amalia tuff in the Latir Volcanic Field, New Mexico, high-silica rhyolite (Audétat *et al.*, 2011). For comparison we also show average compositions for rhyolite and topaz rhyolites of the western USA (see Table 1 for references), the upper crust (Rudnick & Gao, 2003), MORB and ocean island basalt (OIB) (Sun & McDonough, 1989).

(e.g. Ga, As, Rb, Y, Sn, Sb, Cs, Gd, Dy, Er, Yb, Ta, W, Tl, Bi, Th, U) increase with increasing Nb (Fig. 9). As with major elements, the trace element composition of the pumice matrix glass is more primitive than, or compositionally distinct from, most of the melt inclusions (Fig. 9). REE patterns of melt inclusions mimic those of the whole-rock and intrusions from Henderson (Fig. 3b), but extend to higher light REE (LREE) and heavy REE (HREE) values and lower Eu values.

Melt inclusion entrapment temperatures calculated using the Zr-saturation thermometer of Watson & Harrison (1983) range from 663 to 778°C and average ~745°C (Table 1; Electronic Supplement 1). These estimates agree well with the two-feldspar, Fe–Ti-oxide, and biotite thermometry results (Table 2), but average ~95°C lower than temperatures estimated from Ti in quartz. This discrepancy suggests that Ti-in-quartz temperature estimates are too high owing to an inaccurate a_{TiO2} estimate that is ~0·5 too low. We therefore do not discuss Ti-in-quartz temperature estimates further.

Incompatible element signatures of the melt inclusions show an affinity to within-plate granites (Fig. 10; Pearce *et al.*, 1984), similar to other molybdenite-saturated felsic magmas (Audétat *et al.*, 2011) and topaz rhyolites from the western USA (Christiansen *et al.*, 1986). This geochemical interpretation agrees well with the post-subduction, continental rift-related setting inferred for the generation of high-grade Climax-type porphyry Mo deposits (e.g. Carten *et al.*, 1993).

Metals of particular interest in the context of mineralization at the Henderson porphyry Mo deposit are higher in melt inclusions than in average topaz rhyolite (Fig. 11; ~7–24 ppm Mo, ~21–52 ppm Pb, <0·1–29 ppm Cu, ~40–760 ppb Ag, ~4–14 ppm W, ~28–2700 ppm Zn, ~0·3–1·8 ppm Bi, ~690–1400 ppm Mn). Mo and W both behave incompatibly in the melt inclusions, as do Bi and Mn. Concentrations of Pb and Zn are scattered with increasing melt evolution, although the highest concentrations tend to be in the most evolved (i.e. highest Nb) melts. The Pb and Zn contents are probably controlled by variable crystallization of minerals in which these elements are compatible, such as sanidine ($K_{DPb}^{san/melt} \sim 1{\cdot}4$; Ewart & Griffin, 1994) and accessory biotite ($K_{DPb}^{bi/melt} \sim 2{\cdot}1$; $K_{DZn}^{bi/melt} \sim 32$; Ewart & Griffin, 1994), magnetite ($K_{DZn}^{mag/melt} \sim 59$; Ewart & Griffin, 1994), ilmenite ($K_{DZn}^{ilm/melt} \sim 8{\cdot}3$; Ewart & Griffin, 1994), and zircon ($K_{DPb}^{zrn/melt} \sim 7{\cdot}5$; Bea *et al.*, 1994). Concentrations of Cu scatter with melt evolution (Fig. 11), which could be the result of crystallization of accessory biotite (Johnson *et al.*, 2013; $K_{DCu}^{bi/melt} \sim 20{\cdot}3$; Ewart & Griffin, 1994), magnetite ($K_{DCu}^{mag/melt} \sim 5{\cdot}3$; Ewart & Griffin, 1994), and ilmenite ($K_{DCu}^{ilm/melt} \sim 3{\cdot}3$; Ewart & Griffin, 1994) or the saturation and resorption of accessory pyrrhotite ($K_{DCu}^{po/melt} \geq 200$; Simon *et al.*, 2008). Alternatively (but probably not exclusively), diffusion of Cu out of the melt inclusions could explain the scatter (Kamenetsky & Danyushevsky, 2005; Zajacz *et al.*, 2009); however, given the overall high concentrations of Cu and the fact that analyses of both crystalline and homogenized melt inclusions scatter over a similarly broad range, diffusion is probably a secondary factor. Concentrations of Ag are also scattered (Fig. 11), which could be the effect of accessory pyrrhotite crystallization and resorption ($K_{DAg}^{po/melt} \geq 58$; Simon *et al.*, 2008); however, homogenized inclusions have overall lower concentrations, suggesting that diffusion out of the

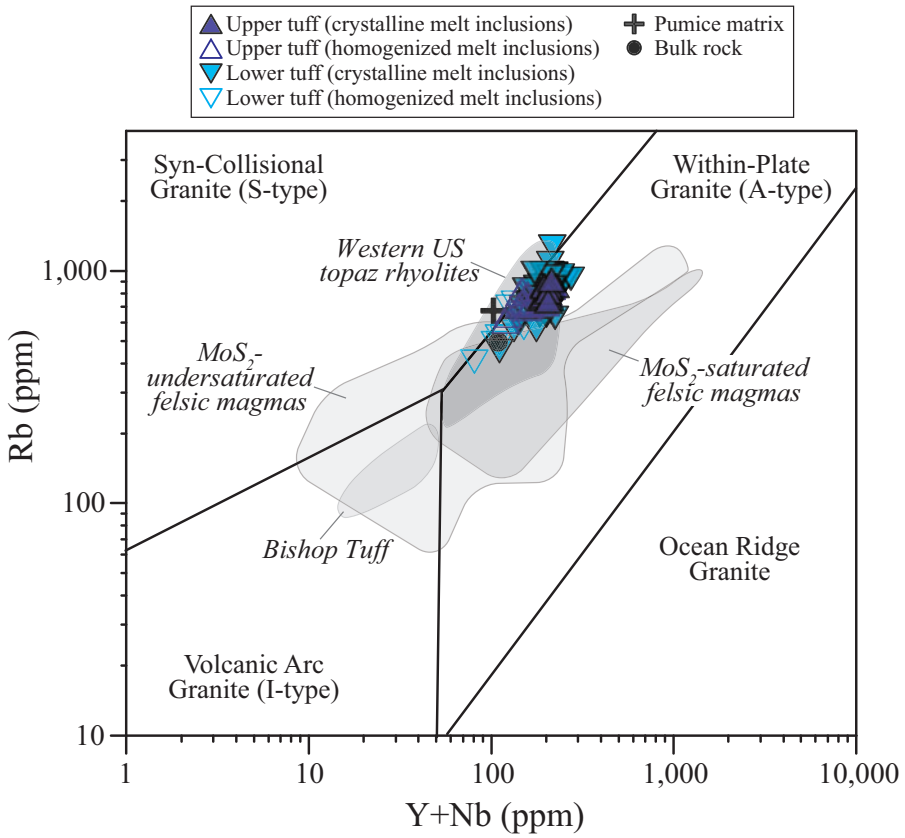

Fig. 10. Geochemical interpretation of the Hideaway Park rhyolite according to the tectonic discrimination diagram of Pearce *et al.* (1984). For comparison, shaded fields show MoS_2-saturated and -undersaturated felsic melt inclusions from around the world (Audétat *et al.*, 2011), and bulk-rock data from topaz rhyolites of the western USA (Christiansen *et al.*, 1986) and the Bishop tuff rhyolite (Hildreth, 1977). The 1σ errors are reported in Table 1.

inclusions (e.g. Zajacz *et al.*, 2009) during homogenization experiments was relatively efficient. Regardless of the uncertainty about the role of diffusion, we present Cu and Ag data as they provide minimum estimates for the concentrations of these metals in topaz rhyolite melts.

With the exception of Pb and Cu, metal concentrations in the pumice matrix glass (Zn, Bi, Ag, Mn) are generally lower than expected given the relatively primitive Nb contents (Fig. 11). For example, given the approximate Mo/Nb slope defined by the melt inclusions, a melt with 87 ppm Nb should contain ~12 ppm Mo rather than 4 ppm. On the other hand, the Cu concentration in the pumice matrix glass is higher than expected. Both of these trends are not consistent with the observation that the concentrations of many incompatible elements, such as Rb and U (Fig. 9; also Ga, As, Sb, La, Ce, Tl), in the pumice matrix glass have the appropriate element/Nb ratio predicted for a less evolved melt. We consider the implications of this relationship in the context of previous work on rhyolites below.

Few melt inclusion metal analyses exist for other studied topaz rhyolites, but they are useful to evaluate some key elements. The maximum Mo concentrations in the Hideaway Park melt inclusions are greater than those from several molybdenite-saturated rhyolites that are genetically related to porphyry Mo mineralization, including the Pine Grove tuff (Pine Grove district, UT; Lowenstern *et al.*, 1994; Audétat *et al.*, 2011) and Amalia tuff (Questa district, NM; Audétat *et al.*, 2011). They are similar to maximum Mo concentrations in melt inclusions from the Sn-mineralized Taylor Creek (NM) topaz rhyolite (Webster & Duffield, 1991, 1994), and are exceeded only by those from the Treasure Mountain dome (Climax–Alma districts, CO; Lerchbaumer & Audétat, 2013). Audétat *et al.* (2011) reported Mo concentrations in melt inclusions from molybdenite-saturated (~1–13 ppm Mo; typically rift-related rhyolites) and molybdenite-undersaturated (~1–17 ppm Mo; typically volcanic arc and syn-collisional rhyolites) samples from 27 felsic magma systems worldwide, and none attain the maximum Mo concentrations recorded in the Hideaway Park melt inclusions (~20–24 ppm Mo; Fig. 12). Concentrations of W and Pb in melt inclusions are similar to those of other molybdenite-saturated rhyolites but Zn and Cu extend to considerably higher concentrations (Fig. 11).

DISCUSSION

The melt inclusions documented in this study provide snapshots of the evolving Hideaway Park magma. Combined with the pumice matrix glass composition

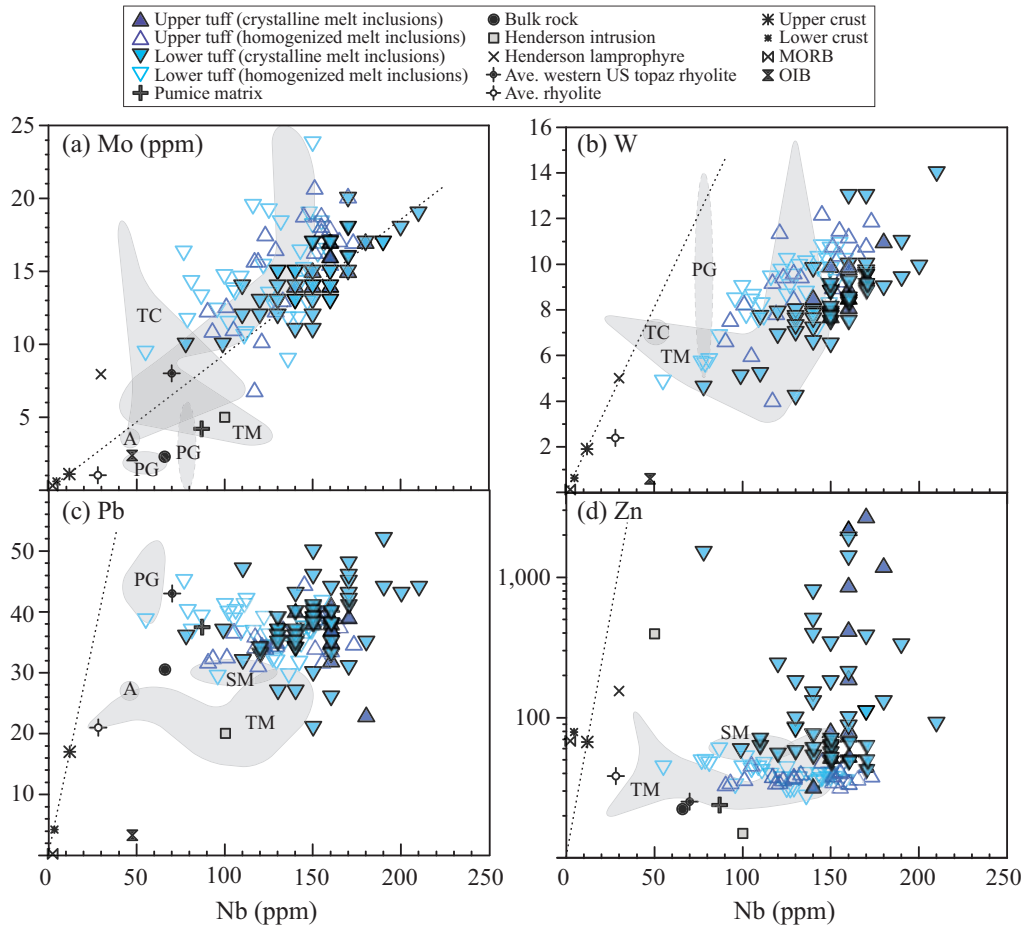

Fig. 11. Variation of (a) Mo, (b) W, (c) Pb, (d) Zn, (e) Cu, (f) Bi, (g) Ag, and (h) Mn concentrations for melt inclusions from the Hideaway Park rhyolite versus Nb. Molydenum is the only metal of economic importance at the Henderson deposit, but the rest are of interest because they are geochemically anomalous at Henderson (Seedorff & Einaudi, 2004*b*). Dotted lines represent the average upper-continental crustal metal/Nb ratio. Shaded fields and abbreviations are the same as in Fig. 9; the average composition for the lower crust is from Rudnick & Gao (2003). The 1σ errors for Mo, W, Pb, Bi, Ag, and Mn are equal to or smaller than the symbols. All errors are reported in Table 1.

and phenocryst chemistry we can reconstruct some of the physical conditions of magmatic evolution and explore the behavior of metals during magma crystallization, mixing, ascent, degassing, and eruption.

Physical processes of magmatic evolution

The high concentration of H_2O and CO_2 preserved in some melt inclusions from the lower tuff (>5 wt % H_2O, 500–600 ppm CO_2) demonstrates that the magma that produced the lower tuff began crystallizing quartz in a reservoir at upper crustal levels at a minimum depth of ~8 km (~290 MPa; Fig. 8). Owing to post-entrapment diffusion of H_2 out of the melt inclusions, we cannot interpret a degassing path with these data. However, CO_2 is not expected to diffuse out of the melt inclusions and there are no bubbles in the homogenized inclusions that could contain CO_2 (e.g. Steele-MacInnis *et al.*, 2011). Given these considerations and the fact that the solubility of CO_2 in rhyolitic melts is highly pressure dependent (Wallace & Anderson, 1999), the low CO_2 values (<100–200 ppm) preserved in most melt inclusions from the lower tuff suggest that the magma ascended, degassing a CO_2-enriched fluid, and continued crystallizing and evolving at shallower crustal levels. The negative correlation of CO_2 with increasing Nb for the lower tuff (Fig. 7) also provides evidence of CO_2-bearing fluid degassing with progressive melt evolution and crystallization. Based on the maximum H_2O and CO_2 contents preserved in melt inclusions from the upper tuff (~2·5 wt % H_2O, ~130 ppm CO_2), a shallow reservoir at ~70 MPa (~2 km minimum depth) is probably where the magma that produced the upper tuff largely evolved. This depth is similar to the reconstructed depth of mineralized intrusions in the Red Mountain intrusive complex (~1·6 km for the Urad deposit and 2·8–3·1 km for the Henderson deposit; Carten *et al.*, 1988*a*).

As magma ascends through the crust and degasses, it evolves by competing processes such as crystallization and magma mixing. Magma evolution is best monitored by elements that are highly incompatible in crystallizing phenocrysts and any exsolved volatile phase, such that their concentrations in the silicate melt increase with progressive crystallization and fluid

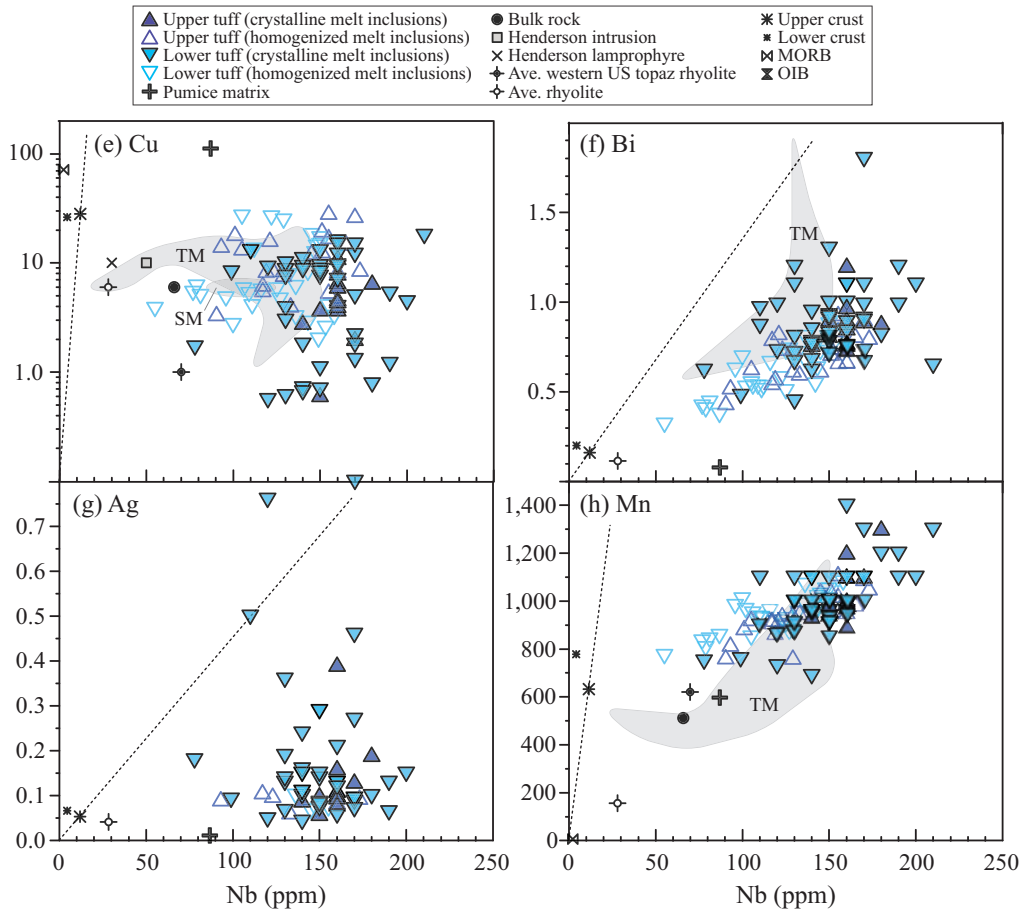

Fig. 11. Continued.

exsolution. To facilitate comparisons with previous work by Audétat *et al.* (2011), we use Rb (similar incompatibility to Nb) and Mo (a largely incompatible metal of interest over the melt inclusion entrapment interval—we discuss exceptions to this behavior below) to investigate the role of magma crystallization and magma mixing in the generation of the Hideaway Park magma as documented by melt inclusion compositions.

Magma crystallization and evidence for filter pressing, crystal settling, and magma mixing

The Mo contents in melt inclusions broadly increase with increasing Rb, and show the same pattern from core to rim for inclusions trapped within single quartz phenocrysts (Fig. 13). These observations are expected if the highly evolved melts preserved in Hideaway Park quartz phenocrysts were produced by crystallization of a relatively less evolved rhyolitic melt (e.g. inclusion HPR-11B, which contains 414 ppm Rb and 9·5 ppm Mo), as has been suggested by Christiansen *et al.* (1984). Magma crystallization can be modeled by either equilibrium or fractional crystallization. The difference between the two models is that during fractional crystallization, crystals are removed from the melt (i.e. by crystal settling or flotation) or the melt is removed from the crystals (i.e. by filter pressing), and therefore incompatible trace element concentrations will increase in the melt more quickly for a given increment of crystallization. Consequently, it takes slightly less crystallization to produce the range of trace element concentrations observed in the melt inclusions. In our fractional crystallization model (Fig. 12), we used the Rayleigh fractional crystallization equation

$$C_i^{\text{melt}} = C_o^{\text{melt}} * F^{(D-1)}$$

where C_o^{melt} is the initial concentration of element i in the parent melt, C_i^{melt} is the concentration of element i in the melt after crystallization, F is the proportion of melt remaining after crystallization, and D is the bulk distribution coefficient that describes the distribution of trace elements between the crystalline assemblage and the melt. We used the least-evolved melt inclusion from the lower tuff as the parent melt for both the lower and upper tuff models because the least-evolved melts for each sample are very similar in composition. Using the same mineral modes as observed in the tuff and mineral–melt distribution coefficients (Table 3), both equilibrium and fractional crystallization models produce very similar results for small values of F. Melt inclusions from the lower Hideaway Park tuff show a broader

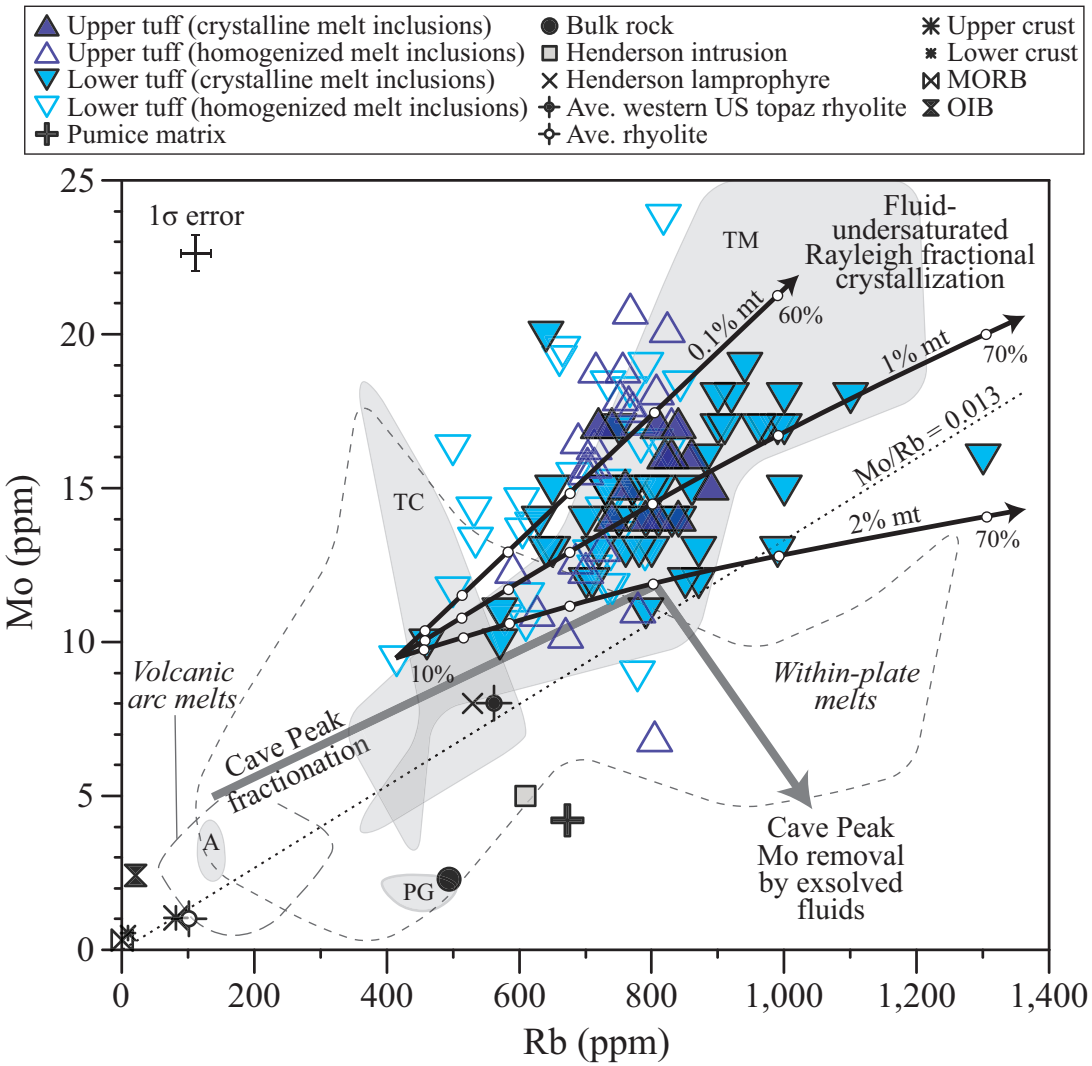

Fig. 12. Concentrations of Mo and Rb in melt inclusions, pumice matrix, and bulk-rock from the Hideaway Park rhyolite, along with bulk-rock compositions of the Henderson stock intrusion and kersantite lamprophyre dike from the Henderson porphyry Mo deposit. Shaded fields and abbreviations are the same as in Fig. 9. Dashed fields show the compositions of felsic melt inclusions from around the world in both within-plate and volcanic arc settings, including MoS_2-saturated and -undersaturated systems (Audétat *et al.*, 2011). Gray arrow shows melt evolution trend from Cave Peak, TX (Audétat, 2010). Black arrows denote modeled evolutionary trends of melts during Rayleigh fractional crystallization, starting with the same parent melt composition for both the upper and lower tuffs. The white dots indicate the amount of crystallization in increments of 10%. The modal proportion of magnetite (% mt) crystallizing largely controls the Mo/Rb ratio of the resultant melt.

range in trace element concentrations than those from the upper tuff, which can largely be explained by ~60–70% fractional crystallization. The more restricted trace element range in the upper Hideaway Park tuff requires only ~45–55% fractional crystallization. Because of the high mineral–melt distribution coefficient of Mo in magnetite (Table 3), the mode of accessory magnetite dominates the overall bulk distribution coefficient, and the broad spread in Mo contents at any given Rb concentration can be explained by slight differences in the volume per cent of accessory magnetite crystallization, from 0·1 to 2 vol. % (Fig. 12). It is important to note, however, that melts with higher Mo contents than those modeled with 0·1 vol. % magnetite require a parental melt with a slightly higher initial Mo content than that modeled here. Given that the overall crystallinity of the Hideaway Park tuff is only ~20–30 vol. %, the high degrees of crystallization suggested by the modeling require that crystals separate fairly efficiently from the evolving melt, which implies that filter pressing and/or crystal settling is very important in the generation of these highly evolved melts, as has been noted for other highly evolved, relatively crystal-poor silicate melts (Johnson et al., 1989; Sisson & Bacon, 1999; Bachmann & Bergantz, 2004). Because the calculated density of the melt (~2·3 g cm^{-3}) is only slightly less than that of quartz and feldspar (~2·5–2·6 g cm^{-3}), it is likely that filter pressing may be the dominant mechanism for separating melt from crystals. Christiansen et al. (1984) found that similar degrees of crystal fractionation (~40–60%) from a less evolved rhyolite melt could explain the extreme compositions observed in other topaz

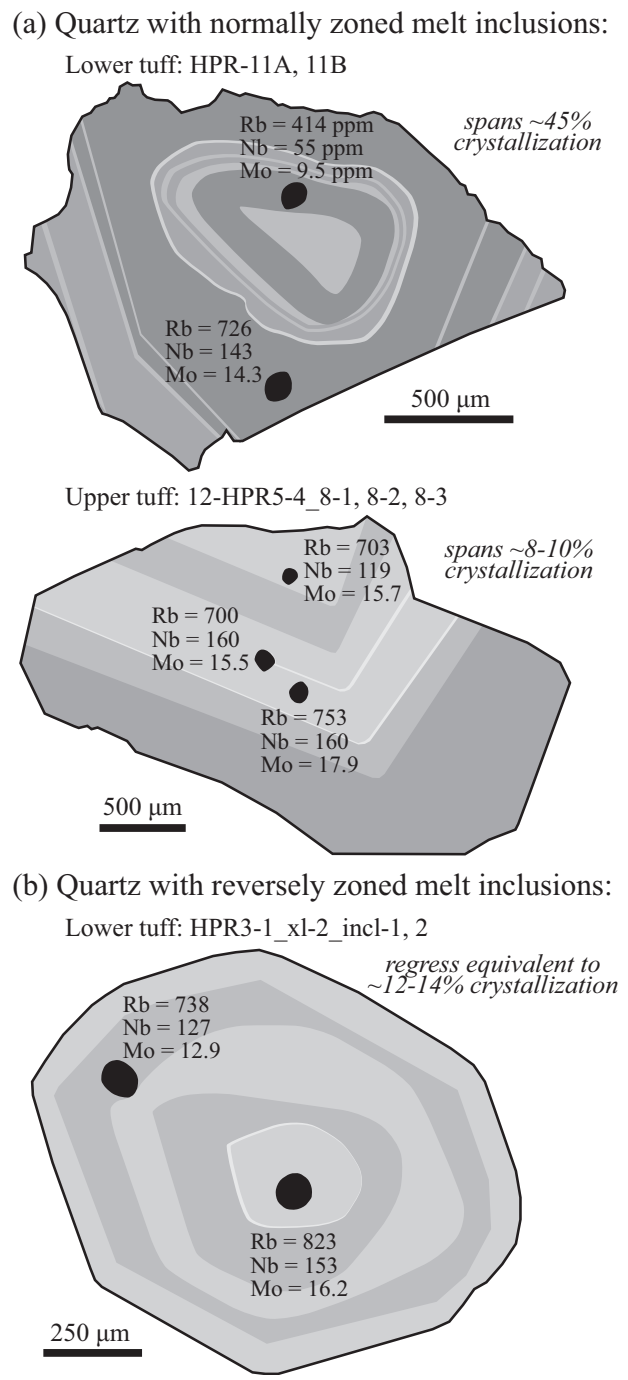

Fig. 13. Schematic diagram of quartz phenocrysts that trapped multiple melt inclusions. Growth and resorption patterns evident in SEM-CL images are shown to demonstrate the (a) normally and (b) reversely zoned trapping of melt inclusions. Melt inclusion compositions are given in ppm and the range of melt evolution preserved within each crystal is reported in per cent crystallization based on Rayleigh fractional crystallization model results.

rhyolites from the western USA. They also suggested that the high fluorine (F) contents of these magmas may be conducive to such magmatic processes. Among their observations is that F depresses the solidus of topaz rhyolite melt to a greater degree than the liquidus (Wyllie, 1979; Weidner & Martin, 1987), effectively

Table 3: Mineral/melt distribution coefficients (K_D), mineral modes, and bulk D value used in Rayleigh fractional crystallization models

Mineral	Mode (vol. %)	$K_D^{mineral/melt}$ Rb	Mo
Quartz	7·0	n.a.	n.a.
Sanidine	7·0	0·38	0·20
Albite	7·0	0·13	0·20
Biotite	2·0	5·97	2·29
Ilmenite	0·5	n.a.	11·00
Magnetite	0·1–2·0	0·04	29·00
Zircon	0·5	n.a.	n.a.
Bulk *D*		0·05	0·12–0·15

Mineral modes are approximated from thin sections documented in this study, and adjusted slightly to fit the range of modeled data. Mineral–melt distribution coefficients (K_D) for high-silica rhyolites are compiled from Mahood & Hildreth (1983), Stix & Gorton (1990), Bea *et al.* (1994), Ewart & Griffin (1994) and Streck & Grunder (1997). n.a., not applicable.

increasing the temperature window (and time for a given cooling rate) over which magma can undergo fractional crystallization. As long as F remains incompatible in the fractionating mineral assemblage, accumulation of F in the melt enhances this effect. Fluorine has also been shown to increase the diffusivity of elements in silicate melts (Bailey, 1977), enhancing the potential for crystal nucleation and growth. In addition, high H_2O and F contents in silicate melts have an equally large effect on melt viscosity (Bailey, 1977; Baker & Vaillancourt, 1995; Giordano et al., 2004). But unlike H_2O, F has a much higher solubility in rhyolitic melts at low confining pressure, such that as an F-rich magma exsolves H_2O upon ascent, retention of F maintains a relatively low melt viscosity. Using the model of Giordano et al. (2004), we estimated the minimum and maximum melt viscosity based on the Hideaway Park melt inclusions with the highest and lowest combined $H_2O + F$ mol %. The calculated viscosity for a high-silica rhyolite melt that is H_2O- and F-rich (5·8 wt % H_2O, 9500 ppm F, 750°C; Fig. 6) is $\sim 10^{4.9}$ Pa s, comparable with that of basaltic andesites to dacites (at typical magma reservoir temperatures; Takeuchi, 2011). In contrast, that for a dry, F-rich melt (~0·5 wt % H_2O, 8400 ppm F, 750°C; Fig. 7) is $\sim 10^{9.8}$ Pa s, which is analogous to the viscosity of dacites to hydrous rhyolites (at typical magma reservoir temperatures; Takeuchi, 2011).

In simple magmatic systems that evolve dominantly by crystallization, the pumice matrix glass should be the most evolved melt (i.e. more evolved than all melt inclusions) because it represents the last portion of untrapped melt upon eruption (e.g. Roberge *et al.*, 2013). However, in the Hideaway Park tuff, the pumice matrix glass is characteristically less evolved than the majority of the melt inclusions (as recorded by incompatible, fluid-immobile elements: e.g. Fig. 9; 87 ppm Nb, 673 ppm Rb, 20 ppm U; also Figs 11 and 12, Table 1). This observation requires magma recharge and mixing with a less differentiated rhyolitic melt prior to eruption, and/or differential motion between crystals and melt (e.g. filter pressing, crystal settling, or convective

mixing of crystals into less evolved magma). Such a magma recharge event may have been responsible for triggering the eruption of the Hideaway Park magma.

Further evidence for magma recharge and mixing comes from evaluation of the SEM-CL images of four quartz phenocrysts that contain multiple melt inclusions trapped within distinct growth bands (Fig. 13). Three out of the four phenocrysts trapped inclusions that are normally zoned; that is, the quartz chronologically trapped progressively more evolved melts (Fig. 13a). We can track the range of evolution preserved within a single crystal in terms of per cent fractional crystallization based on the model in Fig. 12. For example, the phenocryst with the broadest evolutionary range observed has a melt inclusion near the core with 414 ppm Rb and 9·5 ppm Mo and an inclusion near the rim with 726 ppm Rb and 14·3 ppm Mo. This trace element range corresponds to ~45% crystallization, whereas another quartz phenocryst (Fig. 13a) trapped three melt inclusions that span only ~8–10% crystallization. Conversely, one quartz phenocryst trapped reversely zoned inclusions (Fig. 13b), which requires a regression of magma evolution equivalent to melting of ~12–14% previously crystallized minerals, either by crystal resorption or by recharge with less evolved rhyolitic melt.

Given these observations and the volatile-rich nature of the Hideaway Park magma, it seems likely that some combination of filter pressing, crystal settling, magma recharge, magma mixing, and volatile exsolution contributed to the wide range in trace elements preserved in melt inclusions. High concentrations of higher solubility volatiles such as Cl or F (Fig. 7) implies that little to no quartz crystallization (and inclusion entrapment) occurred upon shallow ascent and eruption. The formation of this Mo-bearing topaz rhyolite is thus the result of dynamic mixing of more than one batch of rhyolite melt within the shallow crust that probably had similar parental magmas at depth.

Source of molybdenum and anomalous metals at Henderson

The source of Mo in high-grade mineralizing magmatic systems remains debatable. Significant input from lower crustal sources has been commonly inferred (e.g. Farmer & DePaolo, 1984; Lüders *et al.*, 2009) based on Pb, Sr, and Nd isotopic compositions. For example, the Sr and Nd isotopic compositions of the Seriate stock ($\varepsilon_{Nd} = -10$, $\varepsilon_{Sr} = 432$) indicate involvement of old crustal sources; however, contamination of the Seriate stock magma by the Silver Plume granite is constrained to <1% (Stein & Crock, 1990), suggesting a deeper crustal source. The Pb isotopic compositions of successive Henderson stocks are nearly identical ($^{206}Pb/^{204}Pb \sim 17{\cdot}699$, $^{207}Pb/^{204}Pb \sim 15{\cdot}518$, $^{208}Pb/^{204}Pb \sim 39{\cdot}490$) and are distinct from those of the Silver Plume granite, limiting local Pb derivation to <7% and supporting a homogenized Pb source deeper within the crust (Stein & Hannah, 1985). Stein & Crock (1990) suggested a moderately felsic, granulitic lower crust as a potential source to explain the Sr, Nd, and Pb isotopes. More recent work by Pettke *et al.* (2010) has proposed that retarded uranogenic Pb isotope signatures typical of major Mo deposits in the western USA, including Henderson, imply source magmas that originated from metasomatized subcontinental lithospheric mantle, with assimilation of lower crustal lithologies (as indicated by more radiogenic $^{208}Pb/^{204}Pb$ and less retarded $^{206}Pb/^{204}Pb$) operating as a secondary consequence of long-lived magmatic systems, rather than as the principal magma source.

Audétat *et al.* (2011) suggested that if Mo is sourced from mid- to upper-continental crust, then melt inclusions should be expected to have Mo/Rb ratios $\leq 0{\cdot}013$–$0{\cdot}009$ (average mid- to upper-continental crustal ratios; Rudnick & Gao, 2003) because Rb is highly incompatible during crystallization or partial melting, and therefore Mo/Rb ratios can only decrease through these magmatic processes. Nearly all of the Hideaway Park melt inclusions have Mo/Rb ratios much greater than mid- to upper-crustal values (up to Mo/Rb = 0·033; Fig. 12). The high ratios suggest a deeper source of Mo such as the lower continental crust (Mo/Rb = 0·055; Rudnick & Gao, 2003) or metasomatized mantle melts (e.g. ocean island basalts, Mo/Rb = 0·077; Sun & McDonough, 1989).

Using similar logic, we can assess the potential source of other metals that are found in sub-economic but anomalous concentrations at the Henderson porphyry Mo deposit (Fig. 11). Nb behaves more incompatibly than W, Pb, Zn, Cu, Bi, Ag, and Mn during crystallization or partial melting (except in extremely evolved melts if Nb-rich ilmenite or Nb oxides crystallize), and therefore the metal/Nb ratio is expected to decrease during crystallization or partial melting. For reference, dotted lines in Fig. 11 represent the average upper-continental crustal metal/Nb ratio. Interestingly, when Mo versus Nb is considered, melts of metasomatized mantle (e.g. ocean island basalts) have too low a Mo/Nb ratio to be a potential Mo source, but lower crust is still a viable source. Metasomatized mantle is not a probable source for W or Pb, but either lower- or upper-continental crust is suitable. Elements such as Zn, Cu, Bi, Ag, and Mn may all be reasonably sourced from the lower- or upper-continental crust (Fig. 11). The melt inclusion data suggest that different metals may be sourced from a variety of locations along the path of an ascending magma from the mantle to the upper crust during the generation of mineralizing topaz rhyolites.

Saturation of molybdenite

Out of more than 100 quartz phenocrysts examined, we identified one quartz phenocryst from the lower tuff that contains a small (~20 μm) platelet of molybdenite. Thus, the Hideaway Park magma was molybdenite-saturated, at least for a brief time during its evolution. The measured Mo concentrations in the Hideaway Park melt inclusions presumably top out at ~24 ppm owing to saturation of MoS_2. This maximum Mo concentration is higher than that found in melt inclusions from many

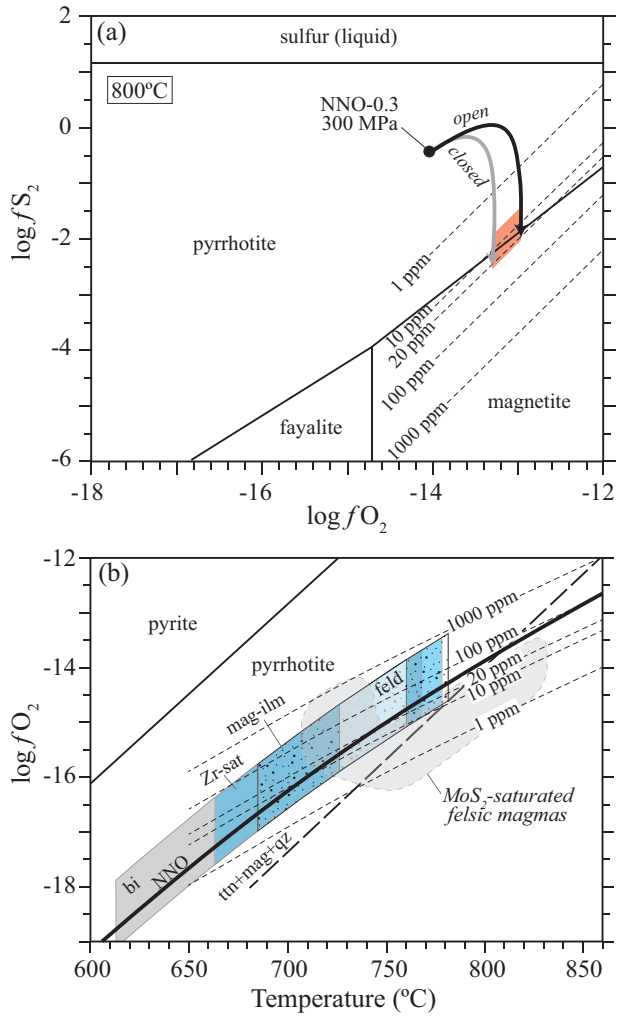

Fig. 14. Thermodynamically predicted MoS_2 solubilities (dashed lines, ppm Mo) as a function of fO_2, fS_2, and temperature, modified after Audétat *et al.* (2011). (a) fO_2 vs fS_2 at isothermal conditions (800°C), with arrows showing the modeled path of the Hideaway Park rhyolite upon ascent from 300 to ~50 MPa (black, open system; gray, closed system). Red shaded area represents range of Mo contents observed in melt inclusions. (b) Temperature and fO_2 estimates for the Hideaway Park rhyolite. Shaded boxes show the range of fO_2 based on decompression modeling and temperatures constrained by various mineral thermo-oxygen barometers [biotite (gray shaded box); magnetite–ilmenite (black stippled box), and two-feldspars (white box); Table 2, Electronic Supplement 3] and Zr-saturation thermometry (blue shaded box; Table 1, Electronic Supplement 1). Dashed-outline, gray shaded field shows conditions of MoS_2-saturated felsic melts from Audétat *et al.* (2011) and long-dashed black line shows stability of titanite (ttn) + magnetite (mag) + quartz (qz) assemblage from Wones (1989).

other Mo mineralized systems from around the world (Fig. 12) and is notable given that highly evolved silicate melts rarely contain >20 ppm Mo (e.g. Audétat *et al.*, 2011).

To understand the remarkably high MoS_2 solubility of the Hideaway Park magma, we consider our estimates of fO_2, fS_2, and temperature in light of the molybdenite solubility model of Audétat *et al.* (2011). Their thermodynamic model applies to silicic magma systems that are at or very near pyrrhotite saturation. Evolved rhyolites commonly contain pyrrhotite over a broad range of common fO_2 and fS_2 conditions (Audétat *et al.*, 2011); however, preservation of pyrrhotite is typically poor owing to magma oxidation and exsolution of a S-bearing volatile phase during ascent and degassing (e.g. Stavast *et al.*, 2006; Audétat & Simon, 2012). Thermodynamic modeling of the fO_2 and fS_2 during ascent and degassing of the Hideaway Park magma from 300 to ~50 MPa (using the program D-Compress; Burgisser *et al.*, in preparation) suggests that it was at or very close to pyrrhotite saturation (Fig. 14a; decompression paths shown with arrows: black indicates open system; gray indicates closed system). We do not observe pyrrhotite in any of the phenocrysts or thin sections studied, but cryptic evidence of pyrrhotite may be preserved. For example, some biotite phenocrysts contain slightly Fe-enriched cores with distinct, thin, Fe-rich rims (Fig. 2d), which could record progressive co-crystallization with pyrrhotite followed by abrupt pyrrhotite dissolution (e.g. Scaillet & Pichavant, 2005). On the other hand, this zonation could also be the product of magma mixing with a less evolved magma. In addition, we identified one small (<10 μm) quartz-hosted inclusion of pyrite from the lower tuff, which could be the product of pyrrhotite oxidation (Stavast *et al.*, 2006).

Assuming the Hideaway Park magma was at or close to pyrrhotite saturation as it decompressed and degassed (e.g. ~800°C, $fO_2 \sim$ NNO − 0·3 to NNO + 0·9, log $fS_2 \sim 0$ to −2·5), the model of Audétat *et al.* (2011) yields reasonable MoS_2 solubilities in good agreement with the measured Mo concentrations in the melt inclusions (Fig. 14a; red shaded area). If we consider the scenario where the Hideaway Park magma was saturated in the assemblage magnetite + quartz ± pyrrhotite at a constant fS_2, and a range of fO_2 from NNO − 0·3 to NNO + 0·9, the Hideaway Park magma could have saturated at ~24 ppm between ~630 and 780°C (Fig. 14b). This temperature range is broad, but not unreasonable given the evidence for magma mixing in this system. The high end of this range is remarkably hot considering the volatile-rich character of the magma, but is not outside reasonable experimental phase relations for topaz rhyolites (Webster *et al.*, 1987), and could be sustained by input of mafic components including S, which we discuss in more detail below. Given these observations, the high MoS_2 solubility of the Hideaway Park magma may be a product of just the right temperature and fO_2 combination.

Evolution of metals during magma crystallization and degassing

Evolution of the Hideaway Park magma, recorded by phenocrysts and melt inclusions, proceeded largely by fractional crystallization of multiple batches of topaz rhyolite accompanied by significant degassing as they ascended from a crustal reservoir at ~8 km to shallow crustal levels prior to eruption (e.g. Figs 8 and 12).

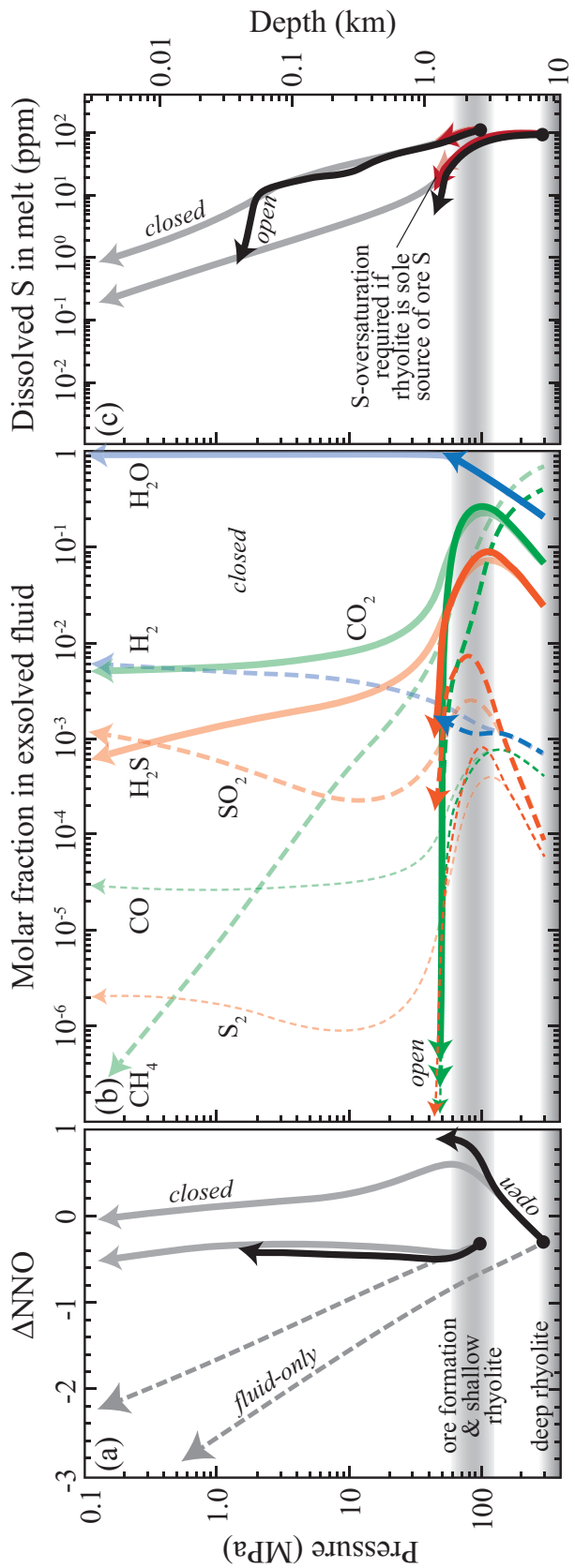

Fig. 15. Compositional and oxygen fugacity variations in S–O–H–C-bearing rhyolitic melt and exsolved fluids during magma ascent modeled using the program D-Compress (Burgisser *et al.*, in preparation). Model assumes a hot (800°C), volatile-rich (~4 wt % H_2O, ~350 ppm CO_2, ~90 ppm S) rhyolite melt that is relatively S-rich (C/S ~2·8) and Fe-poor (0·5 wt % FeO*) with an initial fO_2 of NNO – 0·3 and 0·1 wt % initial exsolved fluid, similar to the Hideaway Park rhyolite. (a) Redox variations for three model scenarios: (1) magma ascent from a relatively deep storage area (300 MPa;~8 km; black arrows, open system; gray arrows, closed system), (2) magma ascent from a shallow storage area, which also coincides with the depth of mineralization at Henderson (100 MPa; ~2–3 km; black arrows, open system; gray arrows, closed system); (3) magma intrusion at either of these crustal levels and decompression of the exsolved fluids, and a fluid ascending from a stalled intrusion of rhyolite (dashed arrows). (b) Compositional variations of fluid species exsolving from a rhyolite decompressing from 300 MPa to the surface (dark arrows, open system; pale arrows, closed system). It should be noted that open-system models do not reach the surface because the C-species are exhausted at depth. (c) Evolution of S dissolved in rhyolite ascending from 300 and 100 MPa (black arrows, open system; gray arrows, closed system). Red arrows denote the S-oversaturation required if rhyolite is the sole source of ore sulfur.

Open-system magma degassing at shallow crustal levels (~100 MPa) is evident from negative δD isotope shifts (to –140‰) in biotite from the Henderson deposit (Carten *et al.*, 1988*b*). Thermodynamic modeling of a S–O–H–C-bearing rhyolitic melt decompressing through the crust to the surface [Fig. 15; using the program D-Compress of Burgisser *et al.* (in preparation)] provides a framework with which to evaluate the behavior of degassing volatiles during ascent and eruption of the Hideaway Park magma, as well as analogous batches of magma that may not have vented to the surface. We start the model with a hot, volatile-rich rhyolitic magma (800°C, ~4 wt % H_2O, ~350 ppm CO_2, ~90 ppm S) at an initial fO_2 of NNO – 0·3, and we explore three scenarios: (1) magma ascent to the surface from a relatively deep storage area (300 MPa; ~8 km; open and closed system); (2) magma ascent to the surface from a shallow storage area, which also coincides with the depth of mineralization at Henderson (100 MPa; ~2–3 km; open and closed system); (3) magma intrusion at either of these crustal levels and ascent of exsolved magmatic fluids to the surface (i.e. during isobaric crystallization). The presence of sulfur-bearing mineral phases is not taken into account, so model outputs represent an end-member case where S partitions from the melt to the immiscible fluid phase only during magma ascent. We then use the model geochemical trends and experimental metal partitioning data to arrive at a first-order understanding of how volatiles and metals might accumulate following this magma ascent path before eruption or accumulation in a porphyry deposit environment.

Upon magma decompression, the oxidation state of the melt changes as aqueous fluids exsolve (Fig. 15a). From the deep magma reservoir, during closed-system magma decompression (magma remains in contact with the fluid), the melt gradually oxidizes to ~NNO + 0·6 as it rises to a depth equivalent to <100 MPa, largely in response to loss of H_2 into the immiscible fluid (Fig. 15b). If the system remains closed, further ascent leads to reduction of the magma to ~NNO – 0·1 at the surface. In contrast, if the system is

open to volatile loss [magma and immiscible fluid separate (e.g. by ascent of a buoyant volatile phase) during ascent at pressures <100 MPa], which is probably the case upon reaching the brittle–ductile transition beneath a volcanic edifice (i.e. the porphyry environment; Fournier, 1999), the magma oxidizes even further to ~NNO + 0·9. Oxidation of the magma can lead to resorption of sulfides (Stavast *et al.*, 2006), which may very well have transpired for pyrrhotite and possibly molybdenite in the Hideaway Park magma. From the shallower reservoir, during open- or closed-system magma decompression, the melt initially becomes slightly reduced to NNO – 0·5 and then ascends with a relatively constant fO_2. In the case of the stalled, crystallizing intrusions, the decompressing aqueous fluid evolves to more reduced conditions. It should be noted that the open-system model results do not reach surface pressure ($P = 0{\cdot}1$ MPa) because the C-species are exhausted at depth.

The chemical evolution of exsolving volatiles is complex in rising magma, and the various species may change their relative proportions within the exsolved fluid by orders of magnitude (Fig. 15b; Burgisser *et al.*, 2008, in preparation). For simplicity, we show only the results for magma decompression from the deep storage area. During closed-system ascent and degassing, CH_4 is initially the dominant species in the exsolving volatile phase, followed by H_2O (with lesser CO_2, H_2S, and even smaller quantities of H_2, SO_2, CO, and S_2). At ~100 MPa, the fluid is dominated by H_2O with lesser CO_2, CH_4, and H_2S. With progressive ascent, H_2O remains the dominant species, but H_2 and SO_2 gradually become more abundant, whereas other fluid species remain constant or decrease in abundance. During open-system ascent and degassing, the exsolved fluid swiftly becomes H_2O-dominant; all fluid species except H_2 decrease significantly, and all C-species are exhausted by ~45 MPa (~1 km depth).

Whereas this model (Fig. 15) does not account for halogen-bearing systems, experimental work on F- and Cl-bearing systems demonstrates that F is highly soluble in topaz rhyolite melt, whereas Cl is partitioned into the exsolving aqueous fluid at shallow crustal pressures (e.g. Webster & Holloway, 1988; Webster, 1990; Keppler & Wyllie, 1991; Holtz *et al.*, 1993; Webster & Rebbert, 1998). The high concentrations of F and Cl in the melt inclusions (Fig. 7) over a range of Nb contents generally support compatibility in the melt, but the spread in F and Cl contents is probably the result of competing forces of partitioning halogens into mineral phases (biotite, titanite; Fig. 5) and a magmatic volatile phase. Recent experiments by Gardner *et al.* (2006) suggest that the fluid/melt partition coefficient of Cl is ~10 at 300 MPa, decreasing to ~2 at the surface. This suggests that Cl partitions into the exsolving fluid phase at all pressures considered here, but does so most strongly at depth. This is in good agreement with the experiments of Webster (1997), which show that at ~200 MPa the first magmatic volatile phase to exsolve from topaz rhyolite melts containing ~1 wt % F should be highly enriched in alkali chlorides. At shallower pressures of ≤100 MPa, Cl resides in the exsolved fluid as HCl (Shinohara, 2009), which lowers the effective fugacities of the other volatile species in a proportional fashion but does not affect the behavior of other volatile species during decompression (e.g. Fig. 15b). It is worth noting that the Hideaway Park pumice matrix glass contains ~360 ppm Cl (Fig. 7), which implies that ~10% of the original Cl remained dissolved in the melt and Cl did not fully exsolve into an immiscible magmatic fluid or vapor, even upon eruption and welding of the tuff. However, the ~9/10 of Cl that did exsolve into the fluid probably played a vital role in the complexing of metals, and hence ore formation. Indeed, fluid inclusions from Henderson show that remarkably saline fluids (≤65 wt % NaCl ± KCl), which unmixed along with vapor from a juvenile, lower salinity magmatic fluid, are responsible for mineralization of main stage quartz molybdenite veins and high-temperature alteration at Henderson (e.g. White *et al.*, 1981; Seedorff & Einaudi, 2004*b*).

The capacity for metals to partition out of the Hideaway Park magma and into an exsolving hydrosaline fluid would depend on the presence of ligands with which metals could form complexes (e.g. Hedenquist & Lowenstern, 1994). Mo and W are known to be soluble as hydroxyacid (OH) complexes, whereas Pb, Zn, Cu, Sn, and Ag are typically soluble as chloride complexes (e.g. Hedenquist & Lowenstern, 1994; Zotov *et al.*, 1995; Zajacz *et al.*, 2008), although much remains to be understood about metal–ligand formation. For example, in the Cl- and F-bearing haplogranite system, the fluid/melt K_D^{Mo} is ~7 for pure H_2O and decreases to ~0·7 with incorporation of HCl and HF in the fluid (Keppler & Wyllie, 1991). Whereas Mo does not complex with Cl in hydrosaline fluids (Candela & Holland, 1984), Na and K will partition into Cl-bearing fluids as chloride complexes (Webster & Holloway, 1988) and Mo may form Na-molybdate and/or K-molybdate complexes in such a fluid exsolved from topaz rhyolite (Webster, 1997).

Considering the chemical evolution of exsolving magmatic aqueous fluids discussed above, it would seem that fluids exsolved from the Hideaway Park magma should have had appropriate ligands to entrain at least some metals. However, there is no evidence for significant partitioning of Mo, or any other metals of interest for Henderson, into an exsolved hydrosaline fluid (or fractionating mineral phase) over the evolutionary interval preserved by the melt inclusions (Fig. 11). Otherwise, we would expect to see an abrupt drop in metal concentrations, as has been documented by Mo in melt inclusions from Cave Peak, TX (e.g. Fig. 12; Audétat, 2010), and clearer evidence for degassing of volatiles other than H_2O and CO_2 (e.g. Fig. 7). Although we cannot quantitatively document the role that volatile loss plays in fractionating metals with these melt inclusion data, volatiles (such as S, F, and especially Cl) must certainly play an important role. Intriguingly,

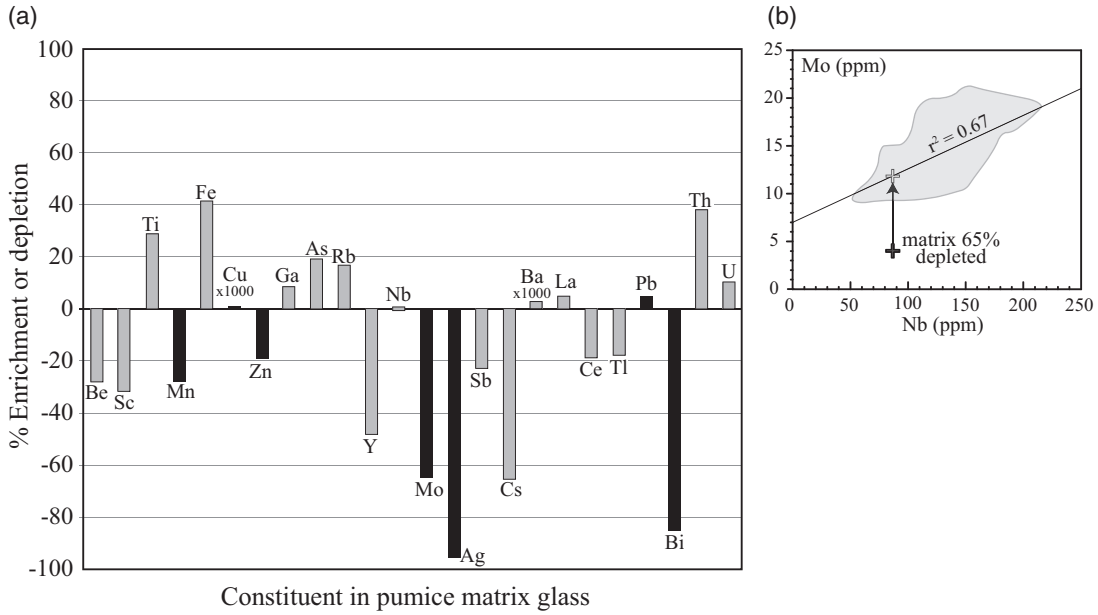

Fig. 16. (a) Per cent relative enrichment and depletion for 24 elements in the Hideaway Park pumice matrix glass, arranged by atomic number. These values are simply the difference between the pumice matrix glass elemental concentrations relative to those expected from melt inclusion metal/Nb ratios, shown schematically for Mo/Nb in (b). Black bars denote metals that are geochemically anomalous at Henderson (Seedorff & Einaudi, 2004*b*). (Melt inclusion metal/Nb ratios range in r^2 values: $r^2 = 0{\cdot}30$–$0{\cdot}67$, Mn, Ga, Rb, Y, Mo, Cs, Bi, Th, U; $r^2 = 0{\cdot}20$–$0{\cdot}29$, Be, Ce, Tl; $r^2 = 0{\cdot}10$–$0{\cdot}19$, Ti, Fe, As; $r^2 = 0{\cdot}01$–$0{\cdot}09$, Sc, Cu, Zn, Ag, Sb, Ba, La, Ce, Pb.)

there is a clear discrepancy between the concentration of F, Cl, and some metals in the pumice matrix glass compared with that in the melt inclusions. Some metal concentrations in the pumice matrix glass are exactly what we would expect for a comparatively less evolved melt; that is, they lie along the expected metal/Nb slope defined by the melt inclusions (e.g. Fig. 9). This is the case not only for Rb and U, but also for incompatible elements such as Ga, As, Sb, La, Ce, Tl, and Pb. In contrast, some metal concentrations are anomalously low, below the expected metal/Nb trend. This is most pronounced for Mo, Ag, and Bi, but also to a lesser extent for Be, Sc, Mn, Zn, Y, and Cs (Fig. 11). We interpret this discrepancy to indicate that after the last melt inclusion was trapped, at which point the melt was rich in volatiles and incompatible metals, the metals that are 'depleted' in the pumice matrix glass (Mo, Ag, Bi, Y, Ce, Be, Sc, Mn, and Zn) must have partitioned into an exsolved aqueous fluid upon ascent and eruption (Fig. 16). Such exsolution of metals may be common during decompression and eruption of magma such as the Hideaway Park rhyolite or during closed- to open-system magma degassing from a cupola beneath a porphyry deposit during periodic pressure drops (i.e. lithostatic to hydrostatic). Generation of ore-forming fluids probably involves a combination of exsolution during analogous shallow magma decompression and during isobaric crystallization when magma stalls and cools at shallow depths (Fig. 17; e.g. Burnham, 1979). The porphyry deposit at Henderson is endowed not only with economic grades of Mo, but also with anomalous concentrations of the same suite of elements (W, Pb, Zn, Cu, Bi, Ag, and Mn; Seedorff & Einaudi, 2004*b*). However, some metal concentrations are unexpectedly high in the pumice matrix glass, especially those of Cu and Ba, but to a lesser extent those of Ti, Fe, and Th (Fig. 16). The 'enrichment' of these metals in the pumice matrix glass is somewhat enigmatic. For example, Cu and Fe are thought to be highly compatible in Cl-bearing aqueous fluids (e.g. Simon *et al.*, 2004, 2008). Given the accessory phase assemblage of the Hideaway Park tuff, it seems unlikely that microlites within the pumice matrix glass could explain these enrichments. Instead, they could be the result of a combination of processes that deserve further study, such as late-stage input from mafic magma or concentration within a cupola of the shallow magma reservoir, a process that is commonly called upon in porphyry systems (Seedorff *et al.*, 2005; Sillitoe, 2010).

The apparent melt-affinity of metals recorded by quartz-hosted melt inclusions (i.e. prior to eruption, as recorded by pumice matrix glass) is somewhat puzzling, especially considering that many of these inclusions were apparently trapped at pressures sufficiently low ($\leq$200 MPa) that hydrosaline fluid saturation is indicated both by experiments and by chemical modeling. The only reasonable explanation is that the entrapment pressures must be higher for a C–O–H–S–F–Cl-bearing melt than those we calculated based on the current H_2O–CO_2 solubility models for C–O–H-bearing melts. Recent experiments by Webster *et al.* (2011) demonstrate that addition of only $\sim$200 ppm dissolved S in a granitic melt can reduce the solubility of CO_2, thus underestimating the volatile saturation pressure by as much as $\sim$50 MPa. By analogy, we hypothesize that the addition of $\sim$1 wt % dissolved F + Cl must drastically

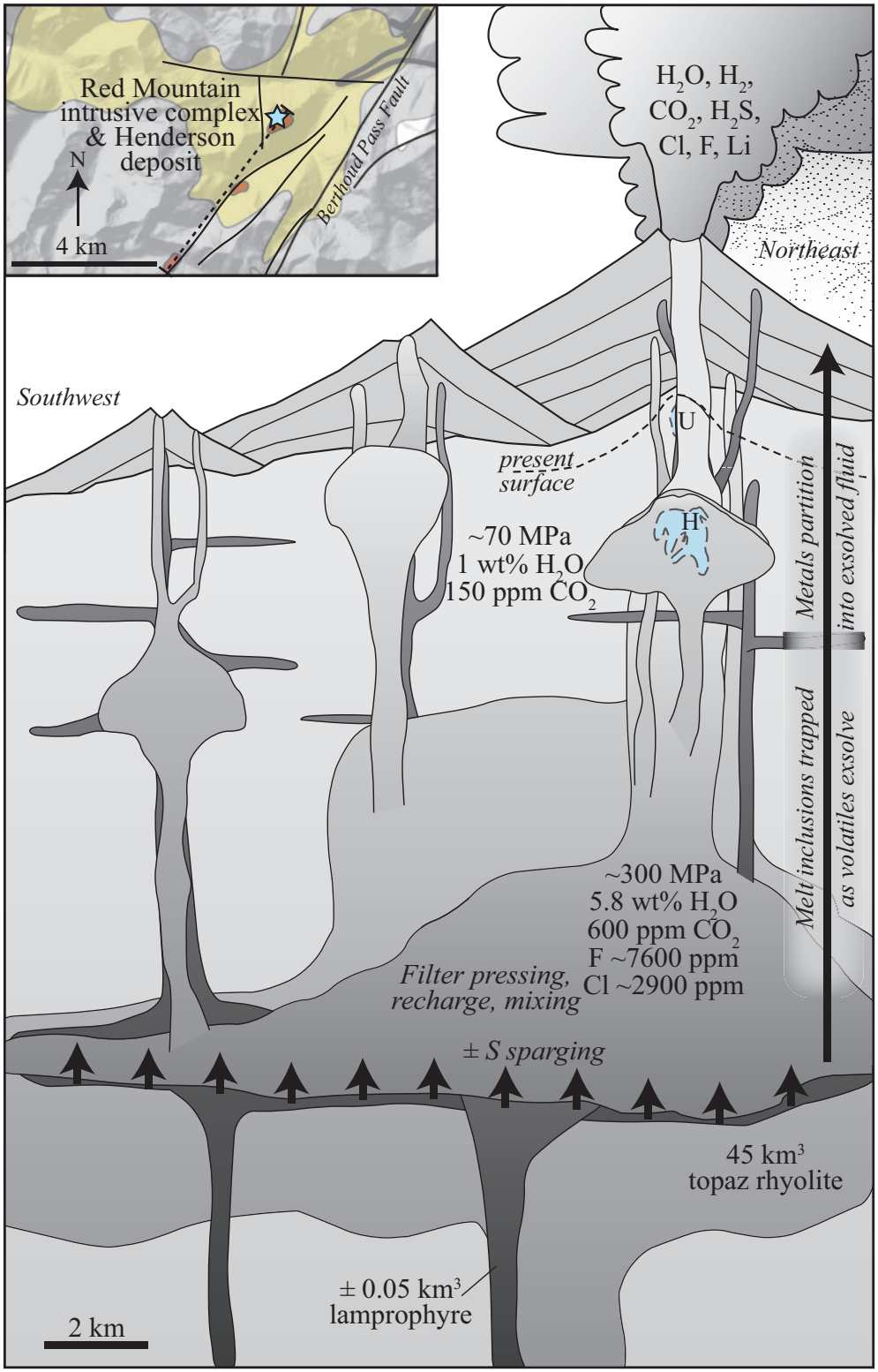

Fig. 17. Interpretative schematic cross-section of the magmatic system beneath the Urad (U) and Henderson (H) porphyry Mo deposits. The map inset shows the approximate SW–NE cross-section location with a dashed line. Positions of volcanic centers are based on locations of the Red Mountain intrusive complex (denoted with a star) and similar age rhyolite porphyry stocks to the SW (shaded orange). Magma chamber and conduit positions are hypothetical, but based on minimum pressure estimates from melt inclusions. Dark shaded conduits denote lamprophyre magma whereas light shaded conduits indicate topaz rhyolite magma; these are not to scale. Sparging of S from the lamprophyre could provides S and heat, and enhance filter pressing and magma mixing. Volatiles begin to exsolve from melt at ≥8 km depth and continue as magma ascends, but the majority of Cl and metals do not partition into the immiscible aqueous fluid until the magma reaches shallow depths of ≤2 km. Vertical scale is exaggerated by ~2 × (modified from Seedorff & Einaudi, 2004*a*; Audétat & Pettke, 2006).

reduce the effective partial pressure of dissolved CO_2 and/or H_2O, leading to erroneously low calculated melt inclusion entrapment pressures, probably underestimating the true pressure by more than 50 MPa. Thus, the Hideaway Park magma may have resided sufficiently deep that it had not yet exsolved a significant volume of fluid (or metals) at the time of quartz-hosted melt inclusion entrapment. Indeed, CO_2 is the only volatile phase in the Hideaway Park magma that we can say probably decreased with progressive melt evolution (Figs 7 and 8). Concentrations of Cl notably remain high with progressive melt evolution (Fig. 7), and Cl must have exsolved (along with some metals) into an immiscible fluid phase after cessation of quartz crystallization, shallower in the system.

Volume of source magmas

The Urad–Henderson system is the second largest Climax-type Mo deposit, with combined production and reserves of 449 Mt of ore at an average grade of 0·38% MoS_2, using a cutoff grade of 0·2% MoS_2 (Carten *et al.*, 1993; Seedorff & Einaudi, 2004*a*). To account for the $\sim 1{\cdot}0 \times 10^6$ t of Mo present in the ore deposit, a volume of $\sim 45\,km^3$ of Hideaway Park rhyolite magma would have been necessary as a Mo source. This calculation assumes 65% Mo removal efficiency (Fig. 16) from magma containing 15 ppm Mo, and a magma density of $2{\cdot}3\,g\,cm^{-3}$ [calculated following Luhr (2001)]. This estimate should be considered a minimum because a large portion of the Urad ore shell was destroyed during emplacement of the Red Mountain porphyry (Fig. 1). This magma volume corresponds to a cube with sides $\sim 3{\cdot}6$ km long or a cylinder with a diameter of $\sim 3{\cdot}1$ km that is 6 km tall. For comparison, it is equivalent to about 10 times the erupted volume of the largest plinian eruption from Somma–Vesuvius, Pomici di Base ($4{\cdot}4\,km^3$; Cioni *et al.*, 2008), or about four times the erupted volume from the plinian eruption of Krakatau in 1883 ($\sim 10\,km^3$; Self, 1992). It is likely that the majority of such magma did not erupt, but rather stalled in an open-system, shallow crustal reservoir and exsolved profuse amounts of magmatic fluids ($\sim 6\,km^3$ H_2O, assuming $45\,km^3$ of rhyolite exsolves 6 wt % H_2O), beneath the Urad–Henderson deposit.

A minimum of $\sim 6{\cdot}8 \times 10^5$ t of S is required to form the MoS_2 at the Urad–Henderson deposit, and still more is required to account for the significant amount of non-economic sulfide minerals that precipitated in the phyllic halo around the Mo shell (e.g. pyrite, pyrrhotite, sphalerite, galena, chalcopyrite; Seedorff & Einaudi, 2004*b*). Previous studies on porphyry Mo deposits have suggested that ore-forming S may be sourced either by enrichment of residual felsic liquids owing to fractional crystallization (e.g. Cave Peak, TX; Audétat, 2010) or by transport from underplating mafic magmas to felsic magmas by magma mixing and/or volatile fluxing (e.g. Pine Grove, UT, Keith *et al.*, 1986; Bingham, UT, Hattori & Keith, 2001). If the $\sim 45\,km^3$ of Hideaway Park rhyolite magma required for the Mo budget was the sole source of S for the Urad–Henderson deposit, it would have needed to contribute a minimum of ~ 7 ppm S. The Hideaway Park melt inclusions contain ≤ 156 ppm dissolved S (Fig. 7), typical of rhyolitic magmas (Wallace & Edmonds, 2011), which if released in its entirety would be enough to provide adequate S for the molybdenite at the Urad–Henderson system with only $\sim 2\,km^3$ of rhyolite. However, it is not obvious whether the magma was sufficiently S oversaturated to release the necessary volume of S. The few Hideaway Park melt inclusions with S contents measureable by EPMA (80–156 ppm S; Fig. 7) were trapped with ≥ 200 ppm CO_2. If these inclusions were trapped along an ideal degassing path, it is likely that they were trapped relatively deeply between ~ 200 and 300 MPa (Fig. 8). As the Hideaway Park magma ascended to a shallower rhyolite reservoir and Henderson cupola depths (from 110 to 60 MPa), the solubility of S would have decreased significantly. Results from thermodynamic magma decompression modeling suggest that the Hideaway Park magma could have contained as much as ~ 30–70 ppm dissolved S at these shallow crustal depths and an oversaturation of only 7 ppm would be adequate to provide the necessary S (Fig. 15c). Unfortunately, common analytical techniques do not have the sensitivity to measure the low S concentrations dissolved in shallow-trapped melt inclusions (e.g. Burgisser *et al.*, 2008), which is necessary to evaluate this problem. If the rhyolite could not provide the necessary S, then another source would have been essential for ore formation. There are intrusions of mantle-derived biotite–plagioclase lamprophyre (kersantite) with an age of $\sim 28{\cdot}6 \pm 3{\cdot}3$ Ma that are commingled with the rhyolitic intrusions at Red Mountain (Bookstrom *et al.*, 1988; Carten *et al.*, 1993), which may have supplied abundant S, regardless of whether the rhyolite contributed some sulfur. Sparging (i.e. gas flushing) of $\sim 6{\cdot}8 \times 10^5$ t of S in the form of H_2S and SO_2 (e.g. Scaillet & Pichavant, 2005) from only $\sim 0{\cdot}05$ km^3 of lamprophyre magma would supply enough S to generate the 437 Mt of MoS_2 ore at Henderson. This calculation assumes an average of 6000 ppm S in the lamprophyre magma, 80% S removal efficiency (i.e. 4800 ppm S; Vigouroux *et al.*, 2008), and a magma density of $2{\cdot}6\,g\,cm^{-3}$ [calculated following Luhr (2001)]. This lamprophyre magma volume corresponds to a cube with sides $\sim 0{\cdot}38$ km long, and is 900 times less than the volume of rhyolite required to satisfy the Mo budget. This agrees well with the observation that lamprophyre intrusions are a very minor component in the bimodal suite of rocks at Red Mountain (Bookstrom *et al.*, 1988). Although evidence for gas sparging is cryptic, given that S is highly insoluble in shallow rhyolitic melts at $fO_2 \sim$ NNO (Burgisser *et al.*, 2008; Wallace & Edmonds, 2011), most of the S exsolved from commingled lamprophyre magma would have been transported through the Hideaway Park magma system as an immiscible volatile phase. Although the question of lamprophyre involvement in

the generation of Climax-type porphyry Mo deposits remains unresolved, we favor this possibility because gas sparging would enhance filter pressing and magma mixing (e.g. Sisson & Bacon, 1999), processes that we know must be fairly efficient in this system. In addition, underplating by mafic magma and sparging of S would contribute heat into the rhyolitic reservoir, which would help explain the higher temperatures recorded by melt inclusions and phenocrysts (Fig. 14b). Periodic injections of mafic magma and S sparging could also trigger magma intrusion or eruption pulses (e.g. Pallister *et al.*, 1992), as well as episodes of volatile release from cupolas into the ore zone. Future, more detailed characterization of lamprophyres at Red Mountain would help to address the source of S and the question of whether such lamprophyres may contribute more than just S (e.g. CO_2, metals).

For comparison, Lowenstern (1994) estimated that ~30 km^3 of rhyolitic magma (with 3 ppm Mo) was sufficient to provide enough Mo to form the Pine Grove porphyry Mo deposit. Likewise, Audétat (2010) estimated that ~28–104 km^3 of alkali feldspar granitic magma (with 6 ppm Mo) would be required to provide the Mo budget, but only 1·4–5·2 km^3 of the same magma (with ~100 ppm S) is necessary to satisfy the S budget to form the Cave Peak, TX deposit.

Hideaway Park magma as a Climax-type porphyry Mo deposit parental magma source

Based on the distinct volatile- and metal-rich melt inclusion compositions (Figs 3, 7, 10 and 11), the suitable weighted mean age of 27·58 ± 0·24 Ma (Fig. 4), and the characteristically F-rich biotite phenocrysts (Fig. 5), we consider the genetic link between the Hideaway Park tuff, the Red Mountain intrusive complex, and the Henderson porphyry Mo deposit to be robust. We therefore deem it to be a good analog for the parental magma that formed the world-class Henderson porphyry Mo deposit. Over the lifetime of the Red Mountain magmatic center, the parental magma and accompanying exsolved fluids and metals were emplaced and degassed in a variety of ways: either quiescently with open-system degassing, violently leading to eruption, or, when the conditions were just right, semi-explosively with porphyry dike injections and hydrofracturing leading to water–rock reactions and stockwork vein formation (Fig. 17). Given that the Hideaway Park tuff is estimated to have been ~15 to >150 m thick only ~16 km NE of the Henderson deposit (Fig. 1; Shroba *et al.*, 2010) we infer that the Hideaway Park magma could reasonably have vented directly from the Red Mountain complex. If it did not, then it probably vented from another vent nearby with a shared crustal magmatic plumbing system (Fig. 17). Comparison of the tuff thickness with isopach maps from Mt. St. Helens (Carey *et al.*, 1990), Mt. Pinatubo (Koyaguchi & Tokuno, 1993), and Mt. Vesuvius (Cioni *et al.*, 2008) suggests that if the Hideaway Park magma did vent from the Red Mountain complex, it probably did so in a Vesuvius-like, plinian-style eruption (Fig. 17).

CONCLUSIONS

The combination of quartz-hosted melt inclusion, pumice matrix glass, and mineral geochemistry presented in this study allows us to reconstruct the pre-eruptive conditions, magmatic processes, and source and evolution of metals within the Hideaway Park magma. This provides a view into the magmatic processes that produced the world-class Henderson porphyry Mo deposit. A large volume (~45 km^3) of volatile- and metal-rich (≤6 wt % H_2O, ≤1 wt % F, ~15 ppm Mo) topaz rhyolite magma evolved by ≤60–70% fractional crystallization, at pressures of ≤300 MPa in the upper crust (≤8 km depth), with little to no quartz crystallization upon shallow ascent and eruption. Some combination of filter pressing, crystal settling, magma recharge, and mixing with less evolved rhyolite melt was essential during magma evolution. The high F contents and low estimated viscosities (~10^5–10^{10} Pa s) of these volatile-rich melts probably enhanced these processes. The Mo in the melt was deeply sourced, from either the lower crust or metasomatized mantle, whereas S may have been sparged from a relatively small volume of comagmatic, mantle-derived lamprophyre magma.

Over the magma evolutionary window preserved by the melt inclusions, none of the metals that are of interest for mineralization at the Henderson deposit (Mo, W, Pb, Zn, Mn, Cu, Bi, Ag) appear to have been sequestered into crystallizing minerals or into an exsolved aqueous fluid. This is because the magma probably resided and evolved somewhat deeper than our melt inclusion entrapment pressures would suggest, and therefore had not yet exsolved an appreciable volume of fluid. Depletion of certain metals in the pumice matrix glass relative to the melt inclusions suggests that during shallow magma ascent and eruption, the Hideaway Park magma did exsolve a volatile phase into which metals partitioned. Aqueous fluids exsolved from analogous batches of magma that did not erupt are probably responsible for the high concentrations of Mo, W, Pb, Zn, and Mn (as well as Cu, Bi, Ag) at the Henderson deposit.

ACKNOWLEDGEMENTS

We are grateful to Tom Sisson for performing cold-seal experiments, and to Bill Benzel and Monique Adams for providing WD-XRF and ICP-MS bulk analyses. Heather Lowers and Alan Koenig generously contributed microanalytical expertise. Thanks go to Paul Wallace, Jake Lowenstern, and Andreas Audétat for thoughtful discussions. Finally, we thank Jim Webster, John Dilles, Adam Simon, Wendy Bohrson, and Alan Koenig, whose constructive reviews greatly improved this paper.

SUPPLEMENTARY DATA

Supplementary data for this paper are available at *Journal of Petrology* online.

REFERENCES

Adams, D. T., Hofstra, A. H., Cosca, M. A., Todorov, T. I. & Marsh, E. E. (2009). Age of sanidine composition of melt inclusions in quartz phenocrysts from volcanic rocks associated with large Mo and Be deposits in the western United States. GSA Annual Meeting.

Anderson, A. T., Newman, S., Williams, S. N., Druitt, T. H., Skirius, C. & Stolper, E. M. (1989). H_2O, CO_2, Cl, and gas in Plinian and ash-flow Bishop rhyolite. *Geology* **17**, 221–225.

Anderson, A. T., Davis, A. M. & Lu, F. (2000). Evolution of Bishop Tuff rhyolitic magma based on melt and magnetite inclusions and zoned phenocrysts. *Journal of Petrology* **41**, 449–473.

Audétat, A. (2010). Source and evolution of molybdenum in the porphyry Mo(–Nb) deposit at Cave Peak, Texas. *Journal of Petrology* **51**, 1739–1760.

Audétat, A. & Pettke, T. (2006). Evolution of a porphyry-Cu mineralized magma system at Santa Rita, New Mexico (USA). *Journal of Petrology* **47**, 2021–2046.

Audétat, A. & Simon, A. C. (2013). Magmatic controls on porphyry Cu genesis. In: Hedenquist, J. W., Harris, M. & Camus, F. (eds) *Geology and Genesis of Major Copper Deposits and Districts of the World: a Tribute to Richard Sillitoe. Society of Economic Geologists, Special Publication* **16**, 553–572.

Audétat, A., Dolejs, D. & Lowenstern, J. B. (2011). Molybdenite saturation in silicic magmas: occurrence and petrological implications. *Journal of Petrology* **52**, 891–904.

Bachmann, O. & Bergantz, G. W. (2004). On the origin of crystal-poor rhyolites: extracted from batholithic crystal mushes. *Journal of Petrology* **45**, 1565–1582.

Bacon, C. R. & Hirschmann, M. M. (1988). Mg/Mn partitioning as a test for equilibrium between Fe–Ti oxides. *American Mineralogist* **73**, 57–61.

Bailey, J. C. (1977). Fluorine in granitic rocks and melts: a review. *Chemical Geology* **19**, 1–42.

Baker, D. R. & Vaillancourt, J. (1995). The low viscosities of $F + H_2O$-bearing granitic melts and implications for melt extraction and transport. *Earth and Planetary Science Letters* **132**, 199–211.

Barclay, J., Carroll, M. R., Houghton, B. F. & Wilson, C. (1996). Pre-eruptive volatile content and degassing history of an evolving peralkaline volcano. *Journal of Volcanology and Geothermal Research* **74**, 75–87.

Bea, F., Pereira, M. D. & Stroh, A. (1994). Mineral/leucosome trace element partitioning in a peraluminous migmatite (a laser ablation-ICP-MS study). *Chemical Geology* **117**, 291–312.

Behrens, H., Tamic, N. & Holtz, F. (2004). Determination of the molar absorption coefficient for the infrared absorption band of CO_2 in rhyolitic glasses. *American Mineralogist* **89**, 301–306.

Bookstrom, A. A. (1981). Tectonic setting and generation of Rocky Mountain porphyry molybdenum deposits. In: Dickinson, W. R. & Payne, W. D. (eds) *Relations of Tectonics to Ore Deposits in the Southern Cordillera. Arizona Geological Society Digest* **14**, 215–226.

Bookstrom, A. A., Carten, R. B., Shannon, J. R. & Smith, R. P. (1988). Origins of bimodal leucogranite–lamprophyre suites, Climax and Red Mountain porphyry molybdenum systems, Colorado: Petrologic and strontium isotopic evidence. *Colorado School of Mines Quarterly* **83**, 1–24.

Burgisser, A., Scaillet, B. & Harshvardhan (2008). Chemical patterns of erupting silicic magmas and their influence on the amount of degassing during ascent. *Journal of Geophysical Research: Solid Earth (1978–2012)* **113**, 1–14.

Burnham, C. W. (1979). Magmas and hydrothermal fluids. In: Barnes, H. L. (ed.) *Geochemistry of Hydrothermal Ore Deposits*, pp. 71–136.

Candela, P. A. & Holland, H. D. (1984). The partitioning of copper and molybdenum between silicate melts and aqueous fluids. *Geochimica et Cosmochimica Acta* **48**, 373–380.

Carey, S., Sigurdsson, H., Gardner, J. E. & Criswell, W. (1990). Variations in column height and magma discharge during the May 18, 1980 eruption of Mount St. Helens. *Journal of Volcanology and Geothermal Research* **43**, 99–112.

Carten, R. B., Geraghty, E. P., Walker, B. M. & Shannon, J. R. (1988a). Cyclic development of igneous features and their relationship to high-temperature hydrothermal features in the Henderson porphyry molybdenum deposit, Colorado. *Economic Geology* **83**, 266–296.

Carten, R. B., Rye, R. O. & Landis, G. P. (1988b). Effects of igneous and hydrothermal processes on the composition of ore-forming fluids; stable isotope and fluid inclusion evidence, Henderson porphyry molybdenum deposit, Colorado. *Geological Society of America, Abstracts with Programs* **19**, A94.

Carten, R. B., Walker, B. M., Geraghty, E. P. & Gunow, A. J. (1988c). Comparison of field-based studies of the Henderson porphyry molybdenum deposit, Colorado, with experimental and theoretical models of porphyry systems. In: Taylor, R. P. & Strong, D. F. (eds) *Recent Advances in the Geology of Granite-related Mineral Deposits. The Canadian Institute of Mining and Metallurgy Special Volume* **39**, 351–366.

Carten, R. B., White, W. H. & Stein, H. J. (1993). High-grade granite-related molybdenum systems: Classification and origin. In: Kirkham, R. V., Sinclair, W. D., Thorpe, R. I. & Duke, J. M. (eds) *Mineral Deposit Modeling. Geological Association of Canada Special Paper* **40**, 521–554.

Christensen, J. N. & Halliday, A. N. (1996). Rb–Sr ages and Nd isotopic compositions of melt inclusions from the Bishop Tuff and the generation of silicic magma. *Earth and Planetary Science Letters* **144**, 547–561.

Christiansen, E. H. & Venchiarutti, D. A. (1990). Magmatic inclusions in rhyolites of the Spor Mountain Formation, western Utah: Limitations on compositional inferences from inclusions in granitic rocks. *Journal of Geophysical Research: Solid Earth (1978–2012)* **95**, 17717–17728.

Christiansen, E. H., Burt, D. M., Sheridan, M. F. & Wilson, R. T. (1983). The petrogenesis of topaz rhyolites from the western United States. *Contributions to Mineralogy and Petrology* **83**, 16–30.

Christiansen, E. H., Bikun, J. V., Sheridan, M. F. & Burt, D. M. (1984). Geochemical evolution of topaz rhyolites from the Thomas Range and Spor Mountain, Utah. *American Mineralogist* **69**, 223–236.

Christiansen, E. H., Sheridan, M. F. & Burt, D. M. (1986). *The Geology and Geochemistry of Cenozoic Topaz Rhyolites from the Western United States. Geological Society of America, Special Papers* **205**, 82 pp.

Christiansen, E. H., Haapala, I. & Hart, G. L. (2007). Are Cenozoic topaz rhyolites the erupted equivalents of Proterozoic rapakivi granites? Examples from the western United States and Finland. *Lithos* **97**, 219–246.

Cioni, R., Bertagnini, A., Santacroce, R. & Andronico, D. (2008). Explosive activity and eruption scenarios at Somma-Vesuvius (Italy): towards a new classification scheme. *Journal of Volcanology and Geothermal Research* **178**, 331–346.

Congdon, R. D. & Nash, W. P. (1991). Eruptive pegmatite magma: rhyolite of the Honeycomb Hills, Utah. *American Mineralogist* **76**, 1261–1278.

Donovan, J. J. & Tingle, T. N. (1996). An improved mean atomic number background correction for quantitative microanalysis. *Microscopy and Microanalysis* **2**, 1–7.

Donovan, J. J., Lowers, H. A. & Rusk, B. G. (2011). Improved electron probe microanalysis of trace elements in quartz. *American Mineralogist* **96**, 274–282.

Ewart, A. & Griffin, W. L. (1994). Application of proton-microprobe data to trace element partitioning in volcanic rocks. *Chemical Geology* **117**, 251–284.

Farmer, G. L. (2003). Continental basaltic rocks. In: Rudnick, R. L. (ed.) *Treatise on Geochemistry 3*. Elsevier, pp. 85–121.

Farmer, G. L. & DePaolo, D. J. (1984). Origin of Mesozoic and Tertiary granite in the western United States and implications for Pre-Mesozoic crustal structure: 2. Nd and Sr isotopic studies of unmineralized and Cu- and Mo-mineralized granite in the Precambrian Craton. *Journal of Geophysical Research: Solid Earth (1978–2012)* **89**, 10141–10160.

Fournier, R. O. (1999). Hydrothermal processes related to movement of fluid from plastic into brittle rock in the magmatic–epithermal environment. *Economic Geology* **94**, 1193–1211.

Gardner, J. E., Burgisser, A., Hort, M. & Rutherford, M. (2006). Experimental and model constraints on degassing of magma during ascent and eruption. In: Siebe, C., Macías, J. L. & Aguirre-Díaz, G. J. (eds) *Neogene–Quaternary Continental Margin Volcanism: A Perspective from México. Geological Society of America, Special Papers* **402**, 99–113.

Geissman, J. W., Snee, L. W., Graaskamp, G. W., Carten, R. B. & Geraghty, E. P. (1992). Deformation and age of the Red Mountain intrusive system (Urad–Henderson molybdenum deposits), Colorado: Evidence from paleomagnetic and $^{40}Ar/^{39}Ar$ data. *Geological Society of America Bulletin* **104**, 1031–1047.

Geraghty, E. P., Carten, R. B. & Walker, B. M. (1988). Tilting of Urad–Henderson and Climax porphyry molybdenum systems, central Colorado, as related to northern Rio Grande rift tectonics. *Geological Society of America Bulletin* **100**, 1780–1786.

Ghiorso, M. S. & Evans, B. W. (2008). Thermodynamics of rhombohedral oxide solid solutions and a revision of the Fe–Ti two-oxide geothermometer and oxygen-barometer. *American Journal of Science* **308**, 957–1039.

Giordano, D., Romano, C., Dingwell, D. B., Poe, B. & Behrens, H. (2004). The combined effects of water and fluorine on the viscosity of silicic magmas. *Geochimica et Cosmochimica Acta* **68**, 5159–5168.

Gunow, A. J., Ludington, S. & Munoz, J. L. (1980). Fluorine in micas from the Henderson molybdenite deposit, Colorado. *Economic Geology* **75**, 1127–1137.

Hattori, K. X. I. & Keith, J. (2001). Contribution of mafic melt to porphyry copper mineralization: evidence from Mount Pinatubo, Philippines, and Bingham Canyon, Utah, USA. *Mineralium Deposita* **36**, 799–806.

Hayden, L. A. & Watson, E. B. (2007). Rutile saturation in hydrous siliceous melts and its bearing on Ti-thermometry of quartz and zircon. *Earth and Planetary Science Letters* **258**, 561–568.

Hedenquist, J. W. & Lowenstern, J. B. (1994). The role of magmas in the formation of hydrothermal ore deposits. *Nature* **370**, 519–527.

Henry, D. J., Guidotti, C. V. & Thomson, J. A. (2005). The Ti-saturation surface for low-to-medium pressure metapelitic biotites: Implications for geothermometry and Ti-substitution mechanisms. *American Mineralogist* **90**, 316–328.

Hervig, R. L., Dunbar, N., Westrich, H. R. & Kyle, P. R. (1989). Pre-eruptive water content of rhyolitic magmas as determined by ion microprobe analyses of melt inclusions in phenocrysts. *Journal of Volcanology and Geothermal Research* **36**, 293–302.

Hildreth, W. (1977). The magma chamber of the Bishop Tuff: Gradients in temperature, pressure, and composition. PhD thesis, University of California, Berkeley, 328 pp.

Hofstra, A. H., Todorov, T. I. & Mercer, C. N. (2013). Silicate melt inclusion evidence for extreme pre-eruptive enrichment and post-eruptive depletion of lithium in silicic volcanic rocks of the western United States: Implications for the origin of lithium-rich brines. *Economic Geology* **108**, 1691–1701.

Holtz, F., Dingwell, D. B. & Behrens, H. (1993). Effects of F, B_2O_3 and P_2O_5 on the solubility of water in haplogranite melts compared to natural silicate melts. *Contributions to Mineralogy and Petrology* **113**, 492–501.

Huang, R. & Audétat, A. (2012). The titanium-in-quartz (TitaniQ) thermobarometer: A critical examination and re-calibration. *Geochimica et Cosmochimica Acta*, **84**, 75–89.

Jacobs, D. C. & Parry, W. T. (1979). Geochemistry of biotite in the Santa Rita porphyry copper deposit, New Mexico. *Economic Geology* **74**, 860–887.

Jochum, K. P., Weis, U., Stoll, B., Kuzmin, D., Yang, Q., Raczek, I., Jacob, D. E., Stracke, A., Birbaum, K., Frick, D. A., Günther, D. & Enzweiler, J. (2011). Determination of reference values for NIST SRM 610–617 glasses following ISO guidelines. *Geostandards and Geoanalytical Research* **35**, 397–429.

Johnson, C. M. & Lipman, P. W. (1988). Origin of metaluminous and alkaline volcanic rocks of the Latir volcanic field, northern Rio Grande rift, New Mexico. *Contributions to Mineralogy and Petrology* **100**, 107–128.

Johnson, C. M., Czamanske, G. K. & Lipman, P. W. (1989). Geochemistry of intrusive rocks associated with the Latir volcanic field, New Mexico, and contrasts between evolution of plutonic and volcanic rocks. *Contributions to Mineralogy and Petrology* **103**, 90–109.

Johnson, E. R., Kamenetsky, V. S., McPhie, J. & Wallace, P. J. (2011). Degassing of the H_2O-rich rhyolites of the Okataina Volcanic Center, Taupo Volcanic Zone, New Zealand. *Geology* **39**, 311–314.

Johnson, E. R., Kamenetsky, V. S. & McPhie, J. (2013). The behavior of metals (Pb, Zn, As, Mo, Cu) during crystallization and degassing of rhyolites from the Okataina Volcanic Center, Taupo Volcanic Zone, New Zealand. *Journal of Petrology* **54**, 1641–1659.

Kamenetsky, V. S. & Danyushevsky, L. V. (2005). Metals in quartz-hosted melt inclusions: Natural facts and experimental artifacts. *American Mineralogist* **90**, 1674–1678.

Keith, J. D. & Christiansen, E. H. (1993). The genesis of giant porphyry molybdenum deposits. In: Hodgson, C. J., Mason, R. & Whiting, B. H. (eds) *Giant Ore Deposits. Society of Economic Geologists Special Publication* **2**, 285–316.

Keith, J. D., Shanks, W. C., Archibald, D. A. & Farrar, E. (1986). Volcanic and intrusive history of the Pine Grove porphyry molybdenum system, southwestern Utah. *Economic Geology* **81**, 553–577.

Kellogg, K. S., Shroba, R. R., Bryant, B. & Premo, W. R. (2008). *Geologic Map of the Denver West 30′ × 60′ Quadrangle, North–central Colorado*. US Geological Survey.

Keppler, H. & Wyllie, P. J. (1991). Partitioning of Cu, Sn, Mo, W, U, and Th between melt and aqueous fluid in the systems haplogranite–H_2O–HCl and haplogranite–H_2O–HF. *Contributions to Mineralogy and Petrology* **109**, 139–150.

Klemm, L. M., Pettke, T. & Heinrich, C. A. (2008). Fluid and source magma evolution of the Questa porphyry Mo deposit, New Mexico, USA. *Mineralium Deposita* **43**, 533–552.

Knox, K. L. (2005). Never Summer igneous complex—Evolution of a shallow magmatic system. MS thesis, University of Colorado, 54 pp.

Koyaguchi, T. & Tokuno, M. (1993). Origin of the giant eruption cloud of Pinatubo, June 15, 1991. *Journal of Volcanology and Geothermal Research* **55**, 85–96.

Kuiper, K. F., Deino, A., Hilgen, F. J., Krijgsman, W., Renne, P. R. & Wijbrans, J. R. (2008). Synchronizing rock clocks of Earth history. *Science* **320**, 500–504.

Lehmann, B. (1987). Molybdenum distribution in Precambrian rocks of the Colorado Mineral Belt. *Mineralium Deposita* **22**, 47–52.

Lerchbaumer, L. & Audétat, A. (2013). The metal content of silicate melts and aqueous fluids in subeconomically Mo mineralized granites: implications for porphyry Mo genesis. *Economic Geology* **108**, 987–1013.

Liu, Y., Zhang, Y. & Behrens, H. (2005). Solubility of H_2O in rhyolitic melts at low pressures and a new empirical model for mixed H_2O–CO_2 solubility in rhyolitic melts. *Journal of Volcanology and Geothermal Research* **143**, 219–235.

Liu, Y., Anderson, A. T., Wilson, C. J., Davis, A. M. & Steele, I. M. (2006). Mixing and differentiation in the Oruanui rhyolitic magma, Taupo, New Zealand: evidence from volatiles and trace elements in melt inclusions. *Contributions to Mineralogy and Petrology* **151**, 71–87.

Liu, Y., Anderson, A. T. & Wilson, C. J. (2007). Melt pockets in phenocrysts and decompression rates of silicic magmas before fragmentation. *Journal of Geophysical Research: Solid Earth (1978–2012)* **112**, 1–12.

Lowenstern, J. B. (1994). Dissolved volatile concentrations in an ore-forming magma. *Geology* **22**, 893–896.

Lowenstern, J. B., Bacon, C. R., Calk, L. C., Hervig, R. L. & Aines, R. D. (1994). Major-element, trace element, and volatile concentrations in silicate melt inclusions from the tuff of Pine Grove, Wah Wah Mountains, Utah. US Geological Survey, Open-File Report 94-242, 20 pp.

Lu, F., Anderson, A. T. & Davis, A. M. (1992). Melt inclusions and crystal-liquid separation in rhyolitic magma of the Bishop Tuff. *Contributions to Mineralogy and Petrology* **110**, 113–120.

Lüders, V., Romer, R. L., Gilg, H. A., Bodnar, R. J., Pettke, T. & Misantoni, D. (2009). A geochemical study of the Sweet Home Mine, Colorado Mineral Belt, USA: hydrothermal fluid evolution above a hypothesized granite cupola. *Mineralium Deposita* **44**, 415–434.

Ludington, S. & Plumlee, G. S. (2009). Climax-type porphyry molybdenum deposits. US Geological Survey, Open-File Report 1215, 16 pp.

Luhr, J. F. (2001). Glass inclusions and melt volatile contents at Paricutin Volcano, Mexico. *Contributions to Mineralogy and Petrology* **142**, 261–283.

Mahood, G. & Hildreth, W. (1983). Large partition coefficients for trace elements in high-silica rhyolites. *Geochimica et Cosmochimica Acta* **47**, 11–30.

Mandeville, C. W., Webster, J. D., Rutherford, M. J., Taylor, B. E., Timbal, A. & Faure, K. (2002). Determination of molar absorptivities for infrared absorption bands of H_2O in andesitic glasses. *American Mineralogist* **87**, 813–821.

Markey, R., Stein, H. J., Hannah, J. L., Zimmerman, A., Selby, D. & Creaser, R. A. (2007). Standardizing Re–Os geochronology: A new molybdenite Reference Material (Henderson, USA) and the stoichiometry of Os salts. *Chemical Geology* **244**, 74–87.

Mason, R. A. (1992). Models of order and iron–fluorine avoidance in biotite. *Canadian Mineralogist* **30**, 343–354.

McDonough, W. F. & Sun, S. S. (1995). The composition of the Earth. *Chemical Geology* **120**, 223–253.

Mercer, C. N. & Reed, M. H. (2013). Porphyry Cu–Mo stockwork formation by dynamic, transient hydrothermal pulses: mineralogic insights from the deposit at Butte, Montana. *Economic Geology* **108**, 1347–1377.

Newman, S. & Lowenstern, J. B. (2002). VolatileCalc: a silicate melt–H_2O–CO_2 solution model written in Visual Basic for Excel. *Computers and Geosciences* **28**, 597–604.

Nielsen, C. H. & Sigurdsson, H. (1981). Quantitative methods for electron microprobe analysis of sodium in natural and synthetic glasses. *American Mineralogist* **66**, 547–552.

Ohmoto, H. & Goldhaber, M. B. (1997). Sulfur and carbon isotopes. In: Barnes, H. L. (ed.) *Geochemistry of hydrothermal ore deposits*, 3rd edn. Wiley, pp. 517–612.

Pallister, J. S., Hoblitt, R. P. & Reyes, A. G. (1992). A basalt trigger for the 1991 eruptions of Pinatubo Volcano? *Nature* **356**, 426–428.

Pearce, J. A., Harris, N. B. W. & Tindle, A. G. (1984). Trace element discrimination diagrams for the tectonic interpretation of granitic rocks. *Journal of Petrology* **25**, 956–983.

Peterman, Z. E., Hedge, C. E. & Braddock, W. A. (1968). Age of Precambrian events in the northeastern Front Range, Colorado. *Journal of Geophysical Research: Solid Earth (1978–2012)* **73**, 2277–2296.

Pettke, T., Oberli, F. & Heinrich, C. A. (2010). The magma and metal source of giant porphyry-type ore deposits, based on lead isotope microanalysis of individual fluid inclusions. *Earth and Planetary Science Letters* **296**, 267–277.

Putirka, K. D. (2008). Thermometers and barometers for volcanic systems. In: Putirka, K. D. & Tepley, F. J., III (eds) *Minerals, Inclusions and Volcanic Processes. Mineralogical Society of America and Geochemical Society, Reviews in Mineralogy and Geochemistry* **69**, 61–120.

Robb, L. (2005). Igneous ore-forming processes. In: Robb, L. (ed.) *Introduction to Ore-forming Processes* **1**, 19–74.

Roberge, J., Wallace, P. J. & Kent, A. J. R. (2013). Magmatic processes in the Bishop Tuff rhyolitic magma based on trace elements in melt inclusions and pumice matrix glass. *Contributions to Mineralogy and Petrology* **165**, 237–257.

Rudnick, R. L. & Gao, S. (2003). Composition of the continental crust. In: Rudnick, R. L. (ed.) *Treatise on Geochemistry 3*. Amsterdam: Elsevier, pp. 1–64.

Scaillet, B. & Pichavant, M. (2005). A model of sulphur solubility for hydrous mafic melts: Application to the determination of magmatic fluid compositions of Italian volcanoes. *Annals of Geophysics* **48**, 671–698.

Schmitt, A. K. & Simon, J. I. (2004). Boron isotopic variations in hydrous rhyolitic melts: a case study from Long Valley, California. *Contributions to Mineralogy and Petrology* **146**, 590–605.

Seedorff, E. & Einaudi, M. T. (2004a). Henderson porphyry molybdenum system, Colorado: I. Sequence and abundance of hydrothermal mineral assemblages, flow paths of evolving fluids, and evolutionary style. *Economic Geology* **99**, 3–37.

Seedorff, E. & Einaudi, M. T. (2004b). Henderson porphyry molybdenum system, Colorado: II. Decoupling of introduction and deposition of metals during geochemical evolution of hydrothermal fluids. *Economic Geology* **99**, 39–72.

Seedorff, E., Dilles, J. H., Proffett, J. M., Einaudi, M. T., Zurcher, L., Stavast, W. J., Johnson, D. A. & Barton, M. D. (2005). Porphyry deposits: characteristics and origin of hypogene features. *Economic Geology 100th Anniversary Volume* **29**, 251–298.

Self, S. (1992). Krakatau revisited: the course of events and interpretation of the 1883 eruption. *GeoJournal* **28**, 109–121.

Severs, M. J., Azbej, T., Thomas, J. B., Mandeville, C. W. & Bodnar, R. J. (2007). Experimental determination of H_2O loss from melt inclusions during laboratory heating: Evidence from Raman spectroscopy. *Chemical Geology* **237**, 358–371.

Shane, P., Martin, S. B., Smith, V. C., Beggs, K. F., Darragh, M. B., Cole, J. W. & Nairn, I. A. (2007). Multiple rhyolite magmas and basalt injection in the 17·7 ka Rerewhakaaitu eruption episode from Tarawera volcanic complex, New Zealand.

Journal of Volcanology and Geothermal Research **164**, 1–26.

Shane, P., Smith, V. C. & Nairn, I. (2008). Millennial timescale resolution of rhyolite magma recharge at Tarawera volcano: insights from quartz chemistry and melt inclusions. *Contributions to Mineralogy and Petrology* **156**, 397–411.

Shannon, J. R., Walker, B. M., Carten, R. B. & Geraghty, E. P. (1982). Unidirectional solidification textures and their significance in determining relative ages of intrusions at the Henderson Mine, Colorado. *Geology* **10**, 293–297.

Shannon, J. R., Nelson, E. P. & Golden, R. J. (2004). Surface and underground geology of the world-class Henderson molybdenum porphyry mine, Colorado. In: Nelson, E. P. & Erslev, E. A. (eds) *Field Trips in the Southern Rocky Mountains, USA. Geological Society of America, Field Guides* **5**, 207–218.

Shinohara, H. (2009). A missing link between volcanic degassing and experimental studies on chloride partitioning. *Chemical Geology* **263**, 51–59.

Shroba, R. R., Bryant, B., Kellogg, K. S., Theobald, P. K. & Brandt, T. R. (2010). Geologic Map of the Fraser 7·5-minute Quadrangle, Grand County, Colorado. US Geological Survey.

Sillitoe, R. H. (2010). Porphyry copper systems. *Economic Geology* **105**, 3–41.

Simon, A. C., Pettke, T., Candela, P. A., Piccoli, P. M. & Heinrich, C. A. (2004). Magnetite solubility and iron transport in magmatic–hydrothermal environments. *Geochimica et Cosmochimica Acta* **68**, 4905–4914.

Simon, A. C., Candela, P. A., Piccoli, P. M., Mengason, M. J. & Englander, L. (2008). The effect of crystal–melt partitioning on the budgets of Cu, Au, and Ag. *American Mineralogist* **93**, 1437–1448.

Sinclair, W. D. (2007). Porphyry deposits. In: Goodfellow, W. D. (ed.) *Mineral Deposits of Canada: A Synthesis of Major Deposit-types, District Metallogeny, the Evolution of Geological Provinces, and Exploration Methods. Geological Association of Canada, Mineral Deposits Division, Special Publication* **5**, 223–243.

Sisson, T. W. & Bacon, C. R. (1999). Gas-driven filter pressing in magmas. *Geology* **27**, 613–616.

Sisson, T. W. & Grove, T. L. (1993). Experimental investigations of the role of H_2O in calc-alkaline differentiation and subduction zone magmatism. *Contributions to Mineralogy and Petrology* **113**, 143–166.

Skirius, C. M., Peterson, J. W. & Anderson, A. T. J. (1990). Homogenizing rhyolitic glass inclusions from the Bishop Tuff. *American Mineralogist* **75**, 1381–1398.

Smith, V., Shane, P. & Nairn, I. (2010). Insights into silicic melt generation using plagioclase, quartz and melt inclusions from the caldera-forming Rotoiti eruption, Taupo volcanic zone, New Zealand. *Contributions to Mineralogy and Petrology* **160**, 951–971.

Stavast, W. J., Keith, J. D., Christiansen, E. H., Dorais, M. J., Tingey, D., Larocque, A. C. L. & Evans, N. (2006). The fate of magmatic sulfides during intrusion or eruption, Bingham and Tintic districts, Utah. *Economic Geology* **101**, 329–345.

Steele-MacInnis, M., Esposito, R. & Bodnar, R. J. (2011). Thermodynamic model for the effect of post-entrapment crystallization on the H_2O–CO_2 systematics of vapor-saturated, silicate melt inclusions. *Journal of Petrology* **52**, 2461–2482.

Stein, H. J. & Crock, J. G. (1990). Late Cretaceous–Tertiary magmatism in the Colorado Mineral Belt; Rare earth element and samarium–neodymium isotopic studies. In: Anderson, J. L. (ed.) *The Nature and Origin of Cordilleran Magmatism. Geological Society of America, Memoirs* **174**, 195–224.

Stein, H. J. & Hannah, J. L. (1985). Movement and origin of ore fluids in Climax-type systems. *Geology* **13**, 469–474.

Stix, J. & Gorton, M. P. (1990). Variations in trace element partition coefficients in sanidine in the Cerro Toledo Rhyolite, Jemez Mountains, New Mexico: Effects of composition, temperature, and volatiles. *Geochimica et Cosmochimica Acta* **54**, 2697–2708.

Streck, M. J. & Grunder, A. L. (1997). Compositional gradients and gaps in high-silica rhyolite. *Journal of Petrology* **38**, 133–163.

Sun, S. S. & McDonough, W. F. (1989). Chemical and isotopic systematics of oceanic basalts: implications for mantle composition and processes. In: Saunders, A. D. & Norry, M. J. (eds) *Magmatism in the Ocean Basins. Geological Society, London, Special Publications* **42**, 313–345.

Takeuchi, S. (2011). Preeruptive magma viscosity: An important measure of magma eruptibility. *Journal of Geophysical Research* **116**, 1–19.

Taylor, R. B. & King, R. U. (1967). *Preliminary report on mid-Tertiary rhyolite vents and associated mineralization south of Georgetown, Colorado. US Geological Survey, Open-File Report* **209**, 15 pp.

Taylor, R. B., Theobald, P. K. & Izett, G. A. (1968). Mid-Tertiary volcanism in the central Front Range, Colorado. *Colorado School Mines Quarterly* **63**, 39–49.

Tweto, O. & Sims, P. K. (1963). Precambrian ancestry of the Colorado mineral belt. *Geological Society of America Bulletin* **74**, 991–1014.

Vigouroux, N., Wallace, P. J. & Kent, A. J. (2008). Volatiles in high-K magmas from the Western Trans-Mexican Volcanic Belt: evidence for fluid fluxing and extreme enrichment of the mantle wedge by subduction processes. *Journal of Petrology* **49**, 1589–1618.

Wallace, P. J. & Anderson, A. T. J. (1999). Volatiles in magmas. In: Sigurdsson, H. (ed.) *Encyclopedia of Volcanoes 1*. San Diego, CA: Academic Press, pp. 149–170.

Wallace, P. J. & Edmonds, M. (2011). The sulfur budget in magmas: evidence from melt inclusions, submarine glasses, and volcanic gas emissions. In: Behrens, H. & Webster, J. D. (eds) *Sulfur in Magmas and Melts: its Importance for Natural and Technical Processes. Mineralogical Society of America and Geochemical Society, Reviews in Mineralogy and Geochemistry* **73**, 215–246.

Wallace, P. J., Anderson, A. T., Jr. & Davis, A. M. (1999). Gradients in H_2O, CO_2, and exsolved gas in a large-volume silicic magma system: interpreting the record preserved in melt inclusions from the Bishop Tuff. *Journal of Geophysical Research* **104**, 20097–20122.

Wallace, P. J., Dufek, J., Anderson, A. T. & Zhang, Y. (2003). Cooling rates of Plinian-fall and pyroclastic-flow deposits in the Bishop Tuff: inferences from water speciation in quartz-hosted glass inclusions. *Bulletin of Volcanology* **65**, 105–123.

Wallace, S. R. (1974). The Henderson ore body—elements of discovery, reflections. *American Institute of Mining, Metallurgical, and Petroleum Engineers Transactions* **256**, 216–227.

Wallace, S. R. (1995). Presidential address: The Climax-type molybdenite deposits: What they are, where they are, and why they are. *Economic Geology* **90**, 1359–1380.

Wallace, S. R., Mackenzie, W. B., Blair, R. G. & Muncaster, N. K. (1978). Geology of the Urad and Henderson molybdenite deposits, Clear Creek County, Colorado, with a section on a comparison of these deposits with those at Climax, Colorado. *Economic Geology* **73**, 325–368.

Watson, E. B. & Harrison, T. M. (1983). Zircon saturation revisited: temperature and composition effects in a variety of crustal magma types. *Earth and Planetary Science Letters* **64**, 295–304.

Webster, J. D. (1990). Partitioning of F between H_2O and CO_2 fluids and topaz rhyolite melt. *Contributions to Mineralogy and Petrology* **104**, 424–438.

Webster, J. D. (1997). Exsolution of magmatic volatile phases from Cl-enriched mineralizing granitic magmas and implications for ore metal transport. *Geochimica et Cosmochimica Acta* **61**, 1017–1029.

Webster, J. D. & Duffield, W. A. (1991). Volatiles and lithophile elements in Taylor Creek Rhyolite; constraints from glass inclusion analysis. *American Mineralogist* **76**, 1628–1645.

Webster, J. D. & Duffield, W. A. (1994). Extreme halogen abundances in tin-rich magma of the Taylor Creek Rhyolite, New Mexico. *Economic Geology* **89**, 840–850.

Webster, J. D. & Holloway, J. R. (1988). Experimental constraints on the partitioning of Cl between topaz rhyolite melt and H_2O and $H_2O + CO_2$ fluids: New implications for granitic differentiation and ore deposition. *Geochimica et Cosmochimica Acta* **52**, 2091–2105.

Webster, J. D. & Rebbert, C. R. (1998). Experimental investigation of H_2O and Cl^- solubilities in F-enriched silicate liquids; implications for volatile saturation of topaz rhyolite magmas. *Contributions to Mineralogy and Petrology* **132**, 198–207.

Webster, J. D., Holloway, J. R. & Hervig, R. L. (1987). Phase equilibria of a Be, U and F-enriched vitrophyre from Spor Mountain, Utah. *Geochimica et Cosmochimica Acta* **51**, 389–402.

Webster, J. D., Goldoff, B. & Shimizu, N. (2011). C–O–H–S fluids and granitic magma: how S partitions and modifies CO_2 concentrations of fluid-saturated felsic melt at 200 MPa. *Contributions to Mineralogy and Petrology* **162**, 849–865.

Weidner, J. R. & Martin, R. F. (1987). Phase equilibria of a fluorine-rich leucogranite from the St. Austell pluton, Cornwall. *Geochimica et Cosmochimica Acta* **51**, 1591–1597.

Westra, G. & Keith, S. B. (1981). Classification and genesis of stockwork molybdenum deposits. *Economic Geology* **76**, 844–873.

White, W. H., Bookstrom, A. A., Kamilli, R. J., Ganster, M. W., Smith, R., Ranta, D. E. & Steininger, R. C. (1981). Character and origin of Climax-type molybdenum deposits. *Economic Geology* **75**, 270–316.

Wones, D. R. (1989). Significance of the assemblage titanite + magnetite + quartz in granitic rocks. *American Mineralogist* **74**, 744–749.

Wyllie, P. J. (1979). Magmas and volatile components. *American Mineralogist* **64**, 469–500.

Wysoczanski, R. & Tani, K. (2006). Spectroscopic FTIR imaging of water species in silicic volcanic glasses and melt inclusions: An example from the Izu–Bonin arc. *Journal of Volcanology and Geothermal Research* **156**, 302–314.

Zajacz, Z., Halter, W. E., Pettke, T. & Guillong, M. (2008). Determination of fluid/melt partition coefficients by LA-ICPMS analysis of coexisting fluid and silicate melt inclusions: Controls on element partitioning. *Geochimica et Cosmochimica Acta* **72**, 2169–2197.

Zajacz, Z., Hanley, J. J., Heinrich, C. A., Halter, W. E. & Guillong, M. (2009). Diffusive reequilibration of quartz-hosted silicate melt and fluid inclusions: Are all metal concentrations unmodified? *Geochimica et Cosmochimica Acta* **73**, 3013–3027.

Zhang, L. (2000). Stable isotope investigation of a hydrothermal alteration system: Butte porphyry copper deposit. PhD thesis, Oregon State University, Corvallis, 182 pp.

Zhu, L., Ding, Z., Yao, S., Zhang, G., Song, S., Qu, W., Guo, B. & Lee, B. (2009). Ore-forming event and geodynamic setting of molybdenum deposit at Wenquan in Gansu Province, Western Qinling. *Chinese Science Bulletin* **54**, 2309–2324.

Zielinski, R. A. & Lipman, P. W. (1976). Trace element variations at Summer Coon volcano, San Juan Mountains, Colorado, and the origin of continental-interior andesite. *Geological Society of America Bulletin* **87**, 1477–1485.

Zotov, A. V., Kudrin, A. V., Levin, K. A., Shikina, N. D. & Var'yash, L. N. (1995). Experimental studies of the solubility and complexing of selected ore elements (Au, Ag, Cu, Mo, As, Sb, Hg) in aqueous solutions. In: Shmulovich, K. I., Yardley, B. W. D. & Gonchar, G. G. (eds) *Fluids in the Crust: Equilibrium and Transport Properties*. Chapman & Hall, pp. 95–137.